UCC Library and UCC researchers have made this item openly available. Please let us know how this has helped you. Thanks!

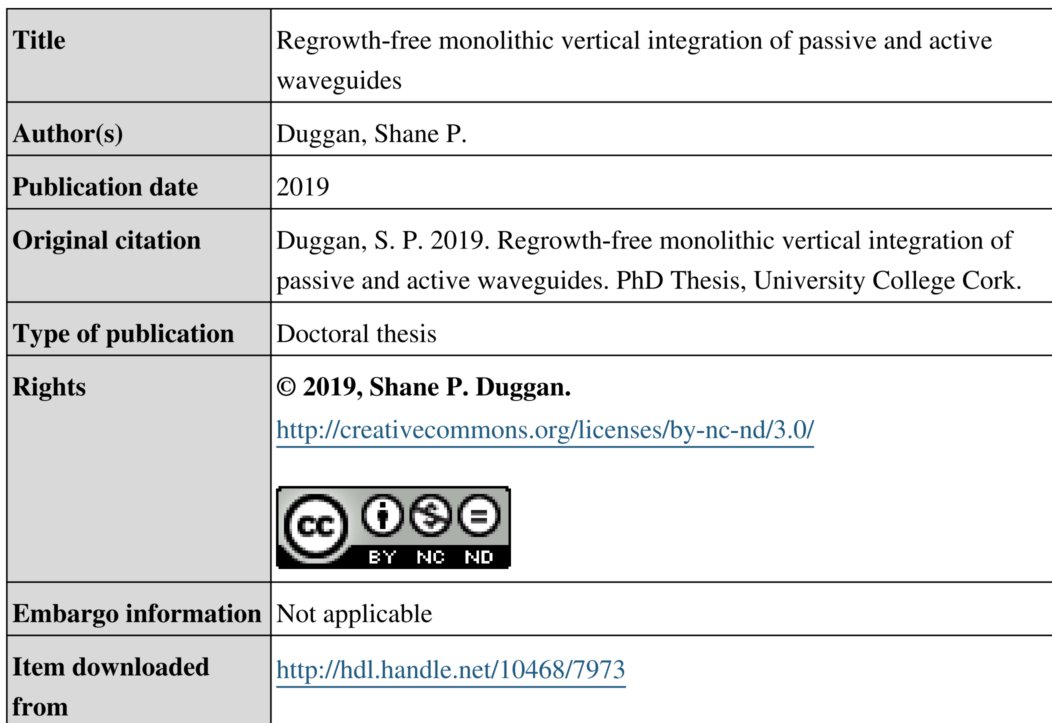

Title	Regrowth-free monolithic vertical integration of passive and active waveguides
Author(s)	Duggan, Shane P.
Publication date	2019
Original citation	Duggan, S. P. 2019. Regrowth-free monolithic vertical integration of passive and active waveguides. PhD Thesis, University College Cork.
Type of publication	Doctoral thesis
Rights	**© 2019, Shane P. Duggan.** http://creativecommons.org/licenses/by-nc-nd/3.0/
Embargo information	Not applicable
Item downloaded from	http://hdl.handle.net/10468/7973

Downloaded on 2019-12-02T14:21:53Z

University College Cork, Ireland
Coláiste na hOllscoile Corcaigh

Integrated Photonics

Regrowth-free Monolithic Vertical Integration of Passive and Active Waveguides

Shane Duggan
BSc
110328489

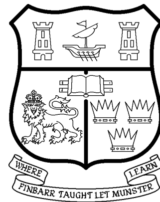

NATIONAL UNIVERSITY OF IRELAND, CORK

School of Science
Department of Physics

Thesis submitted for the degree of Doctor of Philosophy

2 May 2019

Head of Department: Prof. John McInerney

Supervisor: Prof. Frank H. Peters

Research supported by Irish Photonic Integration Centre (IPIC), Science Foundation Ireland (SFI)

Contents

List of Figures . . . iii
List of Tables . . . v
Acknowledgements . . . viii
Abstract . . . ix
List of Acronyms . . . x
List of Symbols . . . xii
List of Publications . . . xiv

1 Introduction **1**
1.1 Communications Growth . . . 1
1.2 Photonic Integration . . . 5
1.2.1 Monolithic Photonic Integration . . . 7
1.2.2 Vertical Monolithic Photonic Integration . . . 9
1.3 Thesis Motivation . . . 11
1.4 Thesis Outline . . . 13

2 Up-Down Waveguide Coupling Theory and Simulations **15**
2.1 Waveguide Tapers . . . 15
2.1.1 Waveguides . . . 15
2.1.2 Tapers . . . 20
2.1.3 Constant Overlap Tapers . . . 22
2.1.4 Comparison of Taper Shapes . . . 24
2.1.5 Beam Propagation Method . . . 26
2.1.6 Optimum Taper Shape . . . 27
2.2 Tapers for Vertical Transitions . . . 29
2.2.1 Monolithic Vertical Integration Design . . . 29
2.2.2 Coupled Waveguide Analysis . . . 31
2.2.3 Modal Overlap Analysis . . . 36
2.2.4 Beam Propagation Method Analysis . . . 40
2.2.5 Taper Optimization Simulations . . . 43
2.3 3 Waveguide Up-Down Coupling . . . 47
2.3.1 Adiabatic Transfer . . . 48
2.3.2 3 Waveguide Optimization Simulations . . . 51
2.4 Epitaxial Material Modelling . . . 55
2.5 Discussion and Conclusion . . . 58

3 Inverted N-I-P laser **60**
3.1 Epitaxial Growth . . . 62
3.2 Fabrication Design . . . 65
3.2.1 Fabrication Process . . . 65
3.2.2 Test Structures . . . 68
3.3 Testing and Characterisation . . . 71
3.3.1 LIV Measurements . . . 71
3.3.2 Pulse Testing . . . 76
3.3.3 CV Measurements . . . 79

3.3.4 ECVP and SIMS 82
3.4 Discussion and Conclusions 85

4 Up-Down Waveguide Device Design and Testing 87
4.1 Epitaxial Growth 87
4.2 Process Design 91
4.2.1 Fabrication Tolerance Simulations 91
4.2.2 Fabrication Design 94
4.2.3 Mask Design 102
4.3 Testing and Characterisation 106
4.3.1 LIV Measurements 107
4.3.2 CV Measurements 110
4.3.3 Growth Reports 112
4.3.4 Up-Down Transitions 114
4.3.4.1 Wavelength Filtering 114
4.3.4.2 Maximised Transmission 116
4.3.4.3 Waveguiding 116
4.3.5 TLS Measurements 118
4.4 Discussion and Conclusions 121

5 Conclusions and Future Work 123
5.1 Summary 123
5.2 Conclusions 126
5.3 Future Work 127

List of Figures

1.1 Data growth . . . 1
1.2 Mach-Zehnder modulator schematics . . . 4
1.3 Integration techniques . . . 8
1.4 Structure Schematic . . . 10

2.1 Slab waveguide diagram . . . 17
2.2 Dispersion equation solutions . . . 19
2.3 Slab waveguide fundamental mode . . . 19
2.4 Overlap surface of slab waveguide modes . . . 22
2.5 Cross sections of overlap integral regions . . . 24
2.6 Taper shapes . . . 25
2.7 Overlaps along different taper shapes . . . 25
2.8 Transmission for different taper shapes . . . 28
2.9 Effective index vs. upper waveguide ridge width . . . 31
2.10 Coupling coefficients for different upper ridge widths . . . 35
2.11 Coupling fraction for different upper ridge widths . . . 35
2.12 Up-down waveguide diagram . . . 37
2.13 Mode solution preference for higher refractive index . . . 37
2.14 Mode solutions in various stacked waveguide geometries . . . 38
2.15 Overlap surface of up-down waveguide structure . . . 39
2.16 Taper shapes for up-down waveguide structure . . . 40
2.17 Upper waveguide transmission for different barrier thicknesses . 42
2.18 Transmission for different up-down waveguide taper shapes . . . 42
2.19 BPM simulation of up-down waveguide transition for different taper lengths. . . . 44
2.20 Transmission through up-down waveguide transition for different taper lengths. . . . 45
2.21 Grating coupler wavevector diagram . . . 47
2.22 Parameter surface for intermediate waveguide . . . 52
2.23 Transmission for variations about the ideal centre waveguide index 52
2.24 BPM simulation of 3WG up-down transition for different taper lengths . . . 53
2.25 Transmission for a quickly tapered upper waveguide before the transition region. . . . 54
2.26 Comparison of 2 and 3 WG up-down device . . . 55
2.27 Band-gap vs. lattice constant for III-V semiconductor alloys . . 56
2.28 Band-gap wavelengths for AlGaInAs compositions . . . 57
2.29 Refractive index vs. band-gap wavelength for InP lattice-matched AlGaInAs compositions . . . 58

3.1 Band diagram of p-substrate laser . . . 62
3.2 Doping profiles of the different p-substrate laser growths 64
3.3 Material test mask . . . 66
3.4 Ridge etch steps . . . 67

3.5 Oxide opening steps 68
3.6 Metal lift-off steps 69
3.7 Lasers under test for growth with reduced doping 71
3.8 Processed wafer using material test mask 72
3.9 OSA trace of a p-substrate laser for growth with reduced doping when biased and unbiased 73
3.10 LI measurements for different p-substrate laser growths 73
3.11 OSA traces of spectra from different p-substrate laser growths . 74
3.12 IV measurements of different p-substrate laser growths 75
3.13 Pulsed OSA trace of p-substrate laser for growth with reduced doping 77
3.14 SEM images of laser ridges 78
3.15 Pulsed LI of a p-substrate laser for growth with reduced doping 78
3.16 Theoretical depletion width vs. reverse bias for different doping concentrations 80
3.17 CV measurement set-up 81
3.18 Depletion width vs. bias for different n-i-p growths 82
3.19 ECVP of p-substrate laser for growth with reduced doping . . . 83
3.20 SIMS of successful n-i-p growths 84
3.21 Designed and measured doping profiles of n-i-p growths 85

4.1 Calibration of upper WG material 90
4.2 Calibration of lower laser material 90
4.3 Upper etch depth tolerance 92
4.4 Etch depth monitor 93
4.5 Thickness tolerance of lower WG cladding 94
4.6 Masks for up-down WG processing 103
4.7 Mask designs up-down WG test devices 104
4.8 Fabricated up-down WG test devices 105
4.9 IV measurements of upper and lower WGs 107
4.10 LI measurements of upper and lower WGs 108
4.11 FP cavities processed on upper and lower material 108
4.12 Pulsed LI measurement of upper and lower WGs 109
4.13 OSA traces of upper and lower WG emission 110
4.14 Depletion width measurements of different growth iterations . . 111
4.15 Calibration of grown lower active material with the upper layers removed 112
4.16 PL of repeated lower active material growth 113
4.17 Spectrum of repeated growth lower active FP cavity 114
4.18 Vertical transition filtered emission 115
4.19 Imaged and calculated mode shapes of upper and lower WGs . . 118
4.20 Reflectometry of up-down WG facet 119
4.21 Imaged TLS vertical transition 120
4.22 Wavelength dependence of the vertical transition 121

List of Tables

2.1 Up-down WG refractive index design 30
2.2 InP lattice-matched materials with suitable refractive indexes for vertical integration. 57

3.1 n-i-p laser epitaxial design 63

4.1 Up-down WG epitaxial design 88

I, Shane Duggan, certify that this thesis is my own work and I have not obtained a degree in this university or elsewhere on the basis of the work submitted in this thesis.

Shane Duggan

"It all sounds great when you say it like that.
The truth is most of that was just luck,
I didn't know what I was doing half the time,
and I nearly always had help–"

– Harry Potter, *in the Hog's Head*

Acknowledgements

Thank you very much, thank you very much, thank you very much, thank you!

Firstly, thanks to Frank for accepting me into his research group and aiding me in pursuing my dream, and for all the advice and assistance over the years. Thanks for melding the group together and for the biannual crokinole lunches at yours and Jo's.

Thanks to the Old Guard of IPG for welcoming the Next Generation and setting the precedent for a fun and friendly atmosphere. I guess it is the way of the world that now it is my time to enter the Old Guard, and pass from this place. To them and my fellow Next Generation: it has been an honour and a privilege serving with you these past years. When they sing songs of our deeds they'll tell of the courgettes in Warsaw, the promised return of the third and final Moises Day, all night long zombie board attacks, the grandeur of MKSE, and all our other adventures together; too numerous to scribe here.

Within the white walls of the canteen our lunch crew laughed and laughed to our hearts' pleasure, and recuperated from our woes. 'Tis unlikely I would've been here, to write this, without those lunches and extended coffee breaks.

I miss the after-PIC-meeting breakfasts on Wednesday mornings, when groups would merge and share stories, and plan to kart and fail to foot-golf.

Many others passed through the ranks of IPG and the Tyndall community, whether briefly or longer. To each gratitude is given, for shaking the order and brightening the days. I spent three fast years on the S+S Committee, and through it got to meet all manner of weird and wonderful people, and journey to otherwise unvisited places. Thanks to you all!

The fine fellows in Tyndall helped endure the trials there, but life also continues outside its boundaries. The joy of family is that you never have to thank them, they're stuck with you no matter what, so I don't express it as much as I should; here's a gigantic ould thank you! Can't imagine what I'd do without you.

There's also my old school buddies who provided a complete escape. We've stuck together still, though now it means trips to Londontown and board game and movie nights. Treasure the days, boys.

If this body of work had turned to fugazy, fugazi, then je ne regretterais toujours rien. On a summer's eve I joined some IPG laddies for a celebration, and met my bestfriend and love. The rest, as they say, is history.

– Shane Duggan
Corcaigh, 2 May 2019

Abstract

Data usage continues to rise exponentially with user demand, and the bandwidth of optical communications is reaching its limit. Spectrally efficient advanced modulation formats are being used to increase the data rate within the existing bandwidth. Mach-Zehnder Modulators achieve high spectral density by modulating both the phase and amplitude of light. At the moment, laser light sources and Mach-Zehnder Modulators are built discretely and packaged and coupled thereafter. Photonic Integrated Circuits (PICs) place multiple photonic components onto single chips, with the benefit of compactness resulting in lower cost through simpler coupling, lower power consumption, and volume manufacture. The difficulty faced by photonic integration is that different components require different material for their different functions, and so cannot be easily placed onto the same material substrate wafer. Existing methods use regrowth techniques to selectively replace material around the chip, but regrowth is expensive and time consuming.

This work vertically integrated a passive waveguide above an active waveguide using regrowth-free monolithic integration. The passive and active waveguides are designed for Mach-Zehnder modulator and laser material. The waveguides were processed on an InP platform, and consisted of AlGaInAs alloys. To our knowledge this is the first time a passive waveguide has been vertically integrated above an active waveguide for III-V semiconductors, and the first time two AlGaInAs waveguides have been vertically integrated, using monolithic regrowth-free techniques on InP.

Vertical coupling was performed through lateral tapers, and an isolation barrier between the stacked waveguides allows the vertical integration of already optimised discrete components without modification. As the isolation barrier deliberately reduces the coupling between the waveguides away from the transition region, a technique using a third passive waveguide in the barrier was used to increase the vertical coupling while maintaining isolation.

A regrowth-free vertical monolithic PIC was conceived, designed, grown, fabricated and tested to prove its operation. The two vertically stacked waveguides provide a solution for integrating active and passive material, so that a laser and Mach-Zehnder Modulator can be monolithically integrated to create a low cost advanced modulator to meet today's ever increasing data demands.

List of Acronyms

Acronym	Definition
ATG	Asymmetric Twin Waveguide
AWG	Arrayed Waveguide Grating
BPM	Beam Propagation Method
CMOS	Complementary metal–oxide–semiconductor
CV	Capacitance-Voltage
CW	Continuous Wave
DC	Direct Current
DFB	Distributed Feed-back
DUT	Device Under Test
DWDM	Dense Wavelength Division Multiplexing
DWS	Dual-Waveguide Structure
EAM	Electro-absorption Modulator
ECVP	Electrochemical Capacitance-Voltage Profile
EDFA	Erbium Doped Fibre Amplifier
EML	Electroabsorption modulated lasers
FP	Fabry-Pérot
GSG	Ground-Signal-Ground
IC	Integrated Circuit
IPG	Integrated Photonics Group
IV	Current-Voltage
LI	Light-current
MGVI	Multi-Guide Vertical Integration
MMF	Multimode Fibre
MMI	Mulitmode Interference Couplers
MPW	Multi-Project Wafer
MQW	Multiple Quantum Wells
MZI	Mach-Zehnder Interferometer

Acronym	Definition
MZM	Mach-Zehnder Modulator
OOK	On-Off Keying
OSA	Optical Spectrum Analyser
PARC	Passive Active Resonant Couplers
PIC	Photonic Integrated Circuit
PL	Photoluminescence
QAM	Quadrature Amplitude Modulation
QCSE	Quantum Confined Start Effect
QPSK	Quadrature Phase Shift Keying
QW	Quantum Well
QWI	Quantum Well Intermixing
SAG	Selective Area Growth
SCH	Separate Confinement Heterostructure
SEM	Scanning Electron Microscope
SFP	Slotted Fabry-Pérot
SIMS	Secondary Ion Mass Spectrometry
SMF	Single Mode Fibre
SMVI	Single-Mode Vertical Integration
SOA	Semiconductor Optical Amplifier
TAVI	Taper Assisted Vertical Integration
TLM	Transmission Line Measurements
TLS	Tunable Laser Source
TG	Twin Waveguide
VCSEL	Vertical Cavity Surface Emitting Lasers
WDM	Wavelength Division Multiplexing
WG	Waveguide
XRD	X-Ray Diffraction

List of Symbols

Symbol	Explanation
A	Area
A_i	Amplitude contributions
β	Propagation constant
c	Speed of light in vacuum
C	Capacitance
d	Core width
$\mathbf{E}$	Electric field
$\mathcal{E}$	Mode
ϵ	Permittivity
ϵ_0	Permittivity in vacuum
ϵ_r	Relative permittivity
η	Efficiency
ϕ	Phase
Γ	Confinement Factor
h	Planck's constant
I	Current
$\mathbb{I}$	Overlap integral
k	Wavenumber
κ	Coupling coefficient
L	Length

Symbol	Explanation
L	Optical Power
λ	Wavelength
Λ	Grating Period
μ	Permeability
μ_0	Permeability in vacuum
n	Refractive index
N	Doping concentration
ν	Frequency
ω	Angular frequency
P	Power
P	Perimeter
q	Charge
R	Resistance
t	Temporal dimension
u	Slowly varying electric field
V	Voltage
W	Width
x	Spatial dimension
y	Spatial dimension
z	Spatial dimension

List of Publications

Journal Articles

- S. P. Duggan, H. Yang, N. P. Kelly, L. Caro, M. Dernaika, M. Shayesteh, A. Gocalinska, K. Thomas, E. Pelucchi, B. Corbett, and F. H. Peters, "P-substrate InP-based 1.5μm lasers using an internal carbon-doped layer to block p-dopant diffusion", Microwave and Optical Technology Letters, vol. 60, no. 10, pp. 2363-2367, 2018.

Conference Proceedings

1. S. P. Duggan, H. Yang, A. Gocalinska, E. Pelucchi and F. H. Peters, "Vertically Coupled Monolithic Integrated InP-AlGaInAs Waveguides", Photonics North, Montréal, 2018.

2. S. P. Duggan, N. P. Kelly, L. Caro, M. Dernaika, M. Shayesteh, J. K. Alexander, H. Yang, A. Gocalinska, K. Thomas, E. Pelucchi and F. H. Peters, " Development of Inverted p-Substrate InP/AlGaInAs Lasers for Vertical Integration with Multiple Passive or Active Intrinsic Regions", 19th European Conference on Integrated Optics (ECIO), Eindhoven, 2017.

3. S. P. Duggan, P. E. Morrissey, F. H. Peters, "Taper Design for Vertical Coupling between Isolated Active and Passive Waveguides", 18th European Conference on Integrated Optics (ECIO), Warsaw, 2016.

4. S. P. Duggan, R. N. Sheehan, P. E. Morrissey, and F. H. Peters, "Design of Tapers for Up-Down Coupling Between Active and Passive Waveguides", Semiconductor and Integrated Opto-Electronics (SIOE'16), Cardiff, 2016.

5. S. P. Duggan, H. Yang, A. Gocalinska, E. Pelucchi and F. H. Peters, "InP-AlGaInAs Waveguides Monolithically Integrated by Vertical Coupling", Photonics Ireland, Cork, 2018.

6. S. P. Duggan, N. P. Kelly, L. Caro, M. Dernaika, H. Yang, M. Shayesteh, J. K. Alexander, A. Gocalinska, K. Thomas, E. Pelucchi and F. H. Peters, "P-Substrate Lasers for Vertical Integration of InP/AlGaInAs Waveguides", Photonics Ireland, Galway, 2017.

7. S. P. Duggan, R. N. Sheehan, P. E. Morrissey, and F. H. Peters, "Design of Up-Down Tapers between Active and Passive Waveguides", Photonics Ireland, Cork, 2015.

8. S. P. Duggan and F. H. Peters, “On-Chip Integration of Photonic Devices”, Institute of Physics (IOP) Ireland Spring Meeting, Limerick, 2018.
9. S. P. Duggan and F. H. Peters, “Monolithic Vertical Integration Of Optoelectronic Devices”, Institute of Physics (IOP) Ireland Spring Meeting, Dublin, 2017.
10. S. P. Duggan, R. N. Sheehan, P. E. Morrissey, and F. H. Peters, “Design Of Up-Down Tapers Between Active And Passive Waveguides”, Institute of Physics (IOP) Ireland Spring Meeting, Belfast, 2016.

Chapter 1

Introduction

1.1 Communications Growth

Technology has allowed people from all walks of life to communicate over vast distances while transmitting enormous amounts of data [1] and society now relies on fast and reliable information exchange [2].

As a result, data demands are rising exponentially [3–11] and the growth is expected to continue increasing rapidly [4, 12–16]. The ever increasing traffic in networks [17–19], due to this growth of the internet [20, 21], is exceeding even Moore's Law [22] and resulting in exascale datacentres [23]. Figure 1.1 shows the predicted continued growth of total global internet traffic [24].

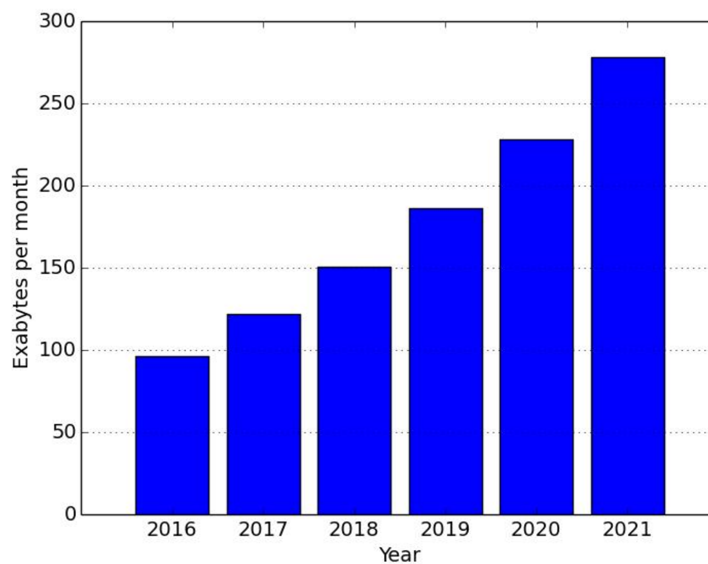

Figure 1.1: Predicted growth of total global internet traffic [24].

Bandwidth is the amount of data that can be transmitted in a fixed amount

of time [25]. As data demands rise, bandwidth continues to grow and is being used to unprecedented levels at an accelerated rate [19, 26–30]. More bandwidth is demanded by the growth of cloud computing, video streaming, big data, smartphone and multimedia applications, internet traffic, social networking, and the emerging internet of things [1, 2, 5, 10, 16, 22, 31–37].

The required bandwidth is beyond the capability of conventional electrical copper interconnects [10, 30, 38–41] which have resistance-capacitance (RC) delay and high power dissipation [41]. The benefit of electrical interconnects is that electrical circuits exploit complicated signal processing [4], but electrical CMOS scaling is expected to stop at 7nm technology due to the interconnects suffering from skin effects and large impedances at such a small scale [4].

Optical fibre has been established in broadband communications for decades [37, 42, 43], supplying the solution to high bandwidth [1, 18, 22, 23, 40, 44–46] and allowing transmission over long distances at high bit rates [31, 34, 44, 47]. The ever increasing amount of data traffic carried by optical fibres increases interest and dependence in the optical domain [6, 48, 49], because no other medium can support the demand on capacity, energy efficiency [2, 31, 44] and long distance transmission.

However, current network architectures are approaching their fundamental limits [47] and will not be able to keep up with bandwidth demand in the future [3, 20]. Fibre optic communications are reaching the maximum rate at which data can be sent with zero error [3]. The transmission windows in optical fibre at 1300nm and 1550nm [3, 50, 51] are being fully exploited and are reaching saturation based on current technology. While the fibre transmission window is much larger [52], only the narrower C-band is primarily used [53] at the 1550nm window, due to the bandwidth of erbium doped fibre amplifiers (EDFAs) which are needed to boost the optical signal for long range transmission [27, 52]. Fibre optic networks need to increase their capacity to offer a suitable communication infrastructure for the continued growth of the internet [5].

The high bandwidth demands lead to a need for spectrally efficient solutions [5, 27, 52, 54–60] with increased information spectral density [29, 61, 62]. Advanced optical modulation techniques utilise multiplexing [47], encoding data on amplitude, phase, polarisation and wavelength for every spatial mode [1, 52, 55, 63–65]. Otherwise more fibre would need to be deployed [5] which is not cost effective over long distances [47]. Low cost, and with it power, reliability and size requirements, are imposed on optical communication solutions [17, 37, 49].

For the highest data rates, high speed modulation schemes with low power consumption are required [17, 66]. 10Gb/s to 25Gb/s switching rates have been in use [26, 56, 67–70] and 50Gb/s to 100Gb/s are now required [26, 28, 31, 55, 64, 67, 69, 71–77]. Future data rate targets are 500Gb/s to 1Tb/s [34, 69, 73, 78] and these higher rates are only achievable at low cost with advanced modulation formats.

Among various existing modulation methods, on-off keying (OOK) is the most basic: simply turning on and off the signal [79, 80]. The simplest case uses modulated Fabry-Pérot (FP) lasers which are low cost [37, 81] and acceptable at low distances [8, 81], but are not suitable for long transmission at rates above 2.5Gb/s because modal dispersion corrupts the signal [8, 37]. Electroabsorption modulated lasers (EMLs) are currently used widely in long haul, and also in mid and short reach, communications [12]. EMLs typically consist of a DFB (distributed feed back) laser and an EAM (electro absorption modulator), and feedback to EMLs becomes a serious concern at speeds above 10Gb/s due to the sensitivity of the DFB lasers [12]. OOK can't be achieved cost effectively at higher rates, because it requires multiple transmitters to send multiple data streams [34]. Multimode fibre (MMF) can be used with a VCSEL (vertical cavity surface emitting laser) only over short distances; instead single mode fibre (SMF) is used with spectrally efficient transmission such as WDM (wavelength division mulitplexing) [20]. WDM sends information using different wavelength channels, so that multiple signals can be sent along the same fibre. Dense WDM (DWDM) further increases capacity by packing more wavelengths closer together and increasing the number of channels in the fibre.

A Mach-Zehnder Modulator (MZM) is a popular modulator because it allows independent switching of both the amplitude and phase of an optical signal [55]. The more spectrally efficient modulation format of QPSK (quadrature phase shift keying), and beyond to formats with higher orders of phase and amplitude, can be achieved using MZMs. QPSK is achieved by switching between four different phases, for a total of four data options. Each modulation carries two bits of data per symbol compared to one for OOK, requiring half the capacity [57, 60, 82]. The number of amplitude and phase values can be increased in the format termed QAM (quadrature amplitude modulation) to further increase the number of bits per symbol [5, 52, 60, 75]. While $LiNbO_3$ is an effective modulator material, it has the drawback of being large and requires a relatively large driver voltage [55, 56, 56, 82, 83]. Semiconductor MZMs on the other hand have a small size and low driving voltage, as well as high bandwidth [55, 56, 68, 82–89].

An MZM consists of a Mach Zehnder interferometer (MZI), or a pair of MZIs nested together. MZM example configurations are displayed in Figure 1.2. An MZI works by splitting light into two paths, modifying the phase of the light in those paths, and then recombining the light, as shown in Figure 1.2a. On a semiconductor platform, splitters and combiners are y-branches or mulitmode interference couplers (MMIs). The phase of the light is altered by applying biases to the arms. The recombined light intensity is dependent on the phase delay between each arm [90, 91], so that switching the phase in the arms between constructive and destructive interference alters the intensity [90–92]. In this way a BPSK transmitter can be achieved by having constructive interference at 0 and π phase differences, Figure 1.2b. Two MZIs can be nested together and phase shifted from each other by $\pi/2$, as in Figure 1.2c [52, 55, 56, 82, 92]. This arrangement gives the option of varying both the in-phase and quadrature components to create QPSK, illustrated in Figure 1.2d. Allowing further phase differences within the nested MZIs creates higher order QAM.

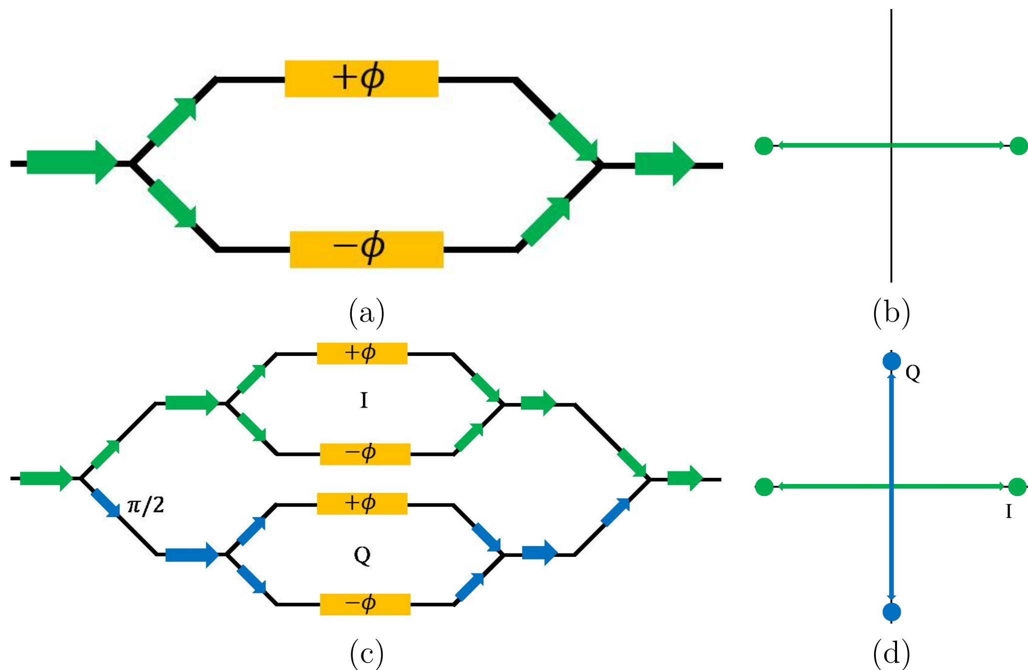

Figure 1.2: Schematic of MZM configurations. The device in (a) applies some phase change ϕ to the arms, and the constellation diagram in (b) shows the BPSK signal possible from the device, with the symbols π out of phase. The device in (c) nests two of the devices in (a) with a phase difference of $\pi/2$, so that there is an in-plane (I) signal and a quadrature (Q) signal. The constellation diagram in (d) shows the QPSK signal possible from this device.

1.2 Photonic Integration

Integrated optics enables the scalable capacity, high yield, and cost effective integration that sustainable communication requires [4, 38, 93].

The economical value from an integrated circuit (IC) must outweigh the cost of the integration itself [73], so integration methods should be simple and cost effective [94]. The energy consumption can be reduced by limiting the cooling capacity [31], and by reducing the number of power-hungry optoelectronic regenerators [95]. Avoiding electrical-to-optical conversions [5, 19, 46] also speeds up information processing and increases bandwidth [22, 46, 96]. Integration also provides lower maintenance costs [26].

Photonic integrated circuits (PICs) have emerged as a promising solution to alleviate the bandwidth bottleneck [97]. A semiconductor laser platform allows integration with other optical components, so that multiple devices are combinable onto a single chip [18, 19, 46, 56, 62, 98–100]. Otherwise many discrete components can be required for multiple functions, taking up a lot of space [101, 102]. Bulk components are expensive and susceptible to environmental factors such as vibrations [102]. Placing numerous components on a PIC allows them all to be connected by lithography, so they can be much more easily path-length matched for smaller delays, and they are so close that propagation losses can also be minimised [45, 101, 103]. PICs overcome sensitivity to the environment, including electromagnetic interference [45, 104], and a single cooler can be used for the whole chip [19]. Thus PICs provide functionality for complex systems [99, 102].

The source of most optical losses is in fibre interconnects between components [103] so their number should be reduced [9, 105–107], which further leads to reduced packaging costs due to less optical-electrical interfaces [23]. There is high coupling loss between fibres and chips, arising from the mode mismatch between them [44, 104, 108]. Even if the mode shape of the chip has been altered there will still be a mismatch in the mode size [44]. The alignment tolerances for fibre to chip are in the submicron range, which PICs can solve [40, 50, 104, 109]. Integration bridges the gap between micro- and nano-scale structures [110].

Device reliability is related to packaging and external factors [19]. Fewer chips means simpler assembly [18, 100] and with it cost reduction and performance enhancement [100, 103, 111]. PICs allow miniaturisation and can be volume manufactured at low cost to achieve scalability [9, 16, 23, 93, 100, 102, 103, 111–115].

Similar to electronics, a high density of devices are desired from PICs [66]. Power consumption can be reduced by placing optics very close to the signal

source, driving the need for the high density chips and packaging [20]. To maximise density, the miniaturisation of waveguide dimensions is critical [116]. The operating wavelength of $1.55\mu m$ determines the size of devices, resulting in overall dimensions of several hundred nanometers, which is larger than silicon waveguide dimensions [116, 117]. Cleaved facets can be removed through integration so that devices don't need to be placed on the edge of the chip, increasing the density of PICs across the entire chip [118, 119]. State of the art photonic integration allows hundreds of photonic elements on footprints less than $1mm^2$ [78, 120, 121].

Thus PICs are lower cost, compact and highly reliable. They have low power consumption, simpler coupling and simpler packaging, and reduced manufacturing time. Along with their small footprint and weight reduction, PICs have large bandwidth, low optical delays, low transmission loss, high accuracy and enhanced performance. [4, 5, 12–14, 16, 18, 19, 23, 28, 40, 45–48, 50, 52–54, 56–58, 63, 66, 68, 72, 78, 95, 96, 98–103, 109, 111–115, 120, 122–148]

All components on a PIC must work normally as if discrete [135, 149], but some compromise may be tolerable if there are improvements in other aspects [132].

While this work focuses on telecommunications, PICs also have a wide range of applications in fibre sensing, datacoms, antenna systems, medical diagnostic, metrology, lighting and more [23, 42, 100, 111, 150].

PICs are similar to electrical ICs, but there are differences that have prevented the same success [42, 45, 103, 117, 121]. The reason is partly market based, with a lack of industry pull [16, 45]. Technology barriers with PIC materials such as InP have also slowed progress [16, 45]. Photonic devices are based on binary, ternary and quaternary materials that are more difficult to control than Si alone [117]. Photonics requires many components, while electronics only requires transistors and passive components [103, 112, 147]. While there are many papers on PICs, there are few commercial devices [121], and the existing commercial sales of PICs are dominated by InP-based solutions [132].

InP-based devices are mature and have been deployed in the field for some time, over two decades [111, 145]. The III-V semiconductor InP is the most promising platform for the fabrication of complex and compact optical circuits, providing complete functionality [66, 67, 78, 111], allowing light propagation, amplification, detection and fast modulation on a single chip [46, 67, 111]. InP-based PICs are an especially attractive platform for the $1.55\mu m$ transmission wavelength [66, 103], and are further capable of providing wavelength ranges from $1.3\mu m$ to $1.6\mu m$ [129, 134]. InP gives access to several electro-optic effects [97],

such as carrier injection, Quantum Confined Start Effect (QCSE), Kerr Effect, Pockels Effect, and thermal tuning [97]. The electro-optic effects can be used to change the refractive index to tune the spectral response of devices [97]. Thermal tuning is slow, and actually acts as a fundamental limit to PICs because they are inherently sensitive to thermal variations [97]. The InP platform, possessing electrical functionality, also has the potential for integration with CMOS [100, 103].

1.2.1 Monolithic Photonic Integration

PICs require many different devices with distinct functionality, both active and passive, which is difficult [16, 103, 104, 113, 134, 147–149, 151, 152]. In this work, active shall be referred to as any section that provides gain or absorption. In some definitions active also includes electro-optic effects as found in modulators, but in this work those will be included in the definition of passive, which simply refers to any section that does not supply gain or absorption at the operating wavelength [127]. Active and passive devices require different band-gaps because they need to be absorbing and non-absorbing respectively at the operating wavelength [50, 103, 134, 147, 152]. Passive devices are transparent to light [50] and should have a bandgap wavelength hundreds of nanometers blueshifted relative to the operating wavelength [153]. Active devices require material that can provide gain [132], higher doping and thinner layers for light confinement, which is then detrimental to passive devices [103].

Monolithic integration creates a PIC from a single crystal, bringing photonic integration to its most extreme advantages, allowing the highest density of complex components [150] and placing many discrete active and passive functions into a single chip [97, 123].

InP remains the material of choice for integration of active and passive materials [145], being the only platform that offers to support full monolithic integration [100]. Epitaxy is limited by lattice mismatching [154], but as mentioned previously, InP is compatible with ternary and quaternary compounds that can be lattice matched to provide a wide range of band-gaps.

Both quaternary compounds AlGaInAs and InGaAsP enable efficient light sources [134, 154]. InGaAsP and AlGaInAs can also be adjusted to obtain both passive and active material while maintaining lattice matching to InP [50, 125]. AlGaInAs is preferred because it is reliable at high temperatures, and has high speed, and also a large gain [21, 70, 70, 70, 81, 98, 155–158, 158, 158]. AlGaInAs has become the standard material for long wavelength laser diodes as a result [74].

AlGaInAs also has the advantage of comprising only a single group V element which allows easier growth [74].

There are different integration techniques for PICs, including [125, 159] etch and regrowth, epitaxial regrowth [54, 160], butt joint regrowth [132], quantum well intermixing (QWI) [54, 132, 137, 159, 160], selective area growth (SAG) [54, 132, 137, 153], offset quantum wells [132, 137], and hybrid integration [50, 54, 160]. Most of these integration techniques are illustrated in Figure 1.3.

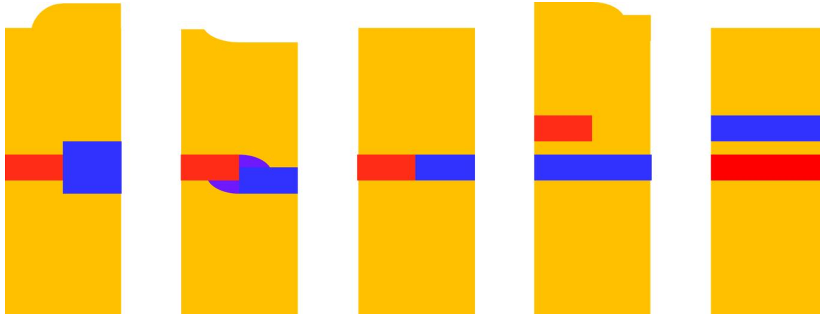

Figure 1.3: Existing monolithic integration techniques. From left to right: etch and regrowth where material is etched away and regrown with a different material, SAG where material is selectively grown around the wafer, QWI where the core bandgap is selectively altered through intermixing, offset quantum wells where cores are placed vertically and the active core is etched away in the passive sections, and the stacked waveguides of this work.

Etch and regrowth techniques etch material away and regrow a different material in that position, which then suffers from a mismatch of thicknesses and refractive indices. During epitaxy SAG selectively grows material around the wafer, but also suffers from thickness and index mismatches. QWI alters the bandgap of the core by intermixing material post-growth, and while this removes any thickness mismatch it instead restricts the core to a single thickness across the wafer, which may not be ideal for each application. Offset quantum wells are made by epitaxially growing different cores vertically above each other, and then etching away the active material in the passive sections. The offset quantum wells allow each waveguide to be optimised discretely, but if the vertical separation isn't large enough there can be overlaps between the light in each core which reduces performance.

The existing integration methods require long and complex fabrication processes [54, 103, 132, 161]. This complex fabrication can limit the functionality required for advanced modulation formats, and incurs high costs [137, 160, 162]. Existing methods require regrowth steps [98, 118] and could require five or more regrowths to achieve the desired band-gaps [132]. Regrowth is expensive and can result in low yields [107, 107, 115, 115, 152, 152, 153, 159, 162–164]. For Al-

containing alloys, regrowth is not a good option as it oxidises rapidly [21, 165]. The existing methods regrow and place devices laterally, so that they must share thicknesses [103], but the optimal thicknesses of cladding layers can differ by more than a micron [166]. Thickness mismatches can cause parasitic reflections as the light transitions between mediums, which can disturb the desired behaviour of the circuit [147, 167, 168]. The cost of fabrication increases with the number of growth steps so the number of growth and processing steps should be minimised [50, 93, 169].

Regrowth-free semiconductor lasers have relatively simple fabrication, and can be fabricated using standard lithography, [53, 98, 112, 146, 148, 151, 161, 164, 170–172] unlike regrowth techniques where high resolution lithography is usually required [53, 118]. Removing the regrowth steps permits separation of the fabrication process and epitaxial growth [141, 162], allowing more freedom in the laboratory processes. The obvious difficulty with regrowth-free fabrication is that active and passive devices still require different materials and so need different growths of some form.

1.2.2 Vertical Monolithic Photonic Integration

The alternative monolithic integration technique investigated in this work uses regrowth-free vertical integration [103, 160, 169, 173]. The technique has previously been termed single-mode vertical integration (SMVI) [160], twin waveguide (TG) [148], asymmetric twin waveguide (ATG) [10, 94, 125, 138, 144, 147, 160, 172, 174–176], multiguide vertical integration (MGVI) [93, 129, 131, 141, 160, 162], taper assisted vertical integration (TAVI) [160], dual-waveguide structure (DWS) [130], and passive active resonant couplers (PARC) [153].

Vertical monolithic integration is achieved by a one-step epitaxial growth [93, 106, 129, 131, 138, 139, 159, 161, 162, 169, 174, 176]. Yield and cost constraints associated with regrowth are eliminated and all features are defined by postgrowth patterning [93, 129, 151, 162, 177]. Vertical integration allows an additional degree of freedom [106, 169, 178] compared to lateral integration. The major advantage to regrowth-free vertical monolithic integration is that each waveguide can be optimised independently [106, 113, 125, 138, 151, 153, 160].

The concept of generic integration exists already for fabrication based on regrowth, implementing well-characterised standardised building blocks on multi-project wafer (MPW) runs that allow low cost access to foundries [67, 147, 164]. The eventual aim is to be able to arbitrarily combine customisable photonic devices, similar to the case in CMOS for electrical components [147]. Vertical

integration further projects a universal integration platform, allowing stacking of completely arbitrary waveguides that have different active and passive functions and materials.

The coupling between active and passive sections is limited [138]. Mode transitions between the vertically stacked waveguides are performed by lateral tapers [10, 93, 138, 151, 159, 174, 175]. Lateral tapers are used because they can be defined with post growth patterning to avoid any regrowth steps. Tapers change the size and shape of an optical mode [179], due to changing of the effective refractive index as the geometry of the structure is altered. For mode transitions between vertically integrated waveguides, the upper waveguide is changed to increase the lower guide's confinement [137] and reduce the upper guide's. After some critical upper waveguide width, the mode will be preferentially guided in the lower waveguide and the vertical transition will be complete. The taper can be reversed to transition light back from the lower to upper waveguides. Figure 1.4 illustrates the mode transition achieved through post-growth defined lateral tapers, showing the mode confined in the upper waveguide at wide ridge widths, mid transition between the guides as the taper narrows, and finally confined to the lower waveguide alone. In the middle of the structure of Figure 1.4 none of the upper waveguide remains and the active mode can operate as if discrete. The taper can be reversed to incite a transition back vertically upward into the upper waveguide.

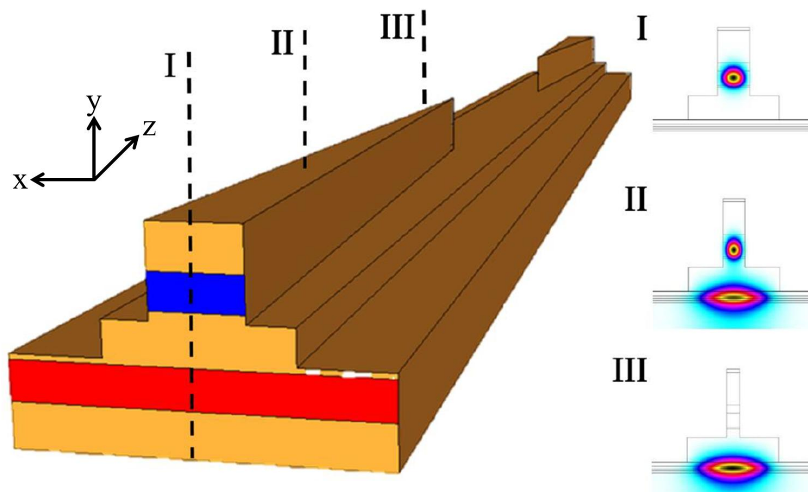

Figure 1.4: A schematic illustrating the mechanism of vertical integration and coupling investigated in this work. The upper blue core is passive relative to the lower red active core. Sections I to III provide mode slices at different points along the propagation in the taper.

In order to reduce absorption losses in the transition, the aim is to minimise

the taper length [94]. There are two types of mode couplers, adiabatic and resonant [137, 180–182].

Resonant couplers can be made very short [137, 138, 180]. However, it is difficult to determine the exact beat length of the mode transition [181, 182], and resonant couplers have tight restrictions on fabrication dimensions due to their strong wavelength dependence [94, 125, 137, 138, 180].

Adiabatic couplers are based on the evolution of a mode while minimising coupling to other modes [179, 181–184]. The system changes gradually in device geometry to allow adiabaticity, so the cross section of the waveguides must be altered very slowly [94, 138, 179]. Thus adiabatic couplers require a longer length [10, 113, 115, 137, 138, 161, 180–185], around $400\mu m$, resulting in a large size and absorption losses [125, 181, 182] and with it a reduction in device density [181, 182, 184]. The larger size of the device leads to a higher probability of material and fabrication defects [182]. Additionally, these tapers require submicron tips [10, 107, 113, 115], which are difficult to achieve with standard lithography [107, 115].

Loss mechanisms in tapers include free carrier absorption due to doping and carrier injection, sidewall and surface scattering, modal mismatch and intraband absorption due to unpumped QWs [168]. However, losses are less than the 2dB coupling loss from other integration techniques [23] and the 6dB from an abrupt active to passive transition [177]. If the taper is performed in passive layers then absorption losses are not such an issue. Adiabatic couplers have more relaxed fabrication tolerances and larger bandwidth [137, 180, 184, 185].

Layer thicknesses determine the vertical coupling strength and have the benefit of being relatively easy to control [106, 169]. The stacked waveguides cannot be placed too close together or there will be modal oscillations between the coupled waveguides [10, 177]. A thick InP spacer layer between the active regions can be used to prevent coupling between the waveguides [186]. Cladding layers are usually about $1\mu m$ thick to minimise overlap and absorption by contact metal, so a similar thickness should be required to separate the integrated waveguides, but such a thick barrier makes a taper coupler inefficient [151].

1.3 Thesis Motivation

All previous works for vertical mode coupling have placed the active waveguide above the passive [93, 94, 113, 129, 175, 177] and the active layers are removed in the passive sections [10, 147, 159] so that the mode in the passive waveguide is

not absorbed by the absorbing active material above it. In this work the ordering of the stacked waveguides is swapped for the first time. A passive waveguide is placed above an active waveguide.

The passive material is to implement a Mach-Zehnder Modulator (MZM). The benefits of MZMs were outlined previously, chiefly that they allow modulation of both amplitude and phase independently, leading to higher spectral density that is required by the limited bandwidth necessitated by exponential telecommunication growth.

A high speed MZM is more difficult to fabricate than a laser. A laser cavity can consist of a simple straight waveguide and only one electrical metal contact to provide gain. An MZM on the other hand features multiple waveguides and splitters, along with multiple metal contacts. The purpose of an MZM is for high speed modulation, and so is of primary importance in the fabrication, while the laser below only needs to produce a continuous wave (CW) light source.

Thus, it is beneficial to place the MZM on the summit of the stacked waveguide structure, so that it does not suffer through more fabrication steps than it needs to. Each fabrication step has the potential to introduce errors and defects, so by placing the MZM on top it will only experience the minimum steps required to define it, but not those of the laser beneath as well. Furthermore, and perhaps most importantly, in order to achieve high speed operation an MZM needs to be planarised, and this would be difficult to achieve if it were buried underneath another waveguide.

Along with the MZM, it is also advantageous to have the passive layers on top to allow easier implementation of a host of other passive components. These passive components might include bent waveguides, MMIs, arrayed waveguide gratings (AWGs), Echelle gratings, tapers, and others, whereas active components will be limited to relatively uncomplicated waveguides for lasers, SOAs, VOAs and detectors.

By placing the passive waveguide above the active waveguide, the active layers can no longer be removed, as has been performed in all other works. Instead, the barrier layers between the stacked waveguides need to be thick enough to isolate the mode of the passive waveguide from that of the absorbing active core below. As stated already, photonic integration should still permit the integrated devices to function as well as in their discrete devices. Thus the barrier layer is actually necessary and crucial for effective monolithic integration. Previous work has neglected a proper barrier layer because the passive waveguide still functioned tolerably after the upper active waveguide was removed. In those cases the passive

waveguide was typically a spot size converter for external coupling to optical fibre, rather than a high speed modulator as in this case, and partial performance is no longer tolerable.

As far as can be determined, this work presents the first regrowth-free monolithic vertical integration of multiple AlGaInAs waveguides. Previous works used AlGaAs [160, 162, 173] and InGaAsP [10, 94, 103, 125, 130, 138, 144, 147, 148, 153, 169, 172, 174–176]. An active AlGaInAs waveguide has previously been vertically integrated above a passive InGaAsP waveguide [93, 131, 141], but not with another AlGaInAs waveguide as in this work.

While this work focuses on telecommunications and the monolithic integration of a laser source and an MZM to achieve integrated advanced modulation formats, the same vertical coupling technique could be utilised for integrating any other photonic system for other applications.

1.4 Thesis Outline

This Chapter 1 has introduced an overview of the challenges of exponential data growth and how telecommunications is overcoming it. PICs are foundational to the next generation of optical communications, providing many benefits such as cost reduction, lower power consumption, compactness, robustness and volume manufacture. A big challenge for PICs is integration of active and passive materials that are inherently different. Complete integration was achieved in this work through regrowth-free vertical monolithic integration.

Chapter 2 outlines waveguiding in PICs, and predicts the exact structure required for vertical integration using theory and simulations. The optimum taper shape was found that can alter the mode shape with minimal loss, and perform the most efficient vertical coupling between stacked waveguides. The barrier thickness required to isolate the stacked waveguides was determined, and a coupling technique that allows a mode transition across this thickness was imagined, predicted with simulations and created. The epitaxial layer structure of the PIC is outlined and modified for effective light guiding while maintaining performance equivalent to discrete components.

Chapter 3 investigates the lower laser of the vertically integrated PIC. Due to the stacking of the waveguides, the lower waveguide must be inverted from its usual configuration, which led to growth and fabrication problems on an unforeseen magnitude. The growth structure is outlined and was modified to overcome its failures. Modifications were achievable due to a host of material test

structures that were designed to characterise the lasers, and used to prove that inverted lasers are suitable for further vertical monolithic integration, operating equivalently to standard n-substrate lasers.

Chapter 4 incorporates the laser structure of Chapter 3 into the coupling designs of Chapter 2. The full stacked waveguide structure is outlined and was grown and fabricated with custom processing steps newly developed for the vertically integrated devices. The processing steps are outlined along with test structures that were designed to prove vertical mode transitions between the stacked waveguides. These test structures were tested and characterised to indeed prove a vertical mode transition. The performance of the stacked waveguides is analysed using the results, and compared to theoretical predictions such as those made in Chapter 2.

Finally, Chapter 5 presents overall conclusions from the work within this thesis, and presents future directions. Contributions that performed well are highlighted as well as areas for future work, where the performance of the vertical monolithic PIC could be enhanced.

Altogether, this thesis brings regrowth-free monolithic vertically integrated passive above active AlGaInAs-InP waveguides from conceptual design to experimental realisation.

Chapter 2

Up-Down Waveguide Coupling Theory and Simulations

The previous chapter outlined how monolithic PICs provide solutions to the challenges facing optical communications. This chapter shall outline how a PIC is designed, beginning with the wave equation and expanding it from 1D through to a full 3D study of the structures. Both analytical and numerical theory and simulations are used and compared to provide as complete an understanding of PIC design as possible. As this work investigates vertical monolithic integration, tapers are studied in detail as they provide the method of achieving vertical coupling. Beyond the coupling design, the material composition of the PIC is also determined in order to realise fabricated and functioning devices in succeeding chapters.

2.1 Waveguide Tapers

2.1.1 Waveguides

A waveguide supports the propagation of light. In the case of semiconductor devices, the waveguide is made up of layers of semiconductor material, each with different refractive indices. The stacked layers are epitaxially grown to make up a slab waveguide.

The wave equation can be derived from Maxwell's Equations to be [90, 187–189]

$$\nabla^2 \mathbf{E} = \epsilon \mu_0 \frac{\partial^2 \mathbf{E}}{\partial t^2} \tag{2.1}$$

for the electric field $\mathbf{E}$, and similarly for the magnetic field. There is no gradient in the permittivity ϵ for a step-index structure such as a slab waveguide, as

there are discrete jumps from section to section and constant thereafter. The wave equation can be solved by separation of variables x, y, z, t so that the vector equation becomes four scalar equations, one in each dimension. Taking the z-direction as an example, we separate time t from the spatial coordinates x, y, z so that

$$E_z = \mathcal{E}_z\left(x, y, z\right) T\left(t\right) \tag{2.2}$$

Insertion into Eq. 2.1 allows the spatial and time components to be split

$$\frac{\nabla^2 \mathcal{E}_z}{\mathcal{E}_z} = \frac{\epsilon\mu_0}{T}\frac{d^2 T}{dt^2} = -k^2 \tag{2.3}$$

and each side of the equality must equal a constant $-k^2$ as each is independent of the other. This Eq. 2.3 supplies simple harmonic oscillator equations for the time

$$\frac{\partial^2 T}{\partial t^2} + \frac{k^2}{\epsilon\mu_0} T = 0 \tag{2.4}$$

and for the space, called the Helmholtz equation,

$$\nabla^2 \mathcal{E}_z + k^2 \mathcal{E}_z = 0 \tag{2.5}$$

The time dependent simple harmonic oscillator Eq. 2.4 can be solved using the ansatz $T = A_\pm e^{\pm i\omega t}$ which supplies the meaning of the constant k through

$$k^2 = \omega^2 \mu_0 \epsilon = n^2 \frac{\omega^2}{c^2} \tag{2.6}$$

the wavevector for light with angular frequency ω in each region with refractive index n.

The Helmholtz equation, Eq. 2.5, can be solved by separation of variables again. If the propagation is predominantly along one direction, termed the z-direction, then it can be separated so that

$$\mathcal{E}_z = \mathcal{E}\left(x, y\right) Z(z) \tag{2.7}$$

so that just as when splitting the temporal and spatial components in Eq. 2.3, each spatial component must now equal constants which together sum to k. The z propagation direction yields

$$\nabla^2 Z + \beta^2 Z = 0 \tag{2.8}$$

the solution of which is, similarly to the temporal solution, $Z = B_\pm e^{\pm i\beta z}$.

All of the previous allows the forward travelling electric field to be expressed by

$$\mathbf{E} = \mathcal{E}\,(x, y)\, e^{i(\beta z - \omega t)} \tag{2.9}$$

The time-independent wave equation, Helmholtz equation, in a slab waveguide becomes

$$\nabla^2 \mathcal{E} + (k^2 - \beta^2)\mathcal{E} = 0 \tag{2.10}$$

where $\mathcal{E}$ is the electromagnetic field in the perpendicular directions to propagation. This perpendicular field pattern is called the mode, supplying supported light in our structures.

If we are dealing with epitaxial layers stacked above one another, as illustrated in Figure 2.1, then the problem reduces to 1D in the vertical x plane and the wave equation becomes

$$\frac{\partial^2 \mathcal{E}}{\partial x^2} + (k^2 - \beta^2)\mathcal{E} = 0 \tag{2.11}$$

where k is the wavenumber in the medium and β is the propagation constant of the mode.

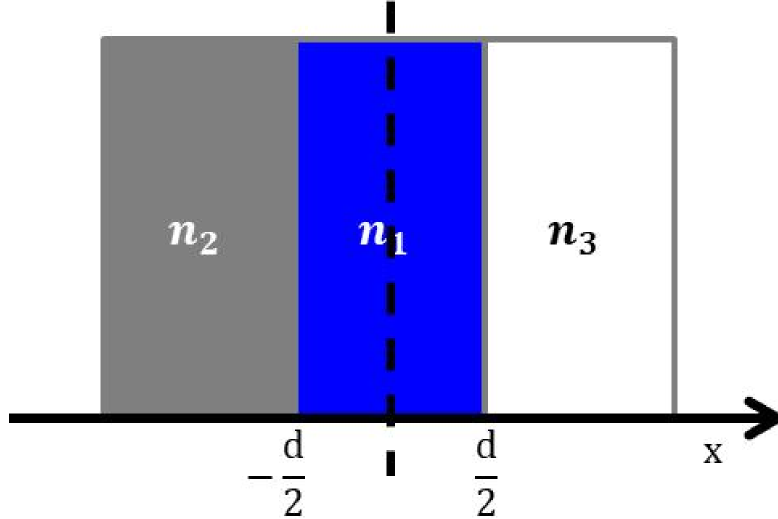

Figure 2.1: An antisymmetric slab waveguide consisting of a core with refractive index n_1, a substrate with refractive index n_2 and cladding with refractive index n_3.

The solution to the wave equation for a core width d centred at $x = 0$ is

$$\mathcal{E} = C_{TE} \begin{cases} \cos(\frac{hd}{2} - \psi)\exp(q(\frac{d}{2} - x)) & x > \frac{d}{2} \\ \cos(hx - \psi) & -\frac{d}{2} < x < \frac{d}{2} \\ \cos(\frac{hd}{2} + \psi)\exp(p(\frac{d}{2} + x)) & x < -\frac{d}{2} \end{cases} \tag{2.12}$$

where

$$\begin{aligned} h^2 &= k_1^2 - \beta^2 \\ p^2 &= \beta^2 - k_2^2 \\ q^2 &= \beta^2 - k_3^2 \\ \tan(2\Psi) &= \frac{h(p-q)}{(h^2 - pq)} \end{aligned} \tag{2.13}$$

for k_1 the wavenumber in the medium with refractive index n_1 etc. and C_{TE} is a normalisation constant enforcing the power flow across all x is equal to unity. β can be solved for through the so called dispersion equation [91] which is attained by using the continuity of $\mathcal{E}$ across the boundaries [187, 190]

$$(h^2 - pq)\sin(dh) - h(p+q)\cos(dh) = 0 \tag{2.14}$$

This transcendental equation must be solved numerically and due to the periodicity of the trigonometric functions involved it produces multiple results corresponding to multiple modes, Figure 2.2. To aid computational scripts that are used to numerically solve this equation it can be recast as

$$d = \frac{\arctan\left(\frac{p}{h}\right) + \arctan\left(\frac{q}{h}\right)}{h} \tag{2.15}$$

Thus for given values of d corresponding values of p and q and thus β can be calculated.

By finding the propagation constants β for core widths d the electric field $\mathcal{E}$ can be constructed at points along x using Eq. 2.12. A plot of one such field is shown in Figure 2.3. The full width of the slab should be chosen to be significantly larger than the core region so that the mode has decayed by the time it reaches the edge of the computational domain.

In 3D there may be an index change in two dimensions simultaneously. In that case the wave equation becomes more complicated to solve. However if the change is predominantly in only one dimension then the effective index method [91, 188] can be used to reduce the wave solution to the 1D case outlined above. Firstly, the direction with the least waveguiding is solved in each region. The resulting propagation constant is converted to an effective index through $\beta = n_{eff}k_0$, where k_0 is the vacuum wavevector where $n = 1$ from Eq. 2.6. The effective indices then become the indices of the cladding for the wave solution in the perpendicular direction that is of interest, which in turn leads to an overall effective index for the structure.

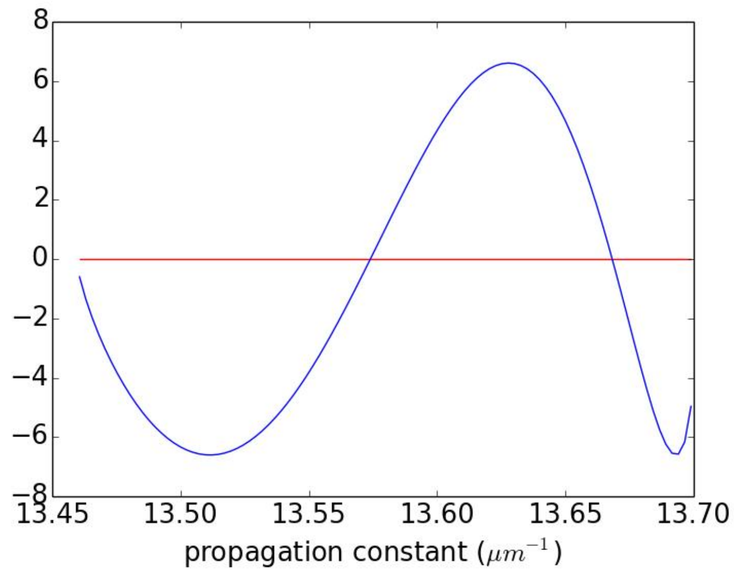

Figure 2.2: The value of the dispersion equation at different propagation constant values. The roots of the curve give the acceptable values of the propagation constant β for a guided mode. The largest value of β corresponds to the fundamental mode.

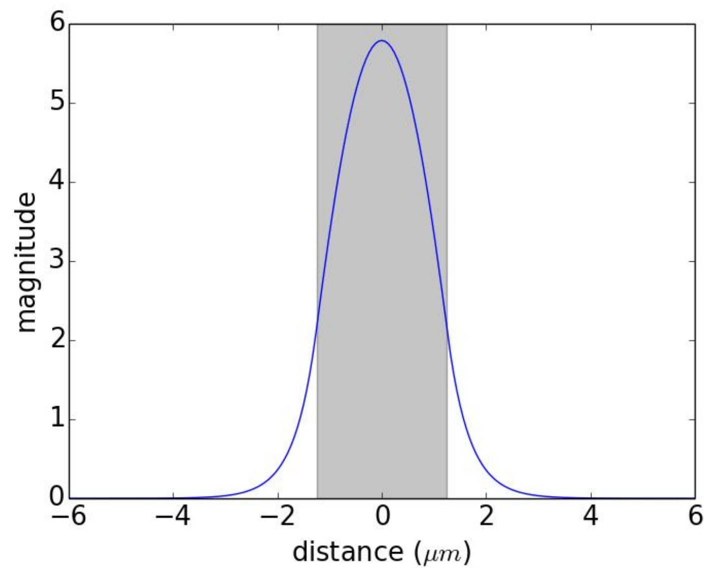

Figure 2.3: The fundamental mode of a slab waveguide. The shaded section illustrates the core region.

By examining Eq. 2.13 it can be seen that the supported mode's propagation constant, and with it the effective index, must lie $k_2, k_3 < \beta < k_1$ so that the values of h, p, q are real. This requires the index n_1 of the core with wavevector k_1 to be the highest. Also, the wave expression in Eq. 2.12 shows explicitly that the mode is centred in the core region $-\frac{d}{2} < x < \frac{d}{2}$ with the highest index, and decays into the cladding. The meaning is that the mode is centred in the core region that has the highest refractive index. This is of note and becomes important when multiple waveguide cores are close together. The dispersion equation, Eq. 2.15, can be solved with the bisection method, for example, knowing that for a guided mode the lower bound is the greater of k_2 and k_3 and the upper bound is k_1, with the dispersion equation monotonic between these.

By looking at the definitions of p, q in Eq. 2.13 it can be seen they are maximised for the largest β. Thus in the cladding regions, $|x| > \frac{d}{2}$, the mode reduces most abruptly for the largest β, meaning that the mode is most confined within the core region. The fundamental mode is described by the lowest value of h so that the wave solution in the core, Eq. 2.12, varies the least along x. The lowest value of h also corresponds to the largest value of β. Thus the fundamental mode is the most confined. The magnetic field solution includes a refractive index ratio factor of the cladding to core indices, which reduces its propagation constant and results in the magnetic field being less confined than the electric field.

The confinement factor of the mode is important as it provides the ratio of power within the waveguide to the total power. As its name suggests, it expresses how well confined the mode is within the waveguide. Higher confinement factors are beneficial when trying to supply gain from the waveguide to the mode, as more of the mode will experience the gain. The confinement factor is expressed by

$$\Gamma = \frac{\int_{-d/2}^{d/2} |\mathcal{E}|^2 \, \mathrm{d}x}{\int_{-\infty}^{\infty} |\mathcal{E}|^2 \, \mathrm{d}x} \tag{2.16}$$

As mentioned above, lower order modes are more confined than higher because, for mode number m, $\beta_m > \beta_{m+1}$ so that $h_{m+1} > h_m$ and $p_{m+1} < p_m, q_{m+1} < q_m$. Lower order modes reside more within the core.

2.1.2 Tapers

A taper is a continuing change in the dimension of a waveguide. A taper can refer to either a narrowing or widening waveguide, and generally can apply to any direction. The most common taper direction is lateral, so that the waveguide core thickness remains constant but its width is altered. Physically it is very

difficult to alter the thickness of a waveguide core, requiring regrowth steps that are expensive and hard to control [107, 107, 115, 115, 152, 152, 153, 159, 162–164]. Lateral feature definition, on the other hand, is achievable through standard UV contact lithography processing steps, which forms the crux of monolithic photonic integration's advantage [53, 98, 112, 146, 148, 151, 161, 164, 170–172].

Section 2.1.1 outlined the 1D mode solutions in a slab waveguide. As the waveguide dimensions change, the supported mode of Eq. 2.15 will likewise change. In the case of actual physical devices it is the width of the core which changes. As there is only a change in one dimension, the 2D wave equation can be reduced to 1D using the effective index method, discussed in Section 2.1.1. The vertical slabs either side of the core width can first be solved to find their effective index, and then those effective indexes can be taken as the cladding for the changing width problem. Typically the configuration remains a symmetric slab waveguide, as the etch depths defining the ridge width are the same on either side.

When a mode leaves one region and enters a different geometry, it means that it is no longer completely supported; it is no longer a perfect solution to the wave equation in that region. There will be some mode mismatch with the new geometry's mode solution, resulting in loss. The mode overlap, also termed the overlap integral, between the fields $\mathcal{E}_z$ and $\mathcal{E}_{z+\Delta z}$ at positions z and $z + \Delta z$ with different core widths can be expressed by [91, 191]

$$\mathbb{I} = \frac{\int \mathcal{E}_z \mathcal{E}_{z+\Delta z} \,\mathrm{d}x}{\left(\int \mathcal{E}_z \mathcal{E}_z \,\mathrm{d}x \cdot \int \mathcal{E}_{z+\Delta z} \mathcal{E}_{z+\Delta z} \,\mathrm{d}x\right)^{1/2}} \tag{2.17}$$

from which it can be seen that when $\mathcal{E}_z \neq \mathcal{E}_{z+\Delta z}$ the overlap is no longer unity and there is loss.

When designing a taper the mode overlap should be as close to unity as possible to make the modal transition adiabatic, having as close to no energy loss as possible in the transition. This is typically achieved by altering the dimension of the waveguide extremely slowly so that the mode changes very little. The slower the dimension of the waveguide changes the longer the taper becomes, and this is contrary to the minimisation aims of PICs. An ideal solution has next-to-no loss while simultaneously being very short. In addition, there is a length dependent loss within the material so that making short structures is advantageous.

Many taper shapes have been examined to find a geometry that satisfies the low loss and short criterion. These include linear, parabolic, exponential, Gaussian, two-step linear and so on. The impact such taper shapes will have on mode

propagation can be seen by looking at the modal overlaps of slab waveguides with different core widths. This is shown within Figure 2.4 where each point provides the modal overlap between two slab waveguides with different widths.

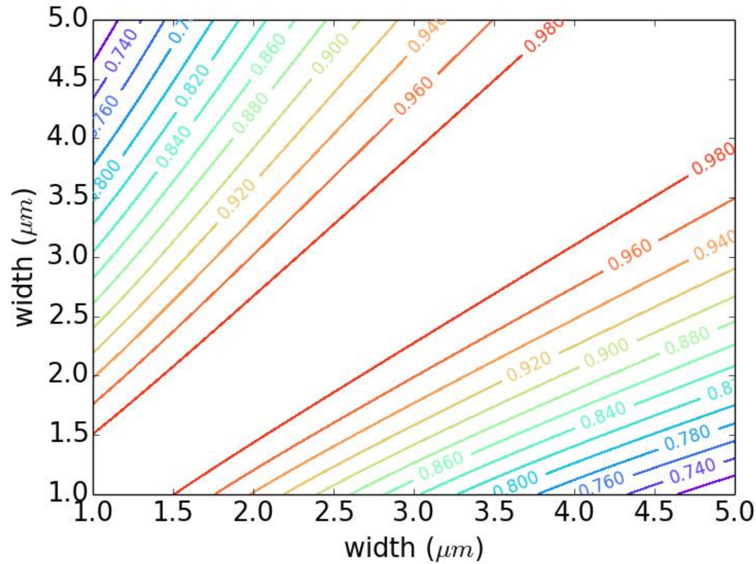

Figure 2.4: A surface of the overlaps between the fundamental modes of slab waveguides with different core widths. Each point provides the overlap between two waveguides with given widths, and the contours show regions of constant overlap value.

At wider core widths the overlap between modes is higher than between narrower widths. Thus, it is beneficial to remain in the wide core region longer because the losses are less. Many taper geometries depend on the change in width becoming slower as the losses become larger, that is as the taper narrows. Typical taper shapes often have positive curvature so that the slope of the change in width increases with distance, meaning that the change in width is slower when the width is narrow. As will be discussed in the next Section 2.1.3 this methodology may not be effective.

2.1.3 Constant Overlap Tapers

An alternative definition of adiabaticity in tapers is that the loss along a taper is constant [147, 179]. With that definition in mind a new taper shape design was examined that had a constant overlap between the mode solution at each point along the waveguide taper.

Eq. 2.17 supplies an expression for the overlap integral $\mathbb{I}$ which can be set equal to a constant, while Eq. 2.12 expresses the solutions of the modes at each

waveguide width. By inserting Eq. 2.12 into Eq. 2.17 an analytical expression for the overlap integral between slab waveguide cross sections can be obtained with reference to Figure 2.5, with the subscripts 1 and 2 denoting the mode solution at positions z and $z+\Delta z$:

$$\mathbb{I} = C_{TE12}\begin{cases} \cos\left(\frac{h_1 d_1}{2}+\psi_1\right)\cos\left(\frac{h_2 d_2}{2}+\psi_2\right)\exp\left(\frac{p_1}{2}\left(d_1-d_2\right)\right) & x>\frac{d_2}{2} \\ \cos\left(\dfrac{h_1 d_1}{2}+\psi_1\right)\cdot & \\ \left[\left(\dfrac{p_1\cos\left(\frac{h_2 d_1}{2}+\psi_2\right)-h_2\sin\left(\frac{h_2 d_1}{2}+\psi_2\right)}{{p_1}^2+{h_2}^2}\right)\right. & \\ -\exp\left(\dfrac{p_1}{2}\left(d_1-d_2\right)\right)\cdot & x>\frac{d_1}{2} \\ \left.\left(\dfrac{p_1\cos\left(\frac{h_2 d_2}{2}+\psi_2\right)-h_2\sin\left(\frac{h_2 d_2}{2}+\psi_2\right)}{{p_1}^2+{h_2}^2}\right)\right] & \\ \frac{\sin((h_1+h_2)d_1)\cos(2(\psi_1+\psi_2))}{h_1+h_2}+\frac{\sin((h_1-h_2)d_1)\cos(2(\psi_1+\psi_2))}{h_1-h_2} & -\frac{d_1}{2}<x<\frac{d_1}{2} \\ \cos\left(\dfrac{h_1 d_1}{2}-\psi_1\right)\cdot & \\ \left[-\left(\dfrac{-q_1\cos\left(\frac{h_2 d_1}{2}-\psi_2\right)+h_2\sin\left(\frac{h_2 d_1}{2}-\psi_2\right)}{{q_1}^2+{h_2}^2}\right)\right. & \\ +\exp\left(\dfrac{q_1}{2}\left(d_1-d_2\right)\right)\cdot & x<-\frac{d_1}{2} \\ \left.\left(\dfrac{-q_1\cos\left(\frac{h_2 d_2}{2}-\psi_2\right)+h_2\sin\left(\frac{h_2 d_2}{2}-\psi_2\right)}{{q_1}^2+{h_2}^2}\right)\right] & \\ \cos\left(\frac{h_1 d_1}{2}-\psi_1\right)\cos\left(\frac{h_2 d_2}{2}-\psi_2\right)\exp\left(\frac{q_1}{2}\left(d_1-d_2\right)\right) & x<-\frac{d_2}{2} \end{cases} \tag{2.18}$$

The core region $-\frac{d_1}{2}<x<\frac{d_1}{2}$ of the narrowest waveguide contains the highest magnitudes of the fields, and so might be the most crucial component to look at setting to a constant. While this leads to a tidy equation it is found that the decaying field components of the overlap are not negligble and contribute crucially to attaining a constant value. Thus an analytical solution to a taper shape providing a constant mode overlap along its length is unattainable.

Instead, a constant overlap taper can be constructed by starting with a given taper width and numerically solving Eq. 2.18 equal to a constant for the next width. Of course as the solution has to be provided numerically anyway now, Eq. 2.18 could be bypassed and the overlap integral, Eq. 2.17, could be solved for all combinations of $\mathcal{E}(d)$, noting that the overlap integral is symmetric so that the overlap between modes $\mathcal{E}_i$ and $\mathcal{E}_j$ is equal to the overlap of $\mathcal{E}_j$ and $\mathcal{E}_i$. Such an array of overlaps was shown in Figure 2.4, on which a constant overlap taper

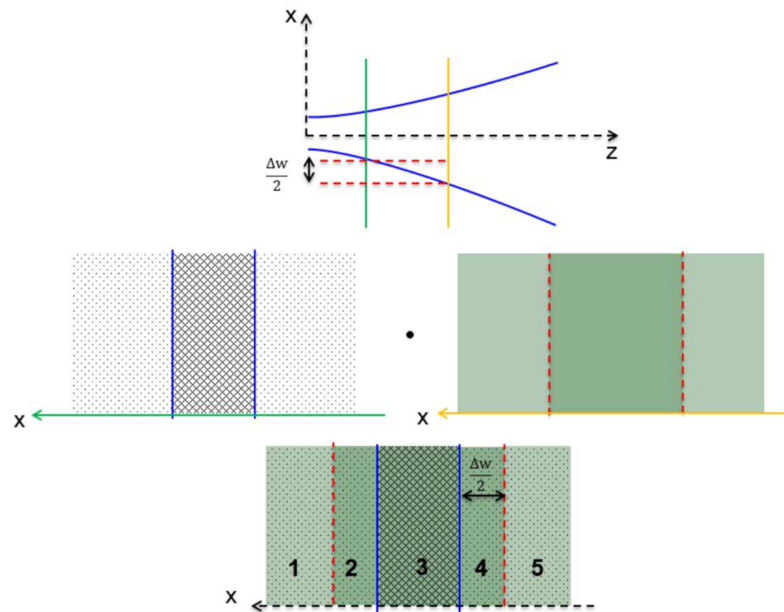

Figure 2.5: The 5 regions for the evaluation of the overlap integral between taper slices with core widths differing by ΔW. The core and cladding regions overlap at different places.

follows a contour.

2.1.4 Comparison of Taper Shapes

The shape of a constant overlap taper is displayed in Figure 2.6. It can be seen that the taper shape is exponential-like in shape and is convex. It also indicates that the taper shape is not dissimilar to simpler exponential and parabolic geometries. Further, the length is normalised in Figure 2.6 which emphasises the difference between the taper shapes. If a realistic distance of tens of micrometers was instead plotted then the difference between the tapers would become negligible and they would become indiscernible. Still it remained to be seen whether the small difference in dimension would noticeably affect propagation, even with a width difference less than the propagating wavelength.

In combination with the taper shapes in Figure 2.6 the overlap along the length of each taper can be examined, displayed in Figure 2.7 for a widening taper. The constant overlap taper is correctly constant along its propagation direction, and is chosen to have an overlap of 0.9999, as close to unity as achievable without excessive computation time, only a uniform waveguide would achieve a complete overlap. Both the exponential and parabolic tapers start with a high overlap which decreases overall. With reference to the overlap surface of Figure 2.4 the reason for the decrease in modal overlap can be intuited. The exponential and

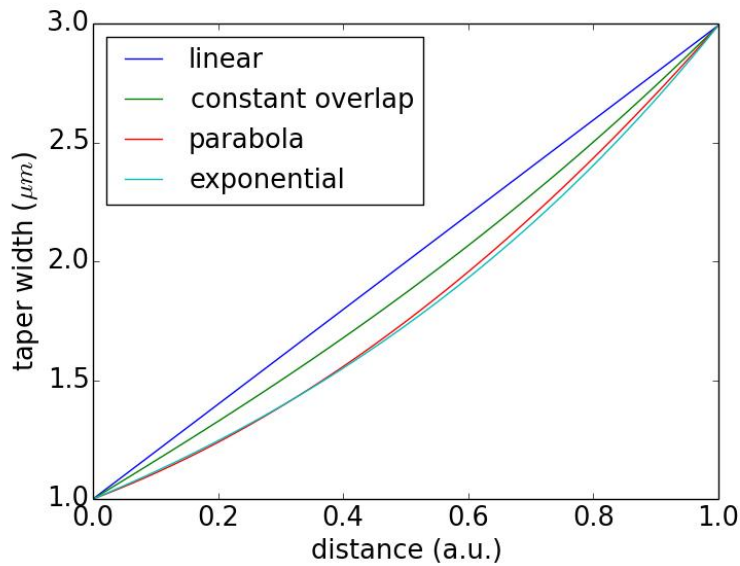

Figure 2.6: The shape of linear, exponential and parabolic tapers and the shape of a taper with constant modal overlap along its length.

parabolic shapes increase in width the slowest and remain in the narrow region where a small change in waveguide width results in a large change in the mode and with it a drop in the mode overlap. The linear taper's overlap integral, however, increases as the taper widens. This can be seen in Figure 2.4 as the linear taper quickly departs the narrow region and enters the wide waveguide width region which then maintains a higher overlap with changing width.

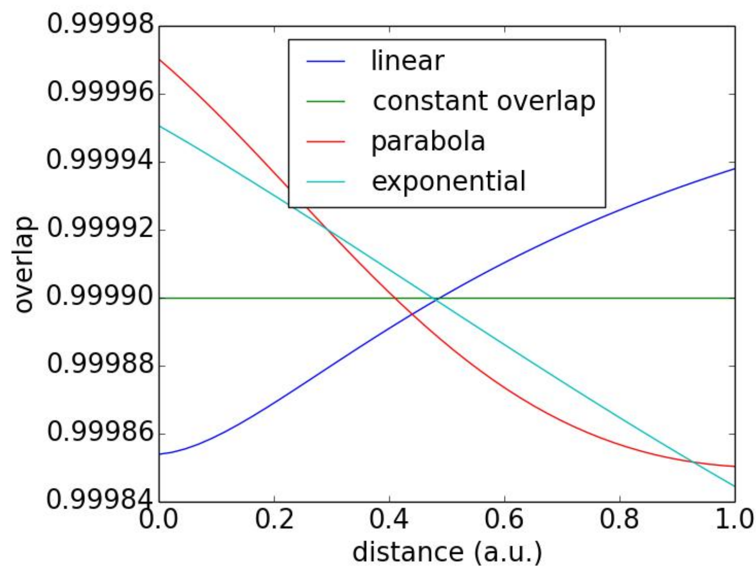

Figure 2.7: The overlap integral along the length of widening linear, exponential, parabolic and constant overlap tapers.

2.1.5 Beam Propagation Method

To investigate light propagation in photonic devices the beam propagation method (BPM) [192] is used. The beam propagation method looks at the Helmholtz equation, Eq. 2.10, varying in all three dimensions so that the electric field is written as

$$\mathbf{E} = u\left(x, y, z\right) e^{i(\beta z - \omega t)} \tag{2.19}$$

consisting of a slowly varying component $u(x, y, z)$ and quickly varying z-dependent exponential terms. The most rapid change to the electric field is most typically due to the phase change with propagation along the guiding axis z. The electric field expression is thus similar to Eq. 2.9 for the slab waveguide case, but the mode u, previously termed $\mathcal{E}$ for the slab, is now z-dependent also. The Helmholtz equation, Eq. 2.10, thus becomes

$$\nabla^2 u + 2i\beta \frac{\partial u}{\partial z} + \left(k^2 - \beta^2\right) u = 0 \tag{2.20}$$

As $u\left(x, y, z\right)$ varies slowly with z it is taken that $\frac{\partial^2 u}{\partial z^2} \to 0$ in what is called the paraxial approximation or parabolic approximation. The resulting beam propagation equation becomes

$$\frac{\partial u}{\partial z} = \frac{i}{2\beta}\left(\frac{\partial^2 u}{\partial x^2} + \frac{\partial^2 u}{\partial y^2} + \left(k^2 - \beta^2\right) u\right) = 0 \tag{2.21}$$

The beam propagation software used was BeamPROP [192]. This solves the beam propagation equation numerically using the finite difference method, taking a slice in z and describing it with discrete points in x and y to find the data for a subsequent slice. BeamPROP employs the transparent boundary condition which assumes that at the boundary there is an outgoing plane wave.

The launch field can be solved for using BPM, making the simulation method self-contained. Mode solving requires a z-invariant geometry and launching a sample field, usually a Gaussian, along it. BeamPROP calculates the mode from one of two options, the imaginary distance method or the correlation method. In the imaginary distance method iz from equation (2.19) is replaced by z'. By writing the field as a sum of all the modes, with amplitude c_m for mode m, it's seen that

$$E = \sum c_m u_m(x, y, z) e^{-i\omega t} e^{\beta_m z'} \tag{2.22}$$

so that at large z', large z, the largest β_m dominates. The largest β_m belongs to the fundamental mode $m = 0$, providing the solution.

The correlation method also uses E as expressed by Equation (2.22) and takes the Fourier Transform to see peaks at values β_m.

In order to ensure that the BPM results are correct, convergence studies can be performed on the simulations. The grid spacing in all directions can be reduced until the simulated output reaches a constant value. This allows the largest grid size possible to be used so that the computation time is reduced while maintaining accuracy.

2.1.6 Optimum Taper Shape

The Beam Propagation Method (BPM), outlined in the preceding Section 2.1.5, was used to determine which taper shape was capable of supplying the highest power transmission over the shortest distance. While BPM utilises the paraxial approximation which is not suitable for quickly changing geometries, the taper width change in the present simulations were still satisfactorily slow, as can be verified by convergence analysis of simulations. There are no bifurcations within the results as the width decreases in the range under investigation.

The constant overlap taper shape derived in Section 2.1.3, was drawn in 2D CAD within the BPM software. The launch mode for the initial width is calculated by first launching a Gaussian into a waveguide with a constant width equal to the initial width. The field propagates along the taper until the mode at one distance and the next matches. Similarly the ideal final mode of the taper can be calculated by setting the constant width equal to the end width. Alternatively the modes could be computed using Eqs. 2.12 and then inserted into BPM software. The launch mode is propagated along each individual taper, and at each step in the propagation the mode field is integrated over to compute the total power as well as the power within the boundaries of the taper itself. Additionally the overlap between the launch mode and the propagating mode is computed at each point, as well as the overlap with the ideal end mode.

If the taper was perfect then the mode would have a complete overlap with the ideal end mode, signifying a complete transition. This overlap is the best measurement of taper performance. In reality there will never be an overlap of unity but the aim is to get as close as possible. Figure 2.8 shows the BPM solution's overlap with the ideal end mode for different taper shapes. The linear taper outperforms the constant overlap taper, as well as the exponential and parabolic shapes. As discussed in Section 2.1.4 in relation to Figure 2.4, this indicates that a taper shape that avoids the narrow width region, where there is high change in overlap with a change in width, should be avoided as the linear

taper does but which the exponential and parabolic do not. For that reason the constant overlap taper also outperforms the exponential and parabolic shapes. Also included in Figure 2.8 then is an inverted parabola shape, with a negative slope that increases in magnitude as it narrows. The inverted parabola taper shape outperforms all the other tapers, supporting the result that the narrow width region should be resided in for as little as possible.

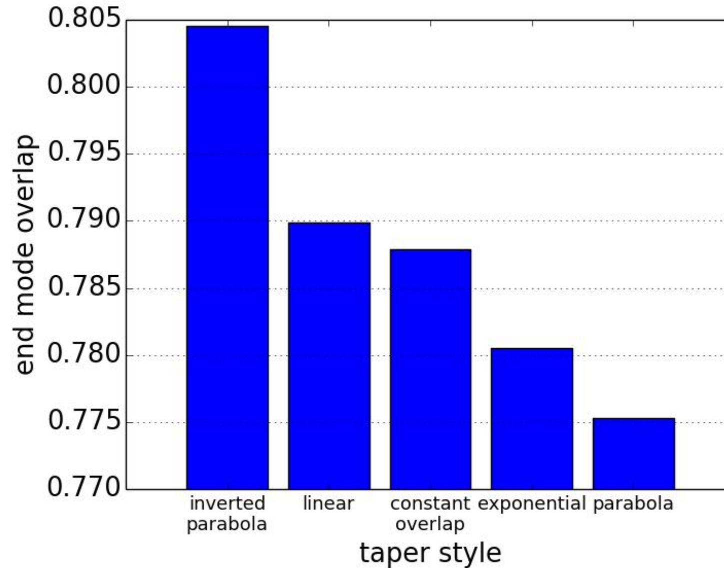

Figure 2.8: The overlap between a BPM simulation of the propagating mode and the ideal mode at the end of a taper.

The result that the narrow region should be exited quickly indicates that the slope of the taper shapes was backwards. It was intuitively presumed that it would be best to change width slowly in the region of high loss, the narrow width region, but this is not the case. The reason for the presumption was to vary the taper slowly to maintain a high overlap. However, in the overlap surface of Figure 2.4 a same sized change in width has a higher overlap in the wide waveguide region than the narrow. This explains why the linear outperforms the others, because it remains in the wide region for longer. This analysis suggests that an ideal taper would have the opposite slope to those used above in Figure 2.6, and would instead remain at wide waveguide widths longer than even the linear taper. Figure 2.8 includes one such taper design, parabolic but with the slope reversed from the previously examined one, which indeed has the highest overlap with the taper end mode and so has the most effective taper transition.

As mentioned previously at the latter stages of Section 2.1.4, the physical difference in taper shapes is already minimal for realistic dimensions. Furthermore, the transmission results shown in Figure 2.8 are all within 4% of each other, which

may be considered an acceptable range. A linear taper is the easiest to design and fabricate on a lithographic mask, and as the shape and transmission between tapers is nominally the same, can be determined as the best choice for a taper.

2.2 Tapers for Vertical Transitions

The previous analysis was performed for a single waveguide, which would be grown and fabricated as a single semiconductor junction. As outlined in Chapter 1.3 this work vertically integrates two waveguides by epitaxially growing them above each other during the same growth sequence.

A passive waveguide is integrated above an active waveguide, where the passive waveguide is destined to become an MZM and the active waveguide is a laser. The laser material was adapted from commercially available InP-AlGaInAs 1.55μm wavelength emitting material [193], which has 5 QWs for optimised gain and confinement. The MZM material is adapted from previous projects undertaken by the Integrated Photonics Group at the Tyndall National Institute. The MZM material consists of 26 QWs for optimised index change with modulating voltage.

The vertically stacked material is shown in Table 2.1 with each epitaxial layer's refractive index. At the base of the structure there is of course the InP wafer, above which additional InP cladding layers are grown. The laser layers with SCH layers surrounding 5 QWs come next at the bottom, followed by more InP cladding. This would complete a solely active structure. For this work's vertical integration, the passive material is then placed upon the cladding InP above the laser. The passive material can be seen to consist only of a single core layer between SCH layers in Table 2.1, rather than the optimum 26 QWs. The layer number was reduced to simplify simulations, with the average refractive index of the QWs taken and applied to the single layer. Finally, the structure is capped with more InP cladding.

2.2.1 Monolithic Vertical Integration Design

For two stacked waveguides there are multiple options in how to couple light between them. Regrowth-free monolithic integration is the technique of choice because it utilises a single epitaxial growth sequence, removing regrowth and selective area growth steps, which have been outlined as undesirable in Chapter 1 due to expense, difficulty, reproducibility and yield [54, 98, 103, 118, 132, 137, 160–162] Thus, within a monolithic platform there can be no vertical variation

Table 2.1: The epitaxial design of the up-down structure, with the refractive indices used in simulations.

Layer #	**Layer**	**Material**	**Refractive index**	**Thickness nm**
17	Cladding	InP	3.1673	1000
16	SCH	AlGaInAs	3.28384	250
15	Core	AlGaInAs	3.427865	447
14	SCH	AlGaInAs	3.28384	50
13	Cladding	InP	3.1673	1000
12	SCH	AlGaInAs	3.2347	10
11	SCH	AlGaInAs	3.22444	60
10	SCH	AlGaInAs	3.2725	60
9 ($\times$5)	Barrier	AlGaInAs	3.36103	10
8 ($\times$5)	Well	AlGaInAs	3.44344	6
7	Barrier	AlGaInAs	3.36103	10
6	SCH	AlGaInAs	3.2725	60
5	SCH	AlGaInAs	3.22444	60
4	Cladding	InP	3.1673	160
3	Cladding	InP	3.1673	340
2	Cladding	InP	3.1673	1000
1	Wafer	InP	3.1673	

in the structure; there can be no vertical tapers. This leaves lateral tapers as the only choice, operating in the plane of the waveguides and altering the waveguide widths as previously examined in Section 2.1.

Figure 2.9 shows the effective index of waveguides at different upper ridge widths. As the ridge width of a waveguide decreases the effective index drops. Once the ridge is wide enough the mode in the waveguide views the ridge as being a slab extending away to infinity and adopts an index close to that of the core alone.

The waveguides must have effective indexes greater than the InP cladding, which has an index of 3.167 in the models, in order to support a mode, following Eq. 2.12.

When the effective indices of the stacked waveguides become comparable light begins to couple between them. The reasoning can be seen from earlier Section 2.1.1 where it was discussed that light will be predominantly guided by the waveguide with the highest refractive index. When the indices of two waveguides are the same then the mode will be split across the waveguides, and once the lower waveguide's index becomes largest it dominates the waveguiding. Section 2.2.2 will further probe coupling between the stacked waveguides.

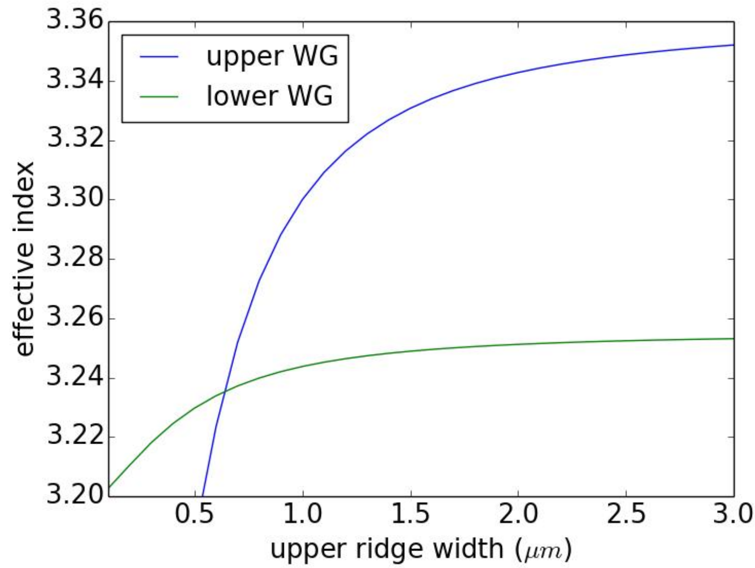

Figure 2.9: The effective index of the two waveguides at different upper ridge widths.

2.2.2 Coupled Waveguide Analysis

A linear taper was found to be the optimum taper shape for waveguides on one plane, balancing ease of fabrication with high optical transmission, Section 2.1.6. This work focuses further on vertical integration, adding a dimension for waveguiding. The additional vertically stacked waveguides complicate the device geometry and it becomes easier to use purely numerical mode solutions and BPM simulations.

However the 2D analysis of preceding sections can still be used to gain initial insight and inform important characteristics just as well as a full 3D model. Each of the stacked waveguides can be solved for separately using the effective index method, Section 2.1.1. When the overall effective index of each waveguide has been found then those values can be used in coupled waveguide equations.

For two waveguides coupling together, each mode will solve the Helmholtz equation in their respective waveguide. The mode solution containing both waveguide modes we can denote as [91]

$$\mathcal{E} = \sum_{m} A_m(z)\, \mathcal{E}_m(x, z) \tag{2.23}$$

for m the mode in each waveguide a and b, and where $A_m(z)$ is the contribution to the amplitude at position z from mode m. $\mathcal{E}_m$ has the same form as Eq. 2.9.

We can place the total mode solution into the Helmholtz equation, Eq. 2.5,

$$\sum_m A_m \left(\nabla^2 \mathcal{E}_m + k^2 \mathcal{E}_m\right) + 2\frac{dA_m}{dz}\frac{\partial \mathcal{E}_m}{\partial z} + \frac{\partial^2 A_m}{\partial z^2}\mathcal{E}_m = 0 \tag{2.24}$$

This can be simplified by assuming that the amplitude does not vary very quickly with propagation along z, same as the paraxial approximation in BPM in Section 2.1.5, so that $\frac{\partial^2 A_m}{\partial z^2} \to 0$. We also have from the electric field, Eq. 2.9, that $\frac{\partial \mathcal{E}_m}{\partial z} = i\beta_m \mathcal{E}_m$.

Each waveguide on its own has a permittivity $\epsilon_m(x)$ that varies in x. When a second waveguide is added along x the waveguides experience a perturbation to their permittivity $\Delta\epsilon_m(x)$ from the added waveguide. We can place this into our equation in place of k; $k^2 = k_0^2 n_m^2 = k_0^2(\epsilon_m + \Delta\epsilon_m)$. The Helmholtz equation for the two waveguides becomes

$$\sum_m A_m \left(\nabla^2 \mathcal{E}_m + k_0^2 \epsilon_m \mathcal{E}_m\right) + A_m k_0^2 \Delta\epsilon_m \mathcal{E}_m + 2i\beta_m \frac{dA_m}{dz}\mathcal{E}_m = 0 \tag{2.25}$$

and $\nabla^2 \mathcal{E}_m + k_0^2 \epsilon_m \mathcal{E}_m = 0$ as the individual Helmholtz equation for each waveguide alone. To find the coupling of waveguide a we multiply across by $\langle \mathcal{E}_a|$, or similarly for b, so the wave equation becomes

$$2i\beta_a \frac{dA_a}{dz}\langle \mathcal{E}_a|\mathcal{E}_a\rangle + 2i\beta_b \frac{dA_b}{dz}\langle \mathcal{E}_a|\mathcal{E}_b\rangle = -A_a k_0^2 \langle \mathcal{E}_a|\Delta\epsilon_a|\mathcal{E}_a\rangle - A_b k_0^2 \langle \mathcal{E}_a|\Delta\epsilon_b|\mathcal{E}_b\rangle \tag{2.26}$$

Further approximations are used to simplify the above equation. The overlap between a waveguide and itself is taken to be considerably larger than with the other waveguide, so that $\langle \mathcal{E}_a|\mathcal{E}_b\rangle \to 0$. Similarly the overlap of a waveguide's mode into the added external permittivity perturbation is small, so that $\langle \mathcal{E}_a|\Delta\epsilon_a|\mathcal{E}_a\rangle \to 0$. Finally, by examining the form of the electric field, Eq. 2.9, there is an oscillatory difference between the waveguide fields coming from their propagation constants, so we will explicitly write $\langle \mathcal{E}_a|\mathcal{E}_b\rangle \to \langle \mathcal{E}_a|\mathcal{E}_b\rangle e^{i\Delta\beta z}$ where $\Delta\beta = \beta_b - \beta_a$. The same holds for waveguide b. The resulting expressions for the change in the amplitudes of waveguides a and b is

$$\begin{aligned} \frac{dA_a}{dz} &= i\kappa_a A_b e^{i\Delta\beta z} \\ \frac{dA_b}{dz} &= i\kappa_b A_a e^{-i\Delta\beta z} \\ \kappa_m &= \frac{k_0^2}{2\beta_m}\frac{\langle \mathcal{E}_m|\Delta\epsilon_n|\mathcal{E}_n\rangle}{\langle \mathcal{E}_m|\mathcal{E}_m\rangle}, n \neq m \end{aligned} \tag{2.27}$$

The above coupled equations, Eq. 2.27, can be solved by taking a further derivative with respect to z, which allows removal of the other waveguide's amplitude contribution and results in a characteristic equation. For example for waveguide a

$$\begin{aligned} \frac{d^2A_a}{dz^2} &= i\kappa_a \frac{dA_b}{dz} e^{i\Delta\beta z} + i\kappa_a A_b i\Delta\beta e^{i\Delta\beta z} \\ \Rightarrow \frac{d^2A_a}{dz^2} &- i\Delta\beta \frac{dA_a}{dz} + \kappa_a\kappa_b A_a = 0 \end{aligned} \tag{2.28}$$

which can be solved through the ansatz $A_a(z) = A_a e^{pz}$ to find

$$\begin{aligned} A_a(z) &= A_{a0} e^{i(\Delta+\beta_c)z} + A_{a1} e^{i(\Delta-\beta_c)z} \\ \Delta &= \frac{\Delta\beta}{2}, \beta_c^2 = \Delta^2 + \kappa_a\kappa_b \end{aligned} \tag{2.29}$$

and A_b can then be found using Eq. 2.27,

$$A_b(z) = \frac{\Delta+\beta_c}{\kappa_a} A_{a0} e^{i(\Delta+\beta_c)z} + \frac{\Delta-\beta_c}{\kappa_a} A_{a1} e^{i(\Delta-\beta_c)z} \tag{2.30}$$

Boundary conditions are then needed to determine the values of the amplitudes. In the case of a directional coupler, power starts fully in one guide only. This is the same case as in this work, light will be in either the passive or active waveguide completely, and then a transition will be instigated. Thus $A_a(0) = 1$ and $A_b(0) = 0$. Once the constants are solved for we arrive at

$$\begin{aligned} A_a(z) &= e^{i\frac{\Delta\beta}{2}z} \left(\cos(\beta_c z) - \frac{i\Delta}{\beta_c} \sin(\beta_c z) \right) \\ A_b(z) &= e^{-i\frac{\Delta\beta}{2}z} \frac{i\kappa_b}{\beta_c} \sin(\beta_c z)) \end{aligned} \tag{2.31}$$

Above are the amplitude fields for the waveguide modes, but it is typically the power that is measured, and the power P goes as the square of the amplitude A. The power along z for the waveguides is then

$$\begin{aligned} \frac{P_A(z)}{P_0(z)} &= 1 - \frac{\kappa_a\kappa_b}{\beta_c^2} \sin^2(\beta_c z) \\ \frac{P_B(z)}{P_0(z)} &= \frac{\kappa_b^2}{\beta_c^2} \sin^2(\beta_c z) \end{aligned} \tag{2.32}$$

For the case of identical guides brought together, then the coupling coefficients $\kappa_a = \kappa_b = \kappa$ are the same and there is no difference in propagation constants,

resulting simply into

$$\begin{aligned} \frac{P_A(z)}{P_0(z)} &= \cos^2(\kappa z) \\ \frac{P_B(z)}{P_0(z)} &= \sin^2(\kappa z) \end{aligned} \tag{2.33}$$

It can be seen from this that the power transfer between the guides is complete, 100%, when the guides are the same. Referencing the non-identical case of Eq. 2.32 it can be seen that the additional factors result in a less than complete power transfer. The power is $\frac{\pi}{2}$ out of phase in each of the identical waveguides, so that power transfer from one to the other is complete after a length $L = \frac{\pi}{2\kappa}$. When the waveguides are different, as in Eq. 2.32 the power transfer is completed after a length $L = \frac{\pi}{2\beta_c}$ and this is termed the transfer length. In order to maximise the transfer the waveguides should be made as identical to each other as possible, and this is achieved by lateral tapers as previously outlined.

The coupling coefficients κ between the guides depend on the overlap between the modes in the guides, Eq. 2.27. If the waveguides are far away then the modal overlap will be minimal, leading to low coupling κ, and so the transfer power will be small, resulting in very little coupling and power transfer, as makes sense intuitively.

The coupling coefficients κ can be calculated in much the same way as the overlap integral, Eq. 2.17, integrating the overlap of the mode within one of the cores. Figure 2.10 shows the coupling coefficients between upper-to-lower and lower-to-upper waveguides at different upper waveguide widths.

The lower waveguide's coupling to the upper waveguide decreases as the upper width increases. This happens because the propagation constant increases with increasing width, Figure 2.9, so that the mode becomes more confined within the upper waveguide core, as previously discussed with reference to Eqs. 2.12 and 2.13. As a result the mode no longer reaches as far into the core of the perturbing lower waveguide, and thus the coupling is reduced. On the other hand the increase in upper waveguide width also increases the permittivity perturbation that the lower waveguide experiences, and thus the coupling from upper to lower is increased.

The fraction of power coupled from the upper to lower waveguide is shown in Figure 2.11. The coupling fraction is taken as $\frac{\kappa_a \kappa_b}{\beta_c^2}$ from Eq. 2.32. From the coupling fraction it can be seen that the power transfer is maximised at an upper waveguide ridgewidth of approximately $0.7\mu m$. This is the point where the coupling coefficients of Figure 2.10 intersect. The maximum transfer occurs

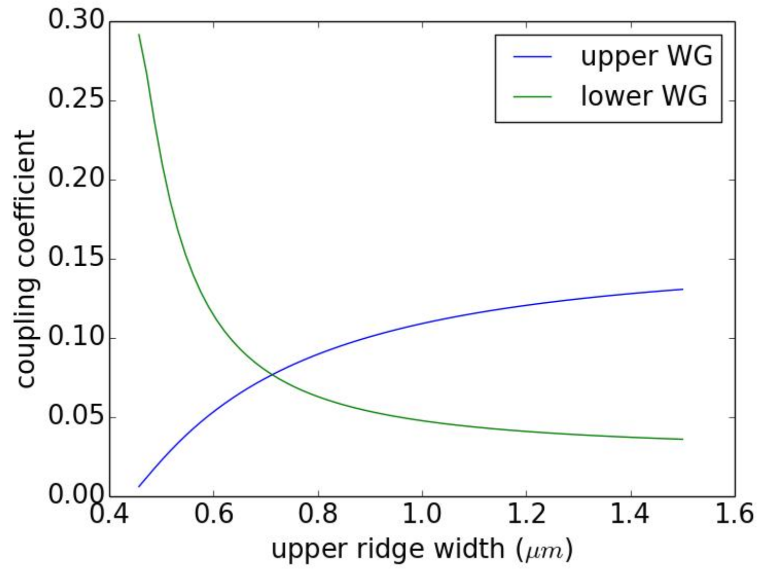

Figure 2.10: Coupling coefficients between the upper and lower waveguides as the upper waveguide width changes.

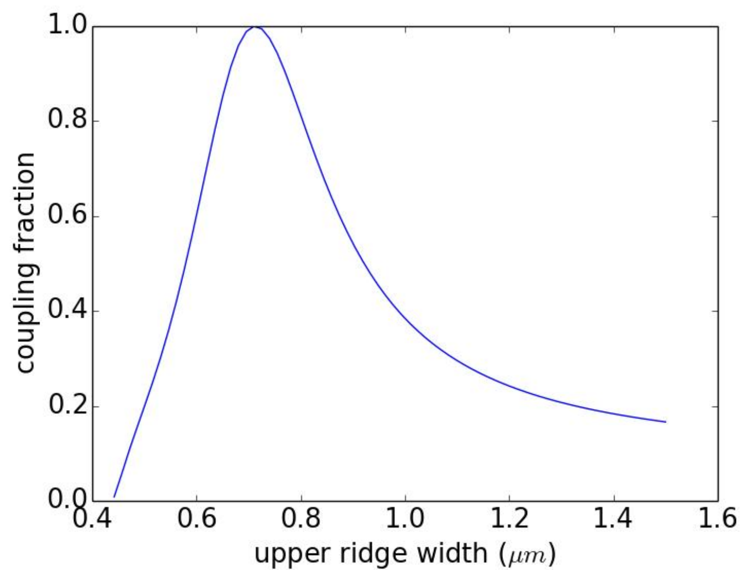

Figure 2.11: Coupling fraction between the upper and lower waveguides as the upper waveguide width changes.

when the guides are the same.

As the behaviour of the coupling coefficients are different depending on the coupling direction, it then makes sense that the mode will transfer differently depending on if it is an up-down or down-up transition. The coupling fraction increases more steeply as the upper waveguide is increased to the transition width of $0.7\mu m$ (the 0 fraction at $0.4\mu m$ arises because the upper mode is no longer supported at that width). This steep increase in power transfer implies that the down-up transition will occur more easily than the up-down transition that has a smaller slope.

The coupling coefficient analysis was displayed for only the upper waveguide width varying. Figure 2.9 showed the effective indexes of the upper and lower waveguides as a function of the upper ridge width. The lower waveguide effective index does not vary considerably as it is narrowed and thus has no effect on the behaviour of the upper ridge. Further the upper waveguide will be designed to be independent from the lower waveguide so that it cannot be affected by the lower waveguide's variation.

2.2.3 Modal Overlap Analysis

The overlap integral, Eq. 2.17, can be performed between various geometries, but it is logical to narrow down the variables to begin with.

Figure 2.12 illustrates the vertically stacked waveguides. Each waveguide is defined by a ridge etch, which will cause the mode to be supported and centred on each of the waveguide cores. To support the upper waveguide's ridge the bottommost waveguide must be wider. This naturally restricts the values of the lower waveguide's width.

Figure 2.13 displays a mode solution's preference to be centred on the waveguide with the higher refractive index.

To minimise fabrication steps, as will be further outlined in more detail in Chapter 3, a single deep etch through the upper waveguide can be used to remove one of the potential etches. This removes one variable from the structure.

The variables left in the device structure are the etch depth and width defining the upper ridge, and the etch depth and width defining the lower ridge. Figure 2.14 shows mode solutions for different upper ridge widths as the upper and lower etches are varied. In many cases the mode is not effectively supported and will result in radiation losses as the mode propagates along the structure.

Chiefly the etch depth and ridge width of the lower waveguide can first be selected to provide confinement only in the lower waveguide. Then the geometry

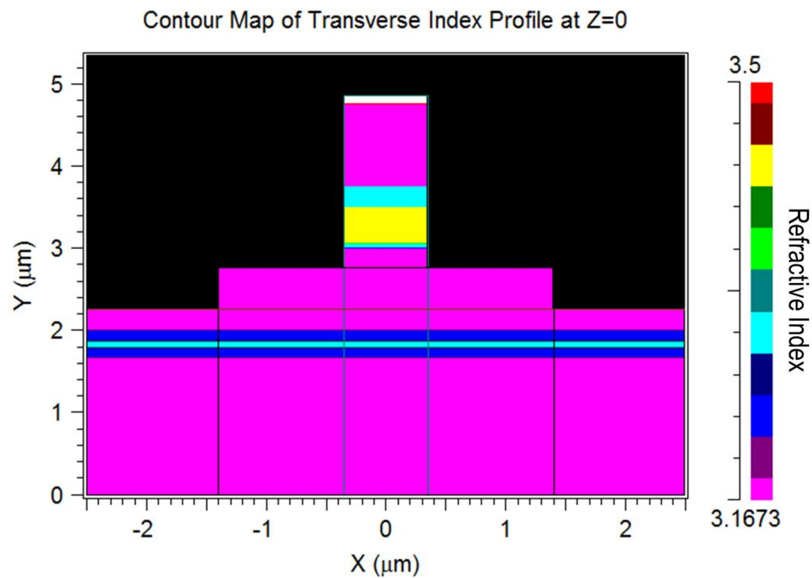

Figure 2.12: Illustration of two vertically stacked waveguides, displaying the refractive index profile. Each waveguide is defined by a ridge etch, thus requiring the bottom waveguide to be wider than the waveguide above to support it.

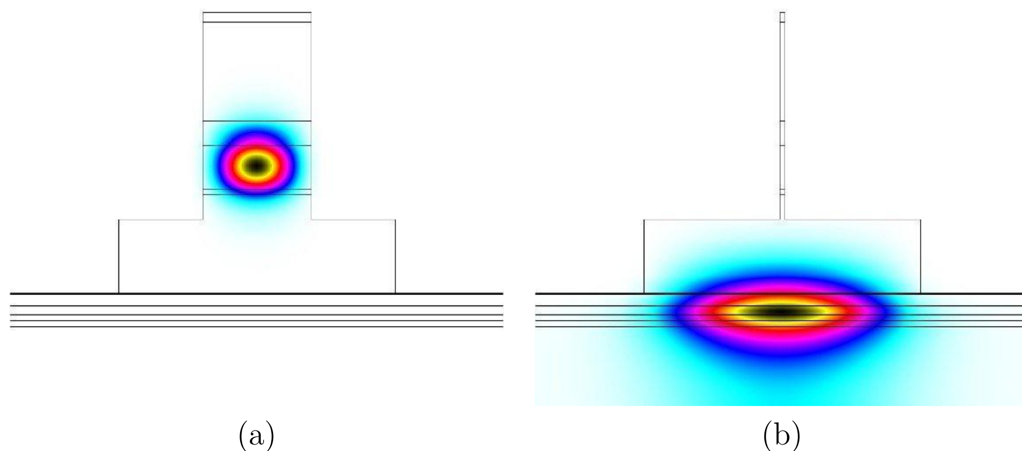

Figure 2.13: Two vertically stacked waveguides with different refractive indices. The mode solution is preferentially centred around the waveguide with the higher effective index. (a) The upper WG supports the mode, but (b) when the upper ridge is narrowed the lower WG supports the mode.

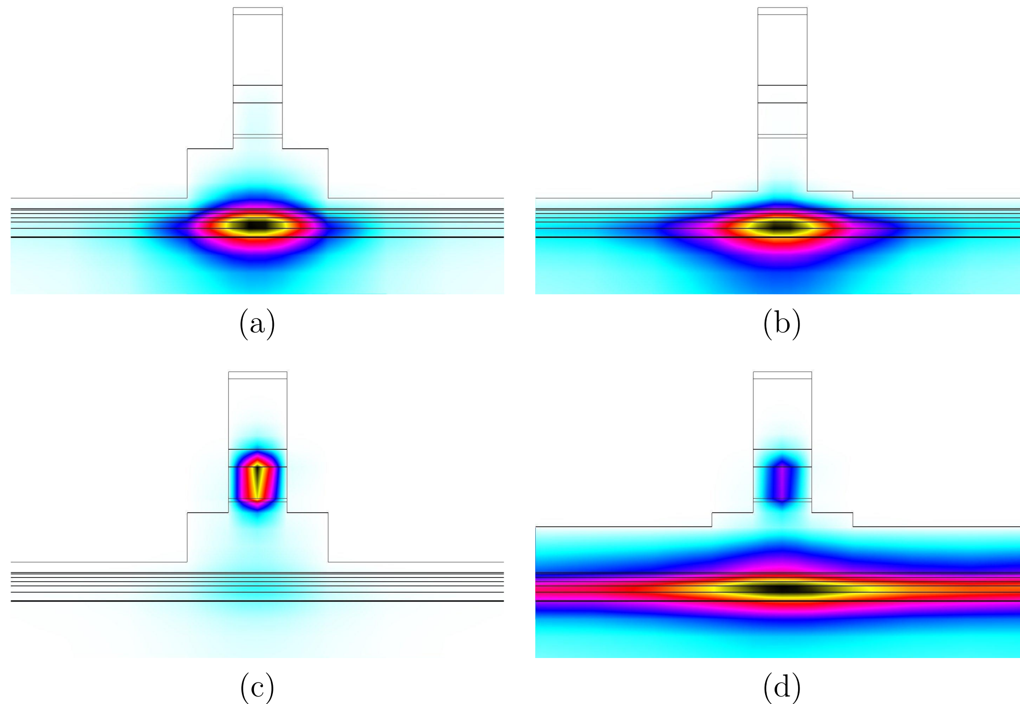

Figure 2.14: Mode solutions for different ridge widths and etch depths of the upper and lower WGs. For the lower WG supported the upper etch is varied in (a) and (b). For the upper WG originally supported the lower etch depth alters the mode shape in (c) and (d).

of the upper waveguide can be solved to find a well confined mode in the upper waveguide. If the etch depth resulting from the solution for the lower waveguide interferes with the upper waveguide then it can subsequently be altered to balance the mode solutions in each waveguide.

To achieve the isolation required for the monolithic vertical integration, there must not be any modal overlap of the upper passive into the lower active waveguide. The mode solutions indicate how much of the mode is in the lower waveguide. The mode can be integrated over the core of the lower waveguide to inform the amount that is present there. A functional restriction that only less than 1% of the mode is allowed to be in the lower waveguide ensures the passive mode solution will not be absorbed.

This modal analysis also indicates the width of the upper waveguide where the mode begins to be preferentially supported by the lower waveguide. As was shown in Figure 2.13, the mode will be centred on the waveguide with the highest effective index. As was shown in Figure 2.9 the effective index of a waveguide decreases as the ridge width narrows. Thus, as the upper waveguide is narrowed the mode will instead become centred on the lower waveguide that originally had a lower refractive index. The width at which this reversal in effective indexes

occurs is the transition region of interest for vertical coupling.

The 2D mode slices in the structure can be solved for different upper waveguide ridge widths. For the monolithic integration process these ridge widths dictate the coupling process. Each mode solution can be overlapped with another, using the overlap integral of Eq. 2.17 now purely computationally in 2D. The overlaps are again symmetric, and result in an overlap surface shown in Figure 2.15.

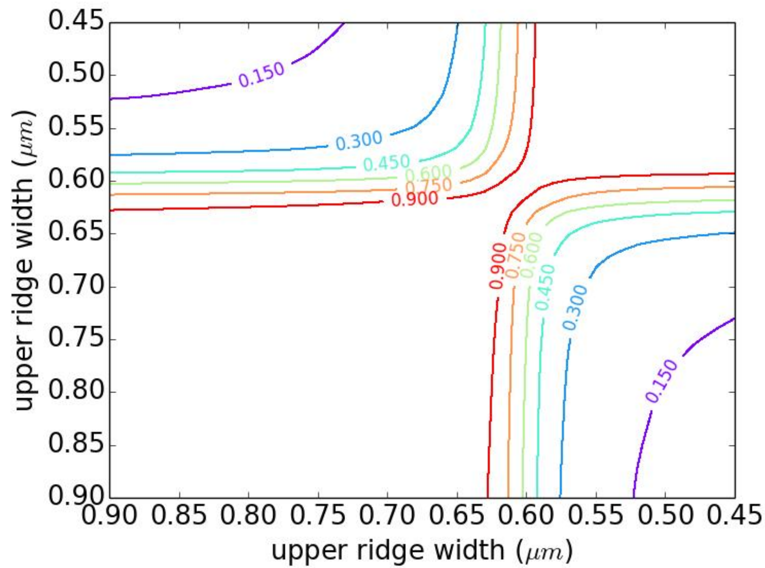

Figure 2.15: Modal overlaps between the mode solutions in the up-down WG structure for different upper WG ridge widths.

The 3D overlap surface can be compared to the 2D taper overlap surface of Figure 2.4. It can be seen that the characteristic behaviour remains, with wider upper ridge widths providing higher overlaps. Toward the narrow upper waveguide region the overlap increases again, and this is due to the mode spreading vertically across both waveguides at the transition point. At that point there is an increased overlap, but the modes are not supported in reality, they'd radiate away as losses.

A constant overlap taper follows a contour on the overlap surface, and thus the overlap surface can be used to determine the shape of a constant overlap taper. Figure 2.16 shows the resulting constant overlap taper shape, compared to a linear taper. The taper shape is similar to that obtained from 2D analysis, and is somewhat exponential in shape. It might be noted from the overlap surface of Figure 2.15 that because the overlap increases again during the transition then a constant overlap taper will begin to widen again. Thus a constant overlap

taper cannot actually be solved for through the vertical mode transition region, it ceases to narrow at an intermediate width.

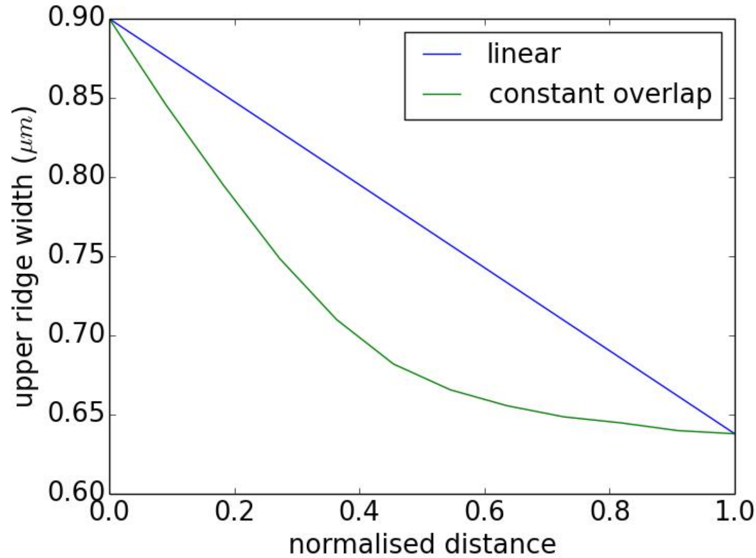

Figure 2.16: Comparison of taper shapes in the up-down WG structure, showing a linear taper and a taper with a constant overlap along its length.

The overlap is highest in the wide ridge section once again, and the 2D analysis found that the longer a waveguide remains in the wide region the lower the losses will be. Thus a constant overlap taper with the shape of Figure 2.16, or another similar positive curvature taper, that remains at low widths for longer will likely perform poorer than an equivalent linear taper. BPM simulations were nevertheless carried out to determine if this is indeed the case.

2.2.4 Beam Propagation Method Analysis

The full 3D structure of the up-down waveguide was drawn with CAD in BeamPROP. Initially the structure has a straight waveguide with a wide upper waveguide so that the mode is supported and centred on the upper waveguide. The upper waveguide is then tapered, using various shape functions, toward zero. The lower waveguide is then continued on straight.

Overlaps with the launch mode and end mode, the ideal lower waveguide mode, will indicate the success of the lateral taper vertical transition. For a full analysis the upper waveguide can then be tapered wider once more to its starting width, so that an overlap with the launch mode will indicate how efficient the overall up-down-up transition is.

Monitors can be placed over different regions of the device to integrate over the power propagating along that section. These monitors can be used as an alternative to the modal overlap comparison, and to determine the power in individual sections.

Placing a monitor into the lower waveguide core allows the overlap of the upper waveguide mode into the lower waveguide to be examined. The lower waveguide is active in the structure in reality and will absorb light that enters it. Thus for the upper waveguide to operate passively its mode solution cannot enter the lower active core.

The lower active waveguide can be set absorbing by setting its material to have a positive non-zero imaginary refractive index. With a BPM simulation, the launch mode can be solved in a straight upper waveguide and launched down the straight stacked waveguide structure, recording the transmitted power. The transmitted power will decrease if the upper waveguide mode overlaps the lower absorbing waveguide. The BPM simulations can be repeated for different barrier thicknesses until the transmission is unity. Figure 2.17 shows the transmission versus barrier thickness, which levels off after a barrier thickness of $1\mu m$. This barrier thickness matches the typical p-cladding thickness of InP based lasers, which have layers placed between the QW core and top contact metal to prevent the metal absorbing the mode [151]. Alternatively the active material can be set with a negative non-zero imaginary refractive index which would supply gain to the mode, simulating an SOA.

BPM simulations were carried out for different taper shapes and it was found that a linear taper performs efficiently, akin to previous 2D analysis shown in Figure 2.18, and is simple to define. Thus a linear taper will be used for the transition. A point to note now is that the linear taper was more effective at the lossy transition section. However a much faster changing taper can be used away from the transition where the overlaps are high. To minimise the overall length of the taper, a two section taper is used, which very quickly reduces the waveguide width to the transition region, utilising the high overlap of the wide ridge region, then slows at the region of interest where the losses will be higher. Thus the overall taper shape, starting from a nominal width of $2.5\mu m$ and going towards the transition point and zero, will have positive curvature. At the transition region however, it is linear to maximise transmission.

It is beneficial to look at the full monitor along the propagation as it will indicate when the propagation behaviour converges. If the taper length were to be too short, then the light would diffract through the structure rather than

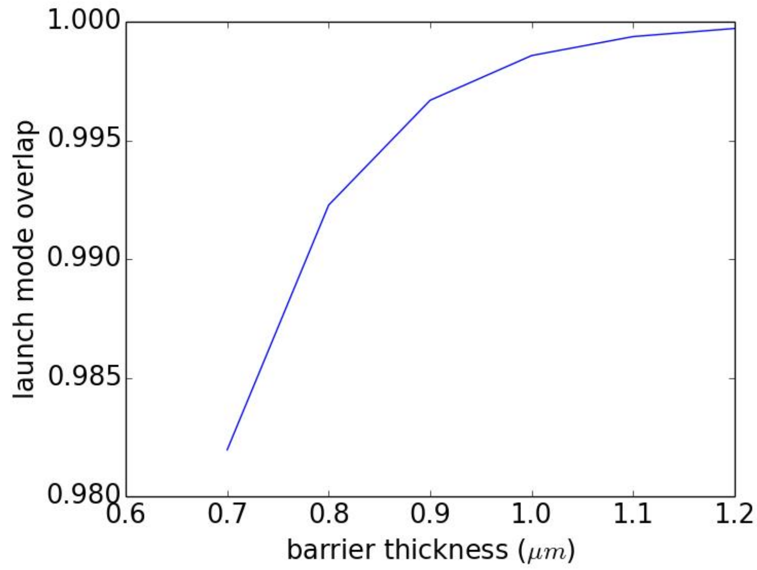

Figure 2.17: The final overlap with the launch mode for a mode propagating along the upper passive WG, with an absorbing lower active WG beneath separated by different barrier thicknesses.

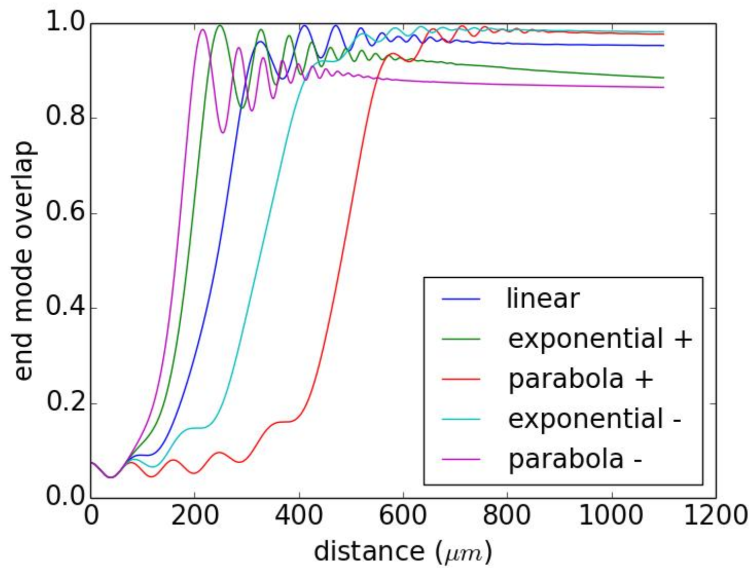

Figure 2.18: The overlap with the ideal end mode along an upward vertical transition in the up-down WG structure for different taper shapes. "+" and "-" indicate the curvature of the taper shape.

be guided correctly along it. This could possibly result in erroneous predictions of high power. Usually such a case would be recognizable as an outlying data point, but it may not be too dissimilar from other results and could instead be mistakenly included.

2.2.5 Taper Optimization Simulations

Both 2D and 3D analysis has indicated that the optimum taper shape is linear, being simple to draw and performing better than other options. Now the dimensions of the linear taper need to be optimised.

Just as with the taper shape analysis, BPM simulations can be carried out for different taper lengths. It is already known from mode solutions that the mode is supported in the upper waveguide at a ridge width of $2.5\mu m$ with a negligible overlap into the absorbing lower waveguide below. This ridge width can initially be set as the start of the upper waveguide taper.

There are two options for the taper transition. Either the taper can be tapered toward zero so that the mode completely leaves the upper waveguide, or the taper can reduce the upper waveguide's effective index to be the same as the lower waveguide at which point the mode will oscillate between the two waveguides. In the case where the mode departs the upper waveguide completely, termed an adiabatic taper, the upper waveguide need only be tapered beyond the width where it no longer supports the mode. The upper waveguide can then be left as a narrow ridge as it will have no impact on what is now the lower waveguide mode, or it can be etched away, which is beneficial practically because it allows top metal contact to the lower waveguide ridge. The drawback from this adiabatic taper is that its length is hundreds of micrometers long. A resonant coupler is the term for the other case, where the mode oscillates between the two waveguides. Its chief benefit is that it is shorter than the adiabatic taper. However, because the mode oscillates between the waveguides it does not experience the full gain from the lower waveguide. The mode will only experience gain while resident within the active core which will be half the time of its propagation. Further, the mode needs to be captured back in the upper waveguide at the end of the transition region. This means that the coupling length must be known and fabricated precisely. This fabrication tolerance is difficult owing to the small dimension of the coupling length, so that any error in fabrication, some of which is inevitable, will result in the mode not correctly transitioned to the guide of choice, resulting in loss of the mode power. Thus, in this work an adiabatic taper is chosen, as it allows greater fabrication tolerance, metal contact to the lower waveguide, and

isolated optimisation of the lower waveguide.

Initially the taper end width can be set to zero. In reality a zero end width isn't feasible, during processing the side walls of the ridge will cease to be defined cleanly at very low dimensions.

Figure 2.19 shows the overlap with the launch mode along the length of the up-down waveguide device. Due to the symmetry of the device along the propagation direction, the launch mode and the ideal end mode are identical. The overlap decreases at the taper transition as the mode enters the lower waveguide instead. The overlap then becomes zero in the straight solely lower waveguide section, proving that the mode has departed completely from the upper waveguide. The overlap increases once more as the upper waveguide is tapered wider again and the mode transitions vertically upward.

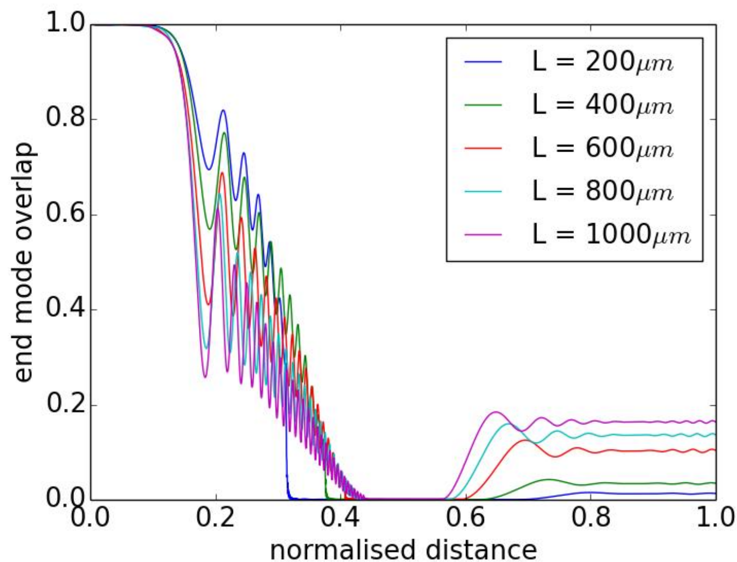

Figure 2.19: The overlap with the ideal end mode of the up-down WG device vs. distance for different taper lengths L. Due to the symmetry of the device the launch mode and end mode are equal.

There is a lot of power lost through the taper transitions, as seen from the overlap being less than 20% at the end of the propagation in Figure 2.19. This illustrates that vertically coupling the two waveguides as they are will not provide an efficient device. Alternate techniques will be explored in the next Section 2.3, but first the behaviour of the taper transitions are explored.

The transmission through the tapers increases as the taper length increases. The losses are reduced as the taper transition becomes slower and so more adiabatic. As mentioned earlier, the behaviour of the monitor also indicates when the taper length is suitable. As seen in Figure 2.19, the monitor takes a much differ-

ent path for the shortest tapers. By looking at the mode shape for short taper transitions it is seen that the mode is not properly guided along the taper between the guides, but rather it diffracts through the device unguided. Figure 2.20 shows the final transmitted power through the device for different taper lengths, indicating that the transmission will continue to increase with longer tapers.

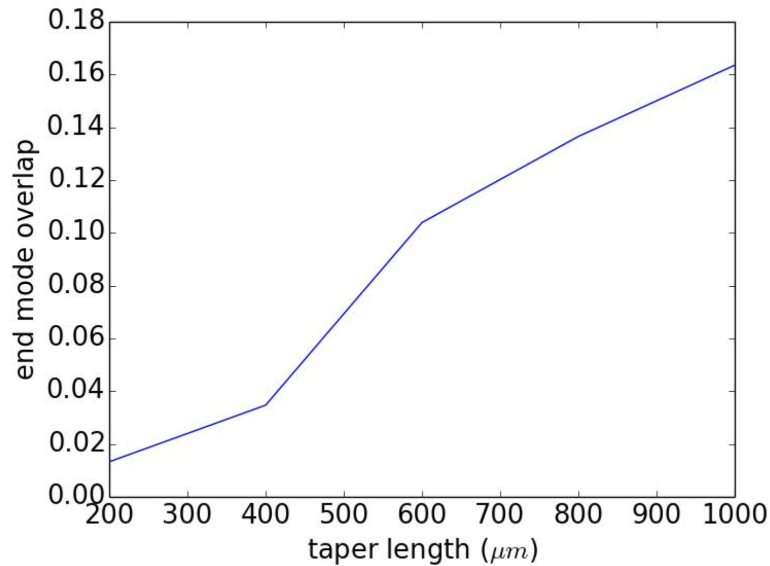

Figure 2.20: The overlap with the ideal end mode at the end of the transition in an up-down WG device for different taper lengths.

From BPM monitors, such as in Figure 2.19, it can be observed when the mode begins to transition. Using the monitors in the BPM software, the distance at which 1% of the field had departed the upper waveguide was noted. The corresponding ridge width the transition occurs at can be extracted from each taper's length. The resulting taper width is uniformly $0.7\mu m$. Thus in all future simulations the taper only needs to begin at $0.7\mu m$, reducing computation time and honing in on the area of interest.

This transition beginning width of $0.7\mu m$ matches that obtained from analytical results for coupled waveguides in Section 2.2.2, recommending the usefulness of that simpler analysis.

Mode slice solutions of cross sections of the structure show that the mode ceases to be solely supported within the upper waveguide once the upper ridge reaches a width of $0.4\mu m$. This width can be confirmed by the BPM simulations, Figure 2.19, extracting data the same way as when determining the taper transition beginning width. Thus BPM simulations can be run for a linear taper between $0.7\mu m$ and $0.4\mu m$ in the upper waveguide, for different lengths, that is for different taper slopes.

It can be found that the slope of the taper is the key parameter. If the start and end widths of the taper are altered, but the same slope is maintained, then the transmission will be the same. The BPM simulations show that the longer the taper the greater the transmission. This is intuitively expected, the slower the change in dimensions the more adiabatic the transition should be.

The above analysis presumed a symmetric device, so that the downward transition taper had the same dimensions as the upward transition taper. A symmetric device allows light to move in both directions equally, useful for initial tests which will form cavities using up-down-up waveguide combinations. For devices that are unidirectional, however, separate asymmetric upward and downward tapers could be used.

Optically it might be expected that the transition process is reversible. Nonetheless an upward taper was analysed just as the previous downward taper. Using BPM simulations it was found that the upward transition began when the upper waveguide width was $0.6\mu m$, rather than $0.4\mu m$ that the downward transition taper ends at. The transition is still completed once the upper waveguide reaches a width of $0.7\mu m$. This means that the taper slope has to be recalculated for the upward transition. To make a properly optimised taper symmetric device then the smallest taper slope between the upward and downward transition would have to be chosen to make sure that both transitions were complete. If the upward transition had the slowest taper change, then the length of the device would have had to become much larger as the downward taper needs to taper over a greater width range.

Section 2.2.2 outlined that the coupling coefficients are different for each waveguide, and this explains the fact that the taper transition is different when going from up-to-down or down-to-up, Figures 2.10 and 2.11. The upper waveguide is affected more as it is itself tapered, while the lower waveguide is less affected because less of its mode resides in the upper waveguide. If the process were to be reversible then the waveguides would have to be identical, and the lower waveguide would have to be tapered in turn. As it is, the process is inherently anti-symmetric vertically, though the structure looks symmetric laterally.

Figure 2.19 includes the power monitor along the propagation for an optimum up-down-up transition between the two vertically integrated waveguides. The maximum transmission is merely 20%. Such a low transmission isn't acceptable, as discretely packaged and externally coupled devices would achieve a higher coupling efficiency. If multiple up-down transitions were required within a device architecture then the losses would quickly become overwhelming. Thus a new

method of coupling the vertically stacked waveguides is required.

2.3 3 Waveguide Up-Down Coupling

The issue that can be uncovered from the two waveguide vertically coupling case of the preceding Section 2.2 is that the barrier region between the two waveguides, required to isolate the passive waveguide mode from an absorbing active waveguide beneath, is then too large to successfully transfer power across. It is perhaps not surprising that the isolation barrier works too well. The issue may be thought to arise from the similarity between the confinement factor in the purely passive section for an upper waveguide ridge width of typically $2.5\mu m$ and close to the transition region.

Additional options are needed to aid a modal transition across the large isolation distance of $1\mu m$. Grating couplers are usually used to increase the coupling between waveguides. A grating coupler introduces an additional wavevector arising from the introduction of a periodic structure. The grating serves to alter the effective index of a waveguide, as shown in Figure 2.21, changing the solutions from previous sections.

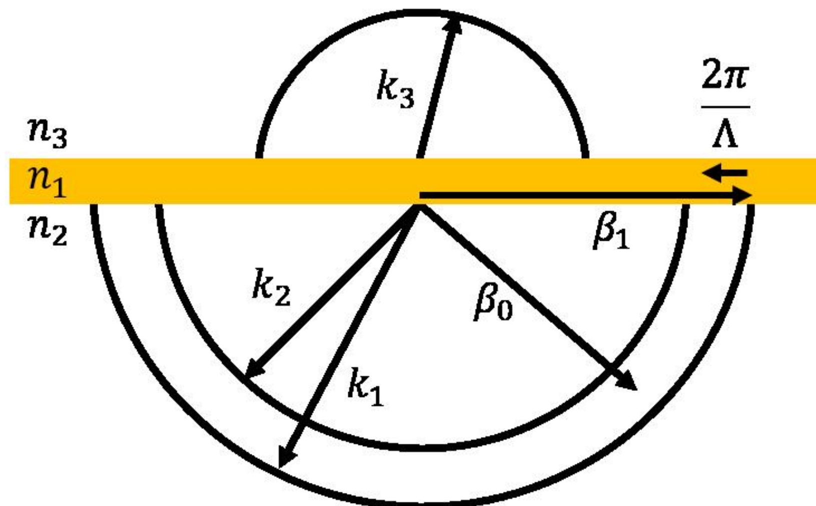

Figure 2.21: Diagram illustrating the possible solutions of a mode's propagation constants in a slab with core index n_1, substrate index n_2 and cladding index n_3. The mode will be supported if it has β_0 as indicated, between k_1 and k_2, the wavevectors in the core and substrate. If $\beta_0 < k_2$ then the mode will couple into the substrate and be lost. If $\beta_0 > k_1$ then the mode will couple into the substrate and air and be lost. A grating with a period Λ introduces a wavevector $\frac{2\pi}{\Lambda}$ that can reduce the propagation constant β_1, as illustrated, that is unsupported, to a supported value.

For monolithic integration, a grating can only be introduced as a permanent

corrugation to avoid any costly regrowth. The grating is defined by etches into the waveguide ridge. The periodic change in dimension of the ridge leads to a periodic perturbation in the permittivity. For a grating period Λ, $\Delta\epsilon$ becomes $\Delta\epsilon\left(z\right) = \Delta\epsilon_n e^{iq\frac{2\pi}{\Lambda}z}$ within our definition of the coupling coefficient in Eq. 2.27, $\langle\mathcal{E}_m|\Delta\epsilon_n|\mathcal{E}_n\rangle$ [91]. The coupling coefficient is then updated to

$$\kappa_m = \sum_q \kappa_m\left(q\right) e^{iq\frac{2\pi}{\Lambda}z} \tag{2.34}$$

Comparison to the non-grating case, Eq. 2.27, shows that the grating results in the addition of a $q\frac{2\pi}{\Lambda}$ term to the propagation constant difference $\Delta\beta$.

We saw in the non-grating coupling Section 2.2.2 that the maximum coupling occured when the waveguides were the same with the same effective indices, such that $\Delta\beta = 0$. The grating can thus be designed so that the updated mode matching condition

$$\Delta\beta - q\frac{2\pi}{\Lambda} = 0 \tag{2.35}$$

is satisfied.

This will not assist the transition across the barrier, as the upper waveguide width can already be narrowed enough to bring its effective index to the same value as that of the lower waveguide. However, it was found in Section 2.2 that the taper width needs to reduce to submicron values of $0.7\mu m$ which is difficult for fabrication to achieve. Thus a grating could instead be used to increase the required end width to a more manageable size, by using its wavevector. For intial tests, however, the grating simply adds complexity to the fabrication, and is omitted. Future work may wish to examine gratings in more detail.

Inspiration was desired from other fields.

2.3.1 Adiabatic Transfer

Similarities exist between quantum mechanics and optics [184, 194, 195]. The similarities arise because both are results of wave equations, the Schrödinger and Helmholtz equations, which share the same format. For a waveguide, the propagation direction replaces the temporal component of quantum systems, and the refractive index replaces the potential [194, 196, 197]. There is interest in these similarities, because optical waveguides can provide experimental accessibility to the realm of quantum effects [195, 196, 198].

Quantum mechanics possesses a technique called STIRAP (stimulated raman adiabatic passage) which is an adiabatic population transfer between two states,

coupled through a third intermediate state [199, 200]. Adiabatic means that the system evolves slowly enough that the single mode state is preserved [201–204]. The optical analogy is CTAP (coherent tunneling by adiabatic passage) which transfers a mode from one waveguide to another, through an intermediate waveguide [194, 196, 198, 205–208].

CTAP has been experimentally demonstrated using three identical waveguides. In what is called a counter-intuitive process [194, 196, 205], the output waveguide slowly comes close to the intermediate waveguide so that they couple together. Then the input waveguide comes closer to the intermediate waveguide so that the mode transitions between them, before moving away again. The mode then transitions from the intermediate waveguide to the output waveguide. The result is that the input and intermediate waveguides have no light at the end, while the output waveguide supports all the mode [194].

The coupled equations for the three waveguide system is [194–196, 198, 200, 201, 205, 208, 209]

$$\begin{aligned} i\frac{dA_L}{dz} &= -\kappa_L A_C \\ i\frac{dA_C}{dz} &= -\kappa_L A_L - \kappa_R A_R \\ i\frac{dA_R}{dz} &= -\kappa_R A_C \end{aligned} \tag{2.36}$$

the formalism of which compares to the two coupled waveguides form in Eq. 2.27, where κ are the coupling coefficients for left and right guides, L and R respectively, to the centre, C.

The eigenvector of the adiabatic transfer can be solved from Eq. 2.36 [194–196, 198, 200, 205, 208, 209].

$$\left(\frac{\kappa_R}{\sqrt{\kappa_R^2 + \kappa_L^2}}, 0, \frac{-\kappa_L}{\sqrt{\kappa_R^2 + \kappa_L^2}} \right) \tag{2.37}$$

This is the zero eigenstate solution [201], which can be seen to result in a dark state for the centre waveguide. The counter-intuitive aspect comes from the form of the solution in the left and right waveguides. If the left waveguide is selected as the input, then intially the coupling κ_R between the right and centre guides must be high. This is why experimentally the output waveguide is brought close to the intermediate waveguide first. For the mode to have transferred to the right waveguide at the end of the process, then the coupling κ_L between the left and centre guides must be high and κ_R must become low. Experimentally this is

why the output guide moves away from the intermediate waveguide as the input waveguide comes closer. The rate of change of κ_R and κ_L must still be slow enough to be adiabatic, but once that requirement is met the coupling behaviour is insensitive, which will relax processing requirements [206, 207].

The eigenvector solutions of the two coupled waveguide Eqs. 2.29 and 2.30, in the case where $\Delta\beta = 0$, is

$$(\pm\sqrt{\kappa_a}, \sqrt{\kappa_b}) \tag{2.38}$$

The eigenvectors produce power transfer between the two waveguides. For the particular adiabatic eigenvector of the three waveguide set-up, Eq. 2.37, there is likewise a split between two waveguides, skipping the intermediate third waveguide which possesses no power at the end of the transition.

This CTAP method can be used with the current vertical monolithic integration platform where instead of bringing waveguides physically closer to the intermediate waveguide, lateral tapers can be used to alter the effective index of the guides to incite coupling between them.

The intermediate waveguide is placed in the barrier region between the passive and active waveguides. The requirement remains that the mode from the passive upper waveguide cannot overlap into the absorbing core of the lower active waveguide. The index of the intermediate waveguide has to be chosen accordingly.

Unlike the CTAP waveguiding experiment the waveguides cannot be identical in the current platform. The effective indices of the upper and lower waveguide will have to be reduced by lateral tapers to match the intermediate waveguide, or the intermediate waveguide could be reduced to match the lower waveguide. This means that the intermediate waveguide is limited to a maximum index equal to that of the upper waveguide, but can be any index below that. Figure 2.9 displayed that the effective index of the lower waveguide doesn't change considerably with its waveguide width, and that was why it was not varied in the taper transition simulations. For the new purpose of adiabatic transfer, it would be desirous to alter the lower waveguide's width and mimic the CTAP process, but it takes a large change in width to incur any change in effective index. Furthermore, the upper waveguide effective index is changed by altering the lower or intermediate waveguide widths, so the upper waveguide would need to be expressed as a function of the lower waveguides.

CTAP conditions should be possible in a monolithic platform, and could be investigated in future work. Initially, however, the complications of tapering multiple sections, requiring more complicated geometries and additional etches, were avoided. An intermediate waveguide is inserted into the barrier region, but

no attempt is made to taper it or the lower waveguide. The upper waveguide remains the solely tapered section. The added intermediate waveguide should still increase coupling following CTAP, and if successful then full analysis could provide a truly adiabatic transition.

2.3.2 3 Waveguide Optimization Simulations

The introduction of the additional intermediate waveguide also introduces more variable parameters. The index, thickness and position of the new centre waveguide must be chosen.

As mentioned previously the index must be less than the upper waveguide, so that the mode is still preferentially centred around the upper passive waveguide. The position of the additional waveguide in the barrier region must be far enough away from each existing waveguide so that the supported mode in those guides is unaffected. Once more the upper passive waveguide mode is of primary importance and so must certainly be unaffected. The restriction on the lower active mode is more lenient, but the confinement must remain as high as possible so the mode experiences the maximum gain from the material when resident there.

As there is no clear restriction on the combination of index, thickness and position, simulations can be performed for all combinations. Figure 2.22 plots a surface, which provides all combinations of parameters that maintain isolation of the upper and lower waveguides. Isolation was taken to mean that there was less than 1% overlap of the upper waveguide mode into the lower absorbing active waveguide. Any point on the surface can then be investigated to see if it maximises transmission.

Growers have their preferred calibrated compounds which helps narrow down the options of Figure 2.22. The resulting intermediate waveguide dimensions chosen are a thickness of 250nm, positioned 250nm above the lower active waveguide core. The index of the intermediate waveguide is 3.3. This is higher than the lower waveguide and less than the upper waveguide, as could be compared in Table 2.1 or Figure 2.9.

To validate the result of the intermediate waveguide parameter surface, BPM simulations of the up-down-up transition can be performed for varying refractive index of the waveguide. Figure 2.23 illustrates that indeed the optical output is maximised for an index of 3.3. A 3% variation in index results in a decrease in transmission to $< 40\%$.

Just as with the solely two stacked waveguide case, the transmission for different taper lengths can be examined, Figure 2.24. BPM simulations indicate that a

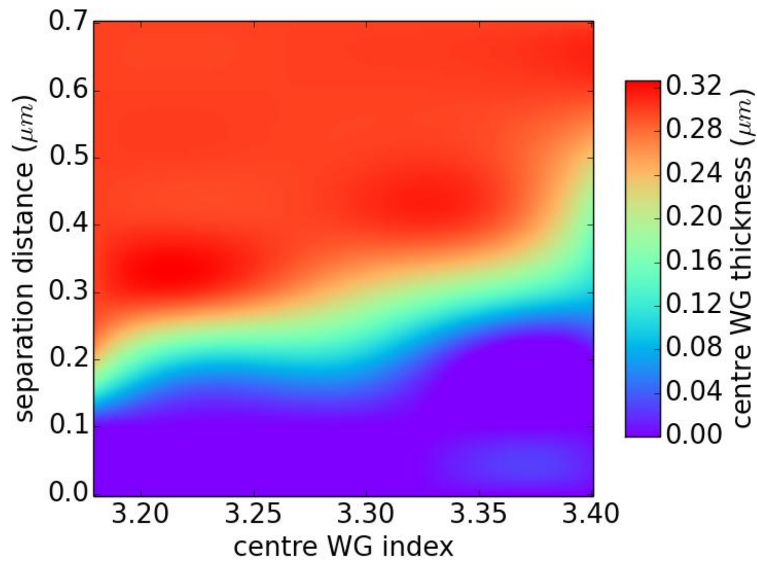

Figure 2.22: Surface depicting the maximum centre waveguide thickness permissible for a combination of refractive index and separation distance from the upper WG that maintains isolation of the passive and active waveguides.

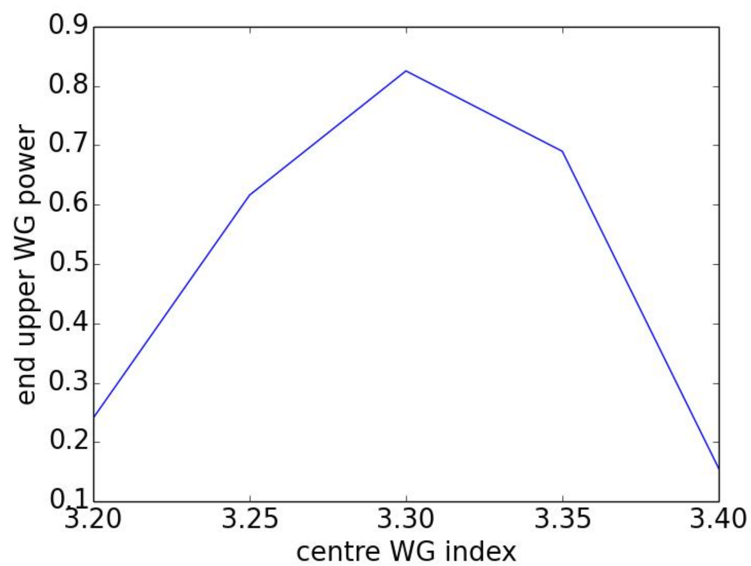

Figure 2.23: The power in the upper WG at the end of the transition in an up-down WG device for different intermediate WG refractive indexes.

taper length below $200\mu m$ is too sudden to allow a proper vertical transition, the power monitor behaviour can be seen to be much different from the behaviour for longer taper lengths. A length of $600\mu m$ should be sufficient to transition the bulk of power from the upper to the lower waveguide.

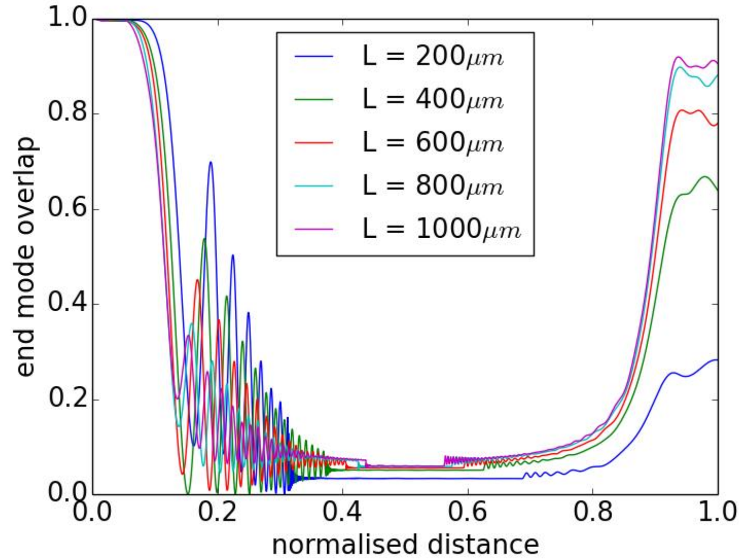

Figure 2.24: The overlap with the ideal end mode of the 3WG up-down device vs. distance for different taper lengths L. Due to the symmetry of the device the launch mode and end mode are equal.

Fabrication tolerances have been alluded to throughout this section, and their impact is now examined. The standard fabrication tolerance is $\pm 0.2\mu m$ in the Tyndall National Institute III-V fabrication facilities, coming from alignment of photo-lithographic masks and exposure of the photoresist. A feature can either be over-exposed or under-exposed, making it smaller or larger than the design intended. Fabrication designs that avoid these tolerances will be outlined in Chapter 4. In order to design a completely fabrication error free device the taper would need to begin at a width $0.2\mu m$ wider and end $0.2\mu m$ narrower than the actual transition point to accommodate the $\pm 0.2\mu m$ tolerance. In the most under-exposed case, the starting width could be $0.4\mu m$ wider than the ideal design, resulting in a width of $1.1\mu m$ rather than the design of $0.7\mu m$. The most over-exposed case could result in an end width of $0\mu m$. While $0\mu m$ isn't realistically achievable the taper need only end at $0.4\mu m$ or below to complete the transition, it doesn't matter if some remains after that. The taper that achieves acceptable adiabaticity changes from $0.7\mu m$ to $0.4\mu m$ over $600\mu m$, thus the taper slope is $\frac{1}{2000}\mu m$ per μm, which means that with an increase in width of $0.4\mu m$ to the taper, the device size will increase by $800\mu m$ per transition taper. This

clearly contravenes the small footprint aim of a PIC, and so designing impervious tapers isn't feasible. The resolution of photolithography is much better in many foundries, and so fabrication tolerances would not be such a large concern. In that case the length of an impervious taper would be reduced and might become acceptable in size.

To remove concern with the taper at widths exceeding $0.7\mu m$, the linear taper required to adiabatically alter the mode from a ridge width of standard $2.5\mu m$ to the transition region can be computed. Figure 2.25 shows the output power for different lengths, illustrating that the taper in this case can be very short, no more than a conservative $50\mu m$ linear taper length is required.

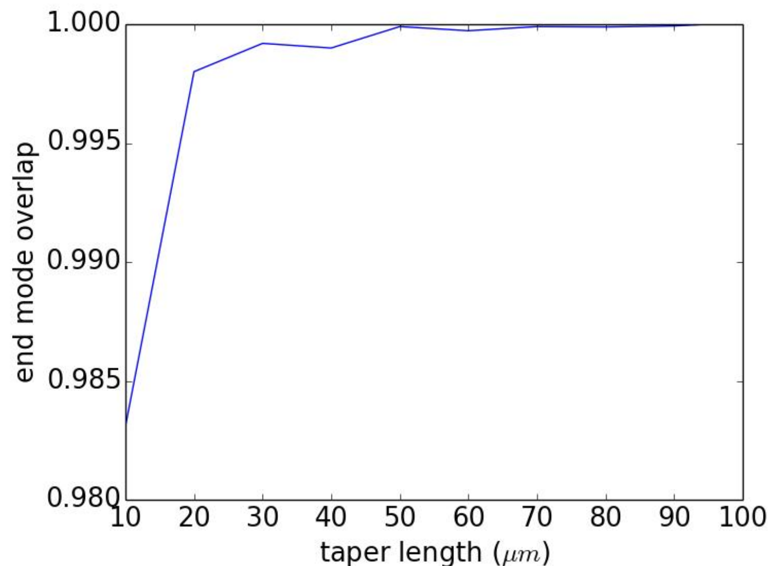

Figure 2.25: The overlap with the ideal end mode of the upper WG for different quick taper lengths, narrowing from a standard mode supporting ridge width of $2.5\mu m$ to the start of the transition region.

Figure 2.26 displays the BPM simulation monitor power along the propagation distance of the mode for an up-down-up transition between the upper passive and lower active waveguides. The addition of the intermediate waveguide increases transmission substantially, above 85%, compared to below 20% originally. The new vertical coupling method makes monolithic vertical integration of the passive and active waveguides feasible, allowing high optical transmission between the waveguides so they can be integrated on a single PIC to achieve photonic integrations aims.

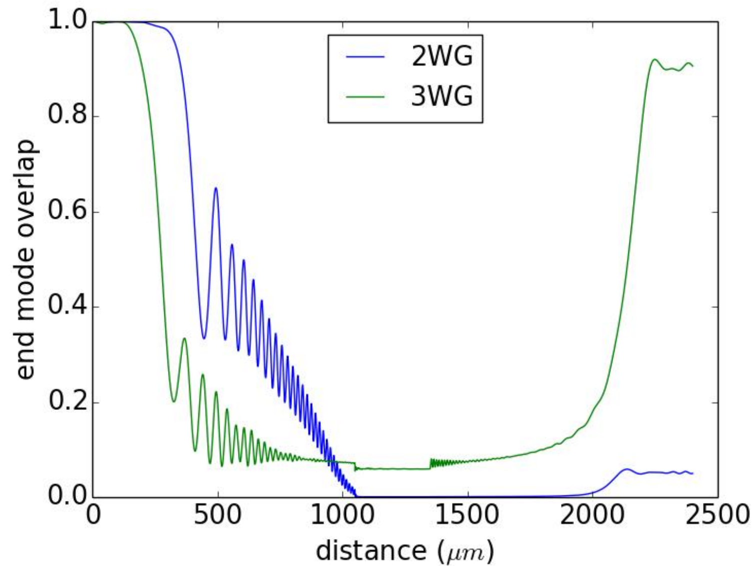

Figure 2.26: Overlap with the ideal end mode along the propagation in the up-down WG structures, comparing the optimum transmission for just the 2 WGs and for 3 WGs with the inclusion of an additional intermediate WG.

2.4 Epitaxial Material Modelling

The full aim of this work is to vertically monolithic integrate an MZM above a laser for telecoms applications, providing advanced modulation formats. Thus, the lower active waveguide in the structure needs to emit at the telecoms wavelength near $1.55\mu m$ with strong output. InP has already been described in this work as the platform required for emission at that wavelength, and the semiconductor alloys used to achieve the correct wavelength are the quaternary compounds AlGaInAs and GaInAsP.

Figure 2.27 is the familiar plot of band gap vs lattice constant for III-V semiconductors. In order to epitaxially grow material successfully onto InP, the material has to be lattice matched to InP. On Figure 2.27, only material on the vertical line of InP can be successfully grown. It can be seen immediately that there are four ternary compounds and a host of quaternary compounds that satisfy lattice matching. However, active material must be at the correct wavelength for emission, and passive material must be transparent, all the while having suitable indices to guide light.

The intermediate waveguide is only needed to provide a mid step for the vertically transitioning light, thus bulk material is satisfactory if it can be found with the correct index and transparency. In order for the material to be grown on InP, it must be lattice matched, and that corresponds to an indium concentration

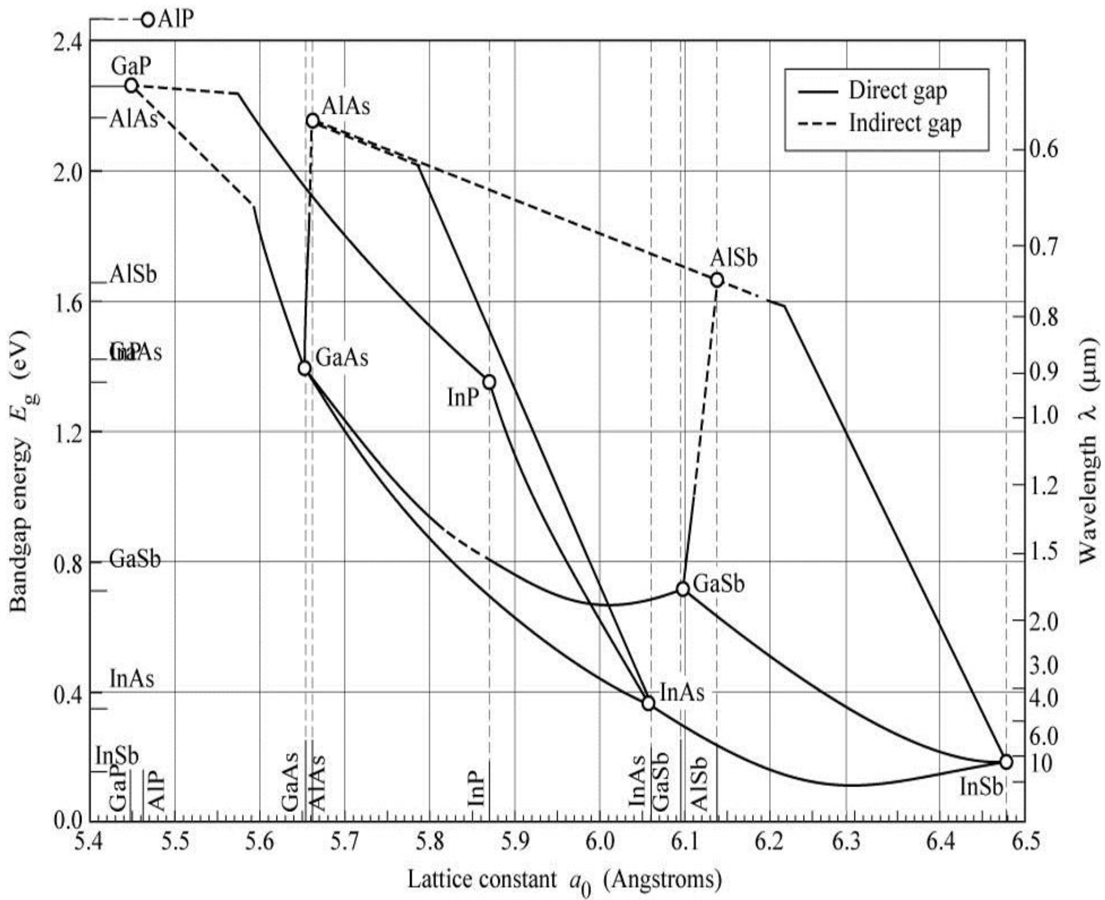

Figure 2.27: Band-gap vs. lattice constant for III-V semiconductor alloys at room temperature [210].

of 52%–53% in AlGaInAs. As these materials are so fundamental to epitaxial growth on an InP platform, which is required for gain in telecoms, the material is well known and modelled. Table 2.2 lists some InP lattice-matched ternary compounds and quaternary compounds with useful refractive indexes, along with their band gap wavelength. The band gap wavelength of different AlGaInAs compositions can be seen on the surface of Figure 2.28, and is a more useful value, because it is easier to measure, that growers use to select their growth compounds.

Table 2.2 outlines that none of the ternary compounds possess the correct refractive indexes. The intermediate waveguide composition choice is $Al_{0.30}Ga_{0.18}In_{0.52}As$, which has the correct refractive index of 3.3 found to produce the best coupling transmission in BPM simulations, while simultaneously being transparent. It is transparent because its band gap wavelength is $1.1\mu m$, corresponding to an energy gap larger than the incoming $1.55\mu m$ wavelength can excite.

Table 2.2: InP lattice-matched materials with refractive indices that suit the passive waveguides required for vertical monolithic integration on a 1.55μm wavelength-based PIC.

Compound	Refractive index	Band-gap wavelength μm
$Al_{0.30}Ga_{0.18}In_{0.52}As$	3.3	1.0983
$Al_{0.13}Ga_{0.34}In_{0.53}As$	3.43	1.4018
$Al_{0.36}Ga_{0.11}In_{0.53}As$	3.28	1.000
$Ga_{0.08}In_{0.92}As_{0.18}P_{0.82}$	3.43	1.0141
$GaInAsSb$	–	> 1.55
$Al_{0.48}In_{0.52}As$	3.35895	0.8553
$Ga_{0.47}In_{0.53}As$	4.15457	1.6839 (>1.55)
$GaAs_{0.5}Sb_{0.5}$	–	1.7292 (>1.55)
$AlInAsP$	–	–

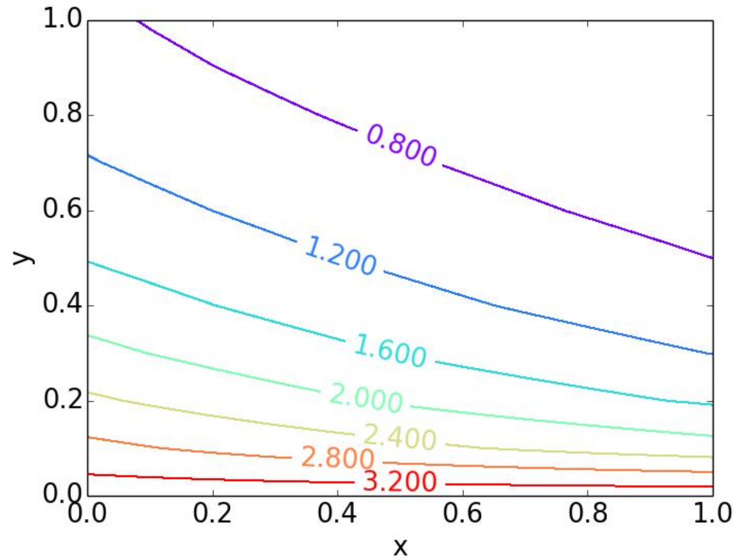

Figure 2.28: Surface plot of the band gap wavelength (in μm) of different x and y compositions of $Al_{xy}Ga_{(1-x)y}In_{1-y}As$.

The intermediate waveguide composition has at this point been determined by consulting models based on measurements of III-V semiconductor properties. The same method can be utilised to find a bulk compound with the same refractive index as the average of the upper passive waveguide.

Table 2.2 outlines that AlGaInAs or GaInAsP are the only compounds with suitable indices for the current application. The condition of transparency finalises the choice to $Al_{0.13}Ga_{0.34}In_{0.53}As$. It is no accident that the band-gap wavelength, becoming the emission wavelength when forward biased, is similar to that from the full MZM material quantum wells. Figure 2.29 shows

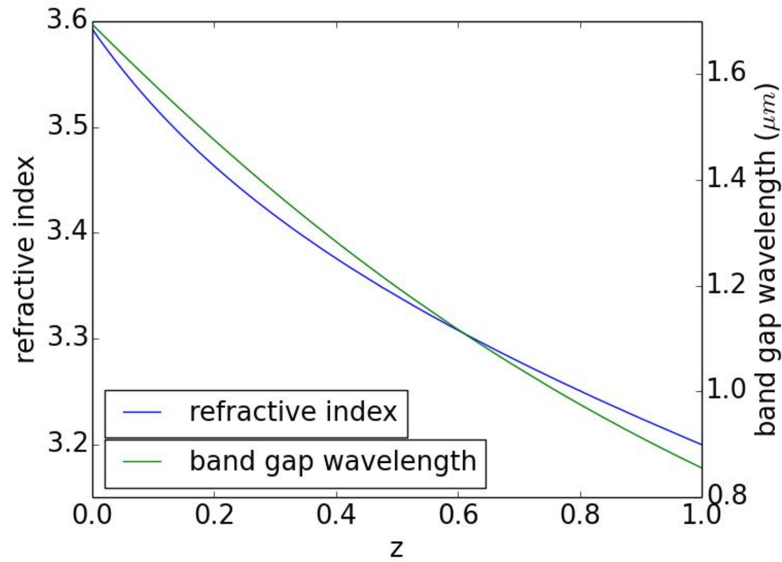

Figure 2.29: Refractive index at 1.55μm vs. band-gap wavelength for InP lattice-matched AlGaInAs compositions, given by $Al_{0.47z}Ga_{0.47(1-z)}In_{0.53}As$

that the refractive index of InP-matched AlGaInAs increases with increasing bandgap wavelength. The AlGaInAs composition modelled is expressed by $[Al_{0.48}In_{0.52}As]_z\,[Ga_{0.47}In_{0.53}As]_{(1-z)}$ when lattice matched to InP. It is only the much thicker core region of the upper waveguide that results in it having a greater index than the higher band gap wavelength lower waveguide, and thus dominant light guiding. It can also be thought wise to use the same compound for all the waveguides, AlGaInAs being used for the lower active waveguide QWs, the upper passive waveguide, and the intermediate waveguide.

2.5 Discussion and Conclusion

In this chapter, waveguides were studied beginning with analytical expressions, before expanding to numerical techniques when the solutions became too complex or the system became large. It was seen, with mode solutions and coupled mode behaviour, that the results from the analytical analysis carried out in 2D matched those of the 3D results. These analytical investigations provided informative understanding of the systems, that may otherwise be lacking in numerical calculations.

The correlation of different techniques, relying on numerical computation, to solve problems such as the isolation barrier thickness and the cut-off mode support ridge width, indicated that the solutions were correct.

A design that places a passive waveguide, with a greater thickness and so higher average refractive index, above an active waveguide has been calculated. The vertical integration of the two guides was achieved solely through the use of lateral tapers, providing a monolithic solution with the associated benefits of lower cost due to avoiding regrowth, having simpler coupling packaging, and supplying high density of devices. Different taper geometries were investigated with the final choice being a linear taper, due to its high transmission and simplicity.

The waveguides are isolated from each other away from the vertical coupling region, allowing each to be optimised independently. The isolation was achieved by $1\mu m$ thick barrier epitaxial layers between the guides during the growth sequence. The $1\mu m$ thick barrier is so successful at isolating the mode in the upper passive waveguide away from the lower absorbing active waveguide that no acceptably significant vertical coupling could be excited between the guides at any ridge width combination. However, inspiration was taken from quantum mechanical processes to introduce an additional third passive waveguide into the barrier region with the sole purpose of aiding a vertical transition between the vertically stacked waveguides.

The mode couples from the upper to the lower waveguide when the upper ridge width drops below $0.7\mu m$, and a vertical transition is completed by an upper ridge width of $0.4\mu m$. In order to achieve an adiabatic mode transfer with the three waveguide stacked structure, the upper narrowing taper length must be in excess of $600\mu m$. The longer the taper, the slower the mode transformation, the more power can be coupled between the stacked waveguides. However the key aim of photonic integration is to minimise the size of devices, so that there is an upper bound on the length possible.

The throughput for an up-down-up propagation transition is 85%, indicating that vertically coupling isolated waveguides is a viable option for photonic integration, achieving greater coupling efficiency than externally output coupled devices.

This chapter also used experimentally attained material models to design the epitaxial structure of an up-down waveguide device. The structure was chosen to be a mix of AlGaInAs and InP, achieving all the band-gaps required. The succeeding chapters shall discuss the growth of the up-down waveguide structure, and its testing and characterisation.

Chapter 3

Inverted N-I-P laser

The preceding Chapter 2 designed the up-down WG structure from a waveguiding point of view. The materials required for a physical implementation based on an epitaxial growth were found using models based on experimental measurements. This Chapter delves further into the requirements of the epitaxial growth.

Until this Chapter, doping had not been dealt with. The integrated device requires a doping profile to create a semiconductor junction. The junctions set up an intrinsic region centred at the core of the waveguides, where dopants would otherwise be absorptive to the guided optical mode. The intrinsic regions are where light is generated or absorbed, acting as emitters or detectors for active material.

The doping profile for a single waveguide is straightforward, one side is n-type doped and the other is p-type doped. Positive and negative electrical contacts are then placed onto the p- and n-doped semiconductor [123]. Typically the InP substrate is n-doped because the n-dopant, usually Si, is more stable under long growth temperatures [123]. N-doped InP is less absorptive [123] which is helpful because the supported mode will reside in part within the substrate.

For two vertically stacked waveguides the profile becomes slightly more complicated. If each were to remain in the standard p-i-n configuration, then when stacked the overall structure would become p-i-n-i-p-i-n, with an additional intrinsic region lying between the waveguides. While such an additional intrinsic region would not altogether be problematic (it may even be beneficial because there would be less dopants in the vertical transition region), but it would increase the thickness of the barrier. The barrier increase would result from the space required to dope the n- and p-regions. Further, the top most p-i-n would require an n-contact metal while the bottommost p-i-n would require a p-metal contact. Thus the barrier region contacts for each waveguide would have to be separate,

requiring two different etch depths to reach the designated contact layers. The additional etches contradict the aims of monolithic photonic integration, minimising the number of fabrication steps to minimise the cost [50, 93, 169], while the increased thickness may cease the vertical coupling outlined in Chapter 2 [151, 186].

Both stacked waveguides will instead share a contact in the middle of the structure. The resulting doping profile can then either follow the form p-i-n-i-p or n-i-p-i-n, with a shared n-contact or p-contact respectively. The reasoning behind InP substrates always being n-doped also informs the reasoning to select a p-i-n-i-p structure.

N-dopants have higher mobility than their p-counterparts [211], so that by being placed in the shared region the current should more successfully flow between contacts and semiconductor. The fact that n-dopants are less absorptive than p-type [123] allows a greater vertical optical transmission through the barrier region, with less absorptive losses.

Another determining factor in adopting a p-i-n-i-p structure is that for our device, the upper passive WG is of chief interest. This passive WG is destined to become a high-speed modulator. A high-speed modulator is more complex to fabricate than a laser cavity, which only requires simple waveguides with standard contacts. A high-speed modulator on the other hand requires waveguide bends, metal crossings over waveguides, planarisation, and low capacitance high speed contacts [55, 56, 68, 82–88]. It is of prime importance to have clear access to the upper WG, and that is why it is placed on top. For the same reasoning it is not wished to invert the modulator as it could introduce further complexity. Thus the upper WG remains in the standard p-i-n configuration, requiring the lower active waveguide, the laser, to be inverted to an n-i-p configuration [93, 212, 213].

The benefits of n-doped substrates have been outlined above. It now falls to outline the restrictions of a p-doped substrate that the laser will possess.

The typical p-dopant for InP is Zn, and it is known to diffuse heavily during the high temperatures required for epitaxial growth [123, 214]. If these dopants enter the QW core region then the optical efficiency will be ruined [215]. When the p-dopants are the last layer deposited in an epitaxial growth their diffusive contribution is not as severe. For vertical integration of multiple waveguides however, the epitaxial growth times will be longer than any single slab waveguide, owing to the additional layers.

The behaviour of p-dopant diffusion in an InP-based p-substrate laser was investigated first to determine if a p-substrate is viable for vertical monolithic

integration.

3.1 Epitaxial Growth

Figure 3.1 shows the band diagram of an InP laser with AlGaInAs QWs, for emission at a wavelength of 1.55μm. The InP transitions to the AlGaInAs QWs through a number of SCH (separate confinement heterojunction) layers. The main function of these SCH layers is to optically confine the light mode, while the QWs confine carriers and promote spontaneous emission transitions to create the mode [51, 189]. The SCH layers are lattice matched to InP to aid a successful growth. The index of the SCH layers progressively deviate from that of InP toward the QW's index, to create strong mode confinement within the QWs. If layers deviate from the InP lattice too abruptly then the growth will not be successful and the mismatches will create defects.

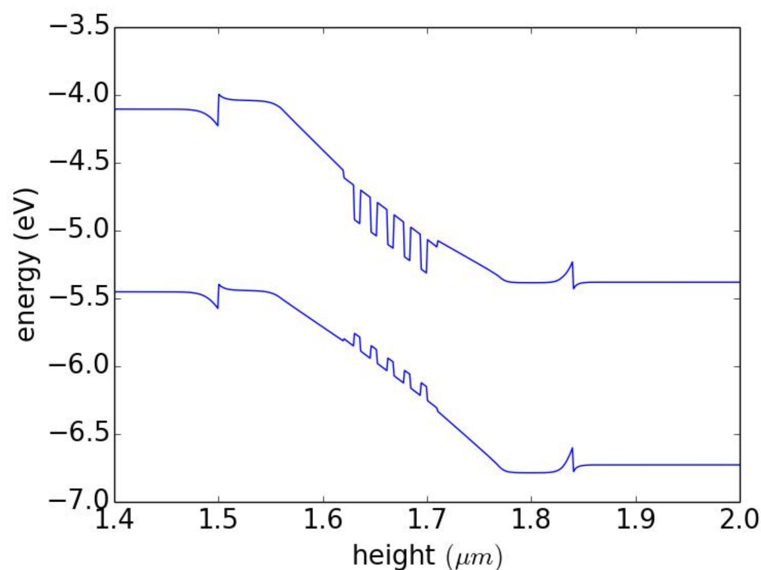

Figure 3.1: Band diagram of the p-substrate InP/AlGaInAs QW laser, produced with SimWindows [216].

Quantum wells are constructed by growing thin epitaxial layers, sandwiching a high band gap material between two lower band gap materials. This creates energy band wells as seen in Figure 3.1. The deliberately different composition of the well and barrier layers can result in either a compressive or tensile strain of the QW, depending on if the well lattice constant is greater of less than the barrier respectively. The strain creates a corresponding increase or decrease in the band-gap energy if it is compressive or tensile. Both types of strain also

reduce the threshold current of the material, making them more electro-optically efficient [189].

With the knowledge of p-doped substrate restrictions in mind a first epitaxial growth was designed that reduced the p-doping density before the core region. Table 3.1 is the epitaxial layer design of a p-substrate laser. Variations of this design were grown and subsequently fabricated. Rather than specifying the refractive index as in Table 2.1 for waveguiding in Chapter 2, the photoluminescence (PL) of each layer is specified in Table 3.1. As the band-gap of materials is easier to measure than the index, growers have calibrated compositions with measured PL, and thus this is the preferred parameter to deliver in designs, along with the estimated x and y concentrations.

Table 3.1: Epitaxial design of three inverted lasers, (a) with reduced p-doping concentration, (b) with pulled-back doping reducing layer #3 to a thickness of 340nm and introducing an additional 160nm thick undoped InP layer #4b before the SCH layer #5b, (c) for carbon blocking layer #3 was reduced to 400nm while layer #4 was extended to 160nm and replaced with carbon doping of $10^{18}cm^{-3}$. Iterations (a) and (b) do not require a layer #5.

#	**Layer**	**Material**	**PL**	**Thick**	**Doping**	**Type**
			nm	nm	cm^{-3}	
14	N cladding	InP		1000	$3{\cdot}10^{18}$	Si
13	N cladding	InP		500	10^{18}	Si
12	SCH	AlGaInAs	913→937	10	10^{18}	Si
11	SCH	AlGaInAs	913	60	10^{18}	Si
10	SCH	AlGaInAs	1030→913	60	NUD	
9 (×5)	Barrier	AlGaInAs	1100	10	NUD	
8 (×5)	Well	AlGaInAs	1530	6	NUD	
7	Barrier	AlGaInAs	1100	10	NUD	
6	SCH	AlGaInAs	913→1030	60	NUD	
4c	SCH	AlGaInAs	913	160	10^{18}	C
3c	P buffer	InP		400	$4{\cdot}10^{17}$	Zn
5b	SCH	AlGaInAs	913	60	NUD	Zn
4b	P buffer	InP		160	NUD	Zn
3b	P buffer	InP		340	$4{\cdot}10^{17}$	Zn
4a	SCH	AlGaInAs	913	60	$4{\cdot}10^{17}$	Zn
3a	P buffer	InP		500	$4{\cdot}10^{17}$	Zn
2	P+ buffer	InP		1000	$> 1.5 \cdot 10^{18}$	Zn
1	Wafer	InP				

The first growth reduced the doping concentration of the p-InP adjacent to the SCH layers to $4 \cdot 10^{17}cm^{-3}$, from a value of $10^{18}cm^{-3}$ for an equivalent p-i-n laser. The same growth was simultaneously performed, with the same layer structure as Table 3.1(a), but with an n-substrate in place of p-substrate. This

growth was performed in the hope that the n-doped substrate would attract the p-dopants grown upon it, pulling diffusion down into the substrate away from the QW core. It will be shown in Section 3.3 that the decrease in concentration and the use of an n-substrate was not sufficient to halt efficiency-ruining dopant diffusion.

For a more drastic and robust dopant reduction the doping profile was simply pulled back from the QWs on the p-side. The epitaxial layer design in Table 3.1(b) had its p-cladding layer split into layer #3b with a thickness of 340nm p-doped InP and layer #4b with a thickness of 160nm undoped InP.

An alternative method doped the SCH layer #4c of the epitaxial design in Table 3.1(c) with carbon, and increased its thickness to 160nm. The p-InP layer #3c was consequently reduced to a thickness of 400nm to accommodate the expansion of the SCH layer above it. In this iteration the carbon doped layer is used as a blocking layer to restrict any Zn dopant diffusion from penetrating through to the QW core.

Figure 3.2 outlines the different doping profiles of the growths. The following Section 3.2 outlines the fabrication process and Section 3.3 follows the testing of the different laser growths.

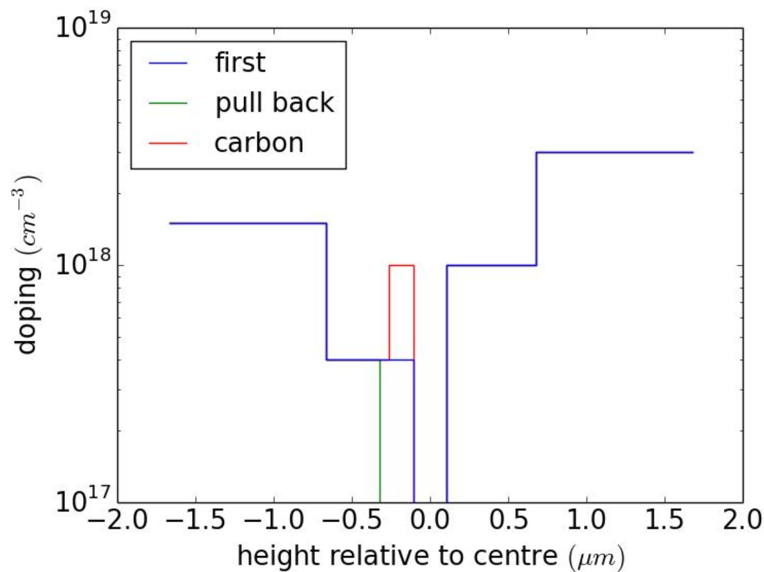

Figure 3.2: Doping profiles of the different p-substrate laser growths.

3.2 Fabrication Design

3.2.1 Fabrication Process

As discussed in depth in Chapter 1.2.1, the aim of monolithic PICs is to minimise the fabrication steps, which include etches and metal deposition.

An etch is required to define waveguide ridges on a PIC, creating the correct refractive index profile to support modes, as discussed in Chapter 2. After the etch, silicon dioxide is grown over the semiconductor material encapsulating the waveguide. This serves to greatly reduce the leakage currents along the outside of the semicondutor ridge, and also provides an insulating layer to support and isolate metal contacts. The silicon dioxide can be selectively etched away to create oxide openings which allow metal-semiconductor contact at the top of the ridge. Thus electrical contact can be made only where desired with electrical isolation elsewhere. Metal deposition is clearly required then to allow electrical injection into the photonic devices. Different sections with separate biases must be unconnected, requiring metal to be selectively deposited across the device.

These basic requirements necessitate three mask steps; etch, oxide opening, metal deposition. A fourth mask step is added for an additional etch through the core layers. This deep etch allows an additional top contact to, in this case, the p-substrate. The deep etch also allows isolation between different biased sections because it severs the n-layers completely, creating a higher resistance and forcing all current flow through the near intrinsic region. Thus in total 4 mask steps can create a monolithic PIC.

Figure 3.3 shows a full mask plate, with each of the four steps occupying a quarter of the mask plate. The plate is rotated by 90° at each stage to select the next mask step, allowing alignment to the wafer under fabrication.

Masks used in our research group are usually designed for a quarter of a circular wafer, so that the mask plate would be split into four quadrants. The wafer is split so that a single wafer can be spread across multiple runs, and if any damage happens during a process run then the entire wafer will not be lost. InP wafers used for our research purposes have a diameter of 2-inches, but other sizes are available for other projects.

This Chapter details the investigation of laser material, and while initially in the following Section 3.3 an existing 2-inch mask was reused to produce laser devices, it became apparent that dedicated material characterisation devices were required to investigate the laser material. Using an entire quarter of a 2-inch wafer for characterising devices could be considered a waste of material, as fur-

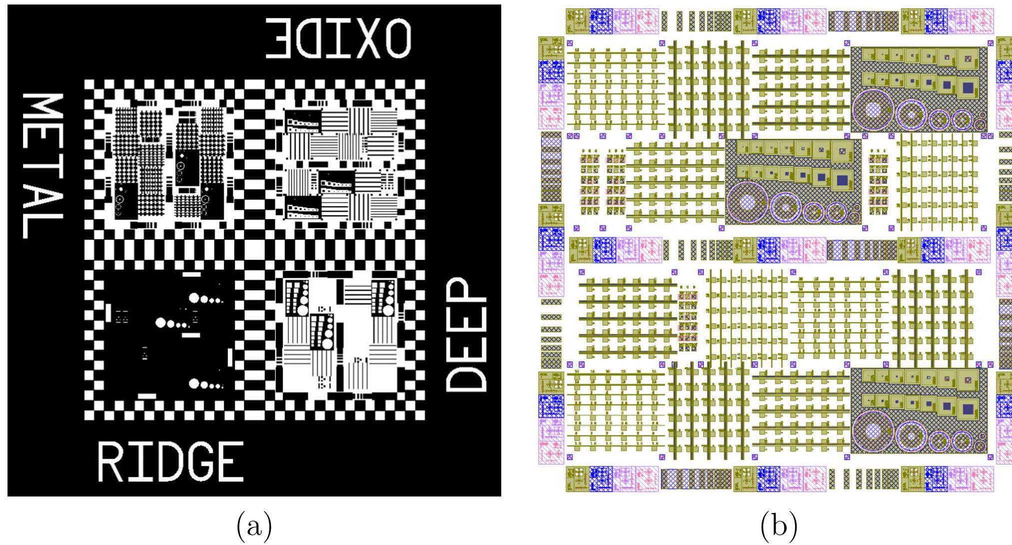

(a) (b)

Figure 3.3: (a) Lithography plate with 4 mask steps used sequentially to produce material test structures such as FP cavities. (b) The 4 mask steps superimposed to illustrate the final device format.

ther destructive measurements may also need to be performed which would then require the sacrifice of an additional quarter. As much of the material as possible should be saved for functional devices. Thus it makes sense to use as little material as possible from a single quarter for characterisation, with the remaining pieces from that quadrant usable for further destructive material-calibrating tests.

The mask of Figure 3.3 is square, $1cm \times 1cm$ in size. The reduced size and squareness of the material test mask allows only a portion of one quadrant of a full wafer to be used. It leaves behind enough material to be used for other material tests, so that the other three quadrants are untouched and ready for full device runs.

As will be outlined in Chapter 4, the full vertically stacked waveguide structure utilises only deep etches to define its waveguides. Thus for this single laser waveguide, only a single deep etch was required through the QW core. This foregoed the necessity of using the “deep” mask step indicated in Figure 3.3.

Figure 3.4 details the fabrication steps that involved the “ridge” mask. The material was coated with silicon dioxide, then photoresist was patterned onto the oxide using the mask. After development, the photoresist remained where the eventual ridges would be. The oxide was then etched away everywhere that wasn’t protected by the photoresist, after which the photoresist was removed completely. The semiconductor material was then etched everywhere that was not protected by silicon dioxide. For a shallow etch, the depth etched down to

is just above the quantum well core of the laser material. For a deep etch, the etch is all the way through the core. With this mask and these fabrication steps, ridges were defined for waveguides.

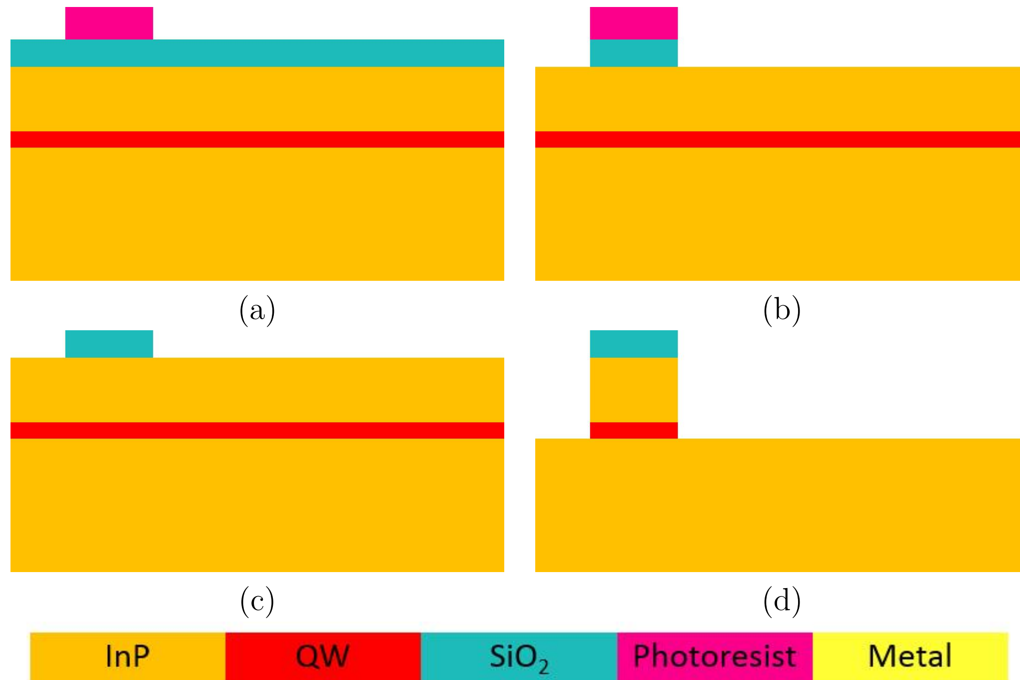

Figure 3.4: Ridge etch steps for laser material characterisation. (a) Silicon dioxide was deposited on the wafer and then photoresist was patterned over the ridge using the mask. (b) The oxide was etched through, but was protected by photoresist over the eventual ridge. (c) The photoresist was removed. (d) The material was etched downward, while the oxide protected and formed a ridge.

Figure 3.5 details the fabrication steps that were required for the "oxide" mask. The material was once more coated with silicon dioxide, and then with photoresist. The photoresist was patterned using the mask, removing the photoresist from those places that would eventually become oxide openings. The oxide was then etched away everywhere that wasn't protected by the photoresist, after which the photoresist was removed. This resulted in openings in the oxide which exposed the semiconductor material for subsequent electrical contact.

Figure 3.6 details the fabrication steps using the "metal" mask. The material was coated with photoresist again. The photoresist was patterned using the mask, removing the photoresist from those places that required metal. Metal was then deposited over the wafer. The photoresist was then removed, resulting in metal lift-off, removing the metal that was on the photoresist. This resulted in separate metal pads on the semiconductor for electrical contact.

The additional "deep" mask layer allows a second etch through the semicon-

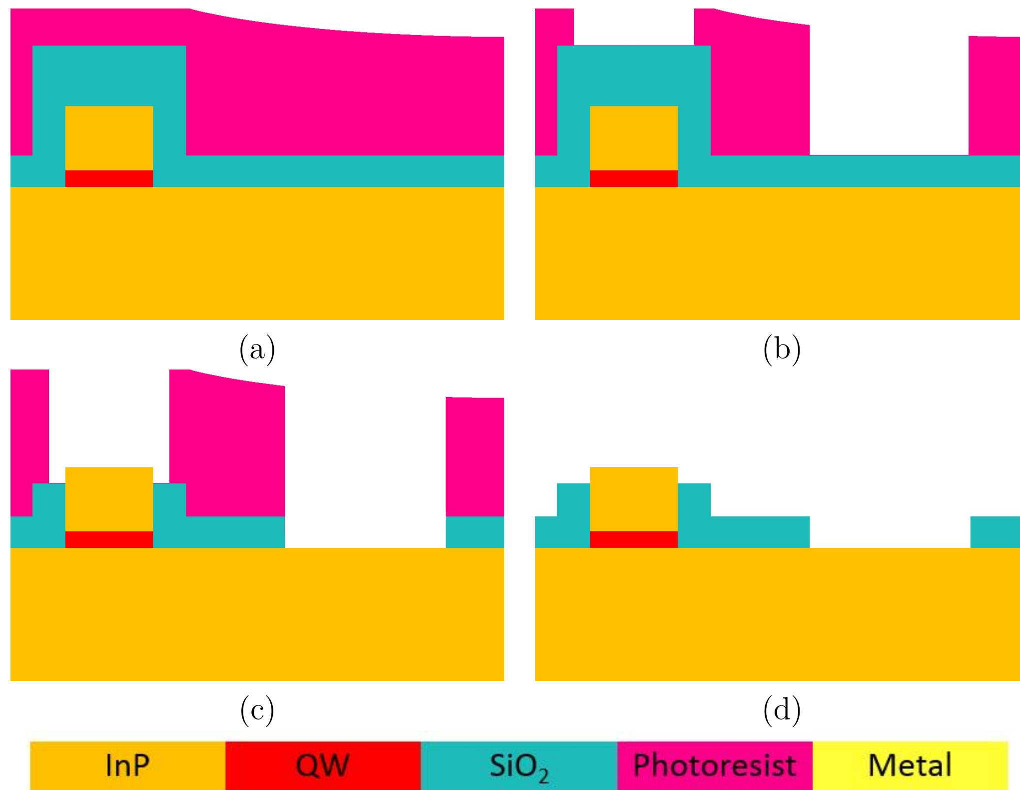

Figure 3.5: Oxide opening steps for laser material characterisation. (a) Silicon dioxide was deposited on the wafer followed by photoresist. (b) The photoresist was patterned using the mask with openings wherever the eventual oxide openings were to be. (c) The oxide was etched away wherever there was no photoresist, allowing contact to the semiconductor. (d) The photoresist was removed.

ductor, so that both a shallow and deep etch are possible. The mask steps above outline a deep etch only process, where the "ridge" mask was used to etch through the core. If a solely shallow etch process was used then the top metal contact for the substrate would remain above the core and wouldn't permit current flow through the intrinsic region. A deep etch is required for top contact to the substrate. The deep etch mask follows the same process steps as the "ridge" mask step, the only difference being the position of the photoresist and the etch depth.

3.2.2 Test Structures

The full mask shown in Figure 3.3 shows a number of test devices. These devices are simple structures, but can reveal important information about a material's functionality.

Blocks of straight Fabry-Pérot (FP) cavities were oriented sideways and upwards, with square metal pads attached to the ridges. Some FP blocks possessed

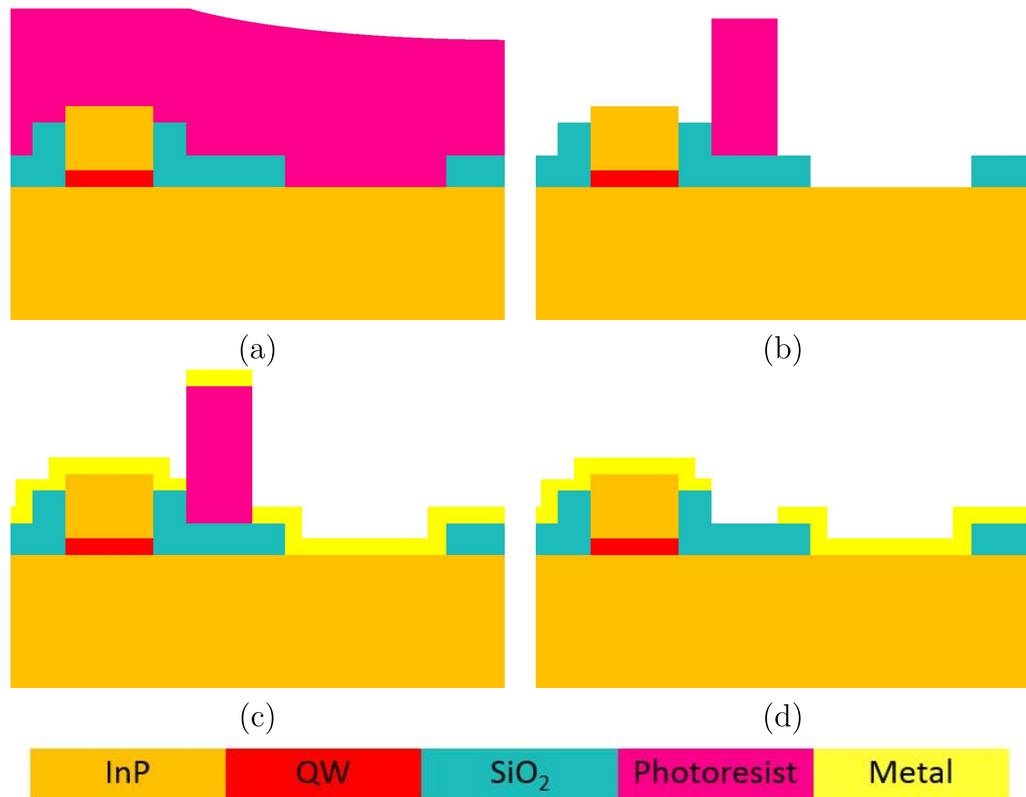

Figure 3.6: Metal lift-off steps for laser material characterisation. (a) Photoresist was deposited on the wafer and (b) patterned using the mask. (c) Metal was deposited over the wafer. (d) The photoresist was removed and lifted off the metal, leaving separate metal contact pads.

both n- and p-contact metal pads, above and below the QW core, which allowed topside probing. Such devices are helpful if the material under test has an insulating substrate which prevents a backside contact. The FP cavities were oriented in perpendicular directions to each other to ensure that the crystal orientation did not affect performance. For decent material and a uniform fabrication process, the device orientation does not noticeably affect device performance.

The FP cavities were designed to have ridge widths varying from $1.5\mu m$ to $15\mu m$. Cleaving the bars created cleaved facets on either side of the cavity, which act as mirrors and formed FP lasers [119, 217, 218]. Pumping electrical current into the FP should produce light emission, which informs of the wavelength of the semiconductor material. The bars of FPs were cleaved into different lengths, and the threshold currents for different length and width FP lasers were extracted to characterise the lasing capabilities of the materials.

Large area diodes are visible on the test mask, Figure 3.3, as circles and squares within large metal blocks. The large area allowed testing even if the fabrication was disastrous, as the probability of some oxide opening is highest

and the quality of the metal contact increases with area because the resistance decreases with area, such that even poor contacts may have acceptably low resistance. Current-voltage and capacitance-voltage measurements were performed on the large area diodes. The circular diodes had an annulus contact, leaving an opening for light injection. The absorption of the material was characterised by illuminating the diode with different wavelength light and recording the photocurrent produced.

One set of square diodes had a large oxide opening, while the other iteration featured serpentine ridges with small oxide openings. The curled ridges have the same total area as the single square oxide opening. Comparison of the two diode types informed about the effectiveness of the oxide opening and the ability of the metal to rise up the sidewalls of the ridges, in addition to informing the electrical leakage due to the sidewalls of the waveguide.

There were also variations of GSG (ground-signal-ground) pads for use with high-speed probes. The GSG pads include iterations that share the same semiconductor layer, are either side of the intrinsic region, or have oxide beneath them. This allows a characterisation of the etch depths and oxide thicknesses using standard high-speed probes. The purpose of these structures was for debugging the fabrication in the event that a problem arose.

The other standard test structures on the material test mask of Figure 3.3 were transmission line measurements (TLM). These consisted of contact pads spaced increasing distances apart. The current flow between the first pad and each subsequent pad were used to accurately determine the resistance of the semiconductor and metal contact.

The total resistance of the device includes the contributions from the contact pads and the semiconductor, and can be expressed as

$$R_T = R_S \frac{L}{W} + 2R_C \tag{3.1}$$

where R_S is the sheet resistance of the semiconductor and R_C is the resistance of the metal contact. By measuring the resistance for different lengths L using pads with width W, the contact resistance can be determined by extrapolating back to $L = 0$.

Visible beside the TLM structures in Figure 3.3, around the outside and bisecting the mask, are alignment marks. These alignment marks were placed on each mask layer and allowed precise alignment of each mask relative to the previous so that all the photoresist patterns lined-up.

The growths outlined in Section 3.1 were fabricated using the process design

outlined in Section 3.2.1 to create the material characterisation structures listed above. The test structures were used to investigate the n-i-p laser growths in the next Section 3.3.

3.3 Testing and Characterisation

3.3.1 LIV Measurements

The first inverted laser growth featured a reduced p-doping density profile, with one growth on a p-InP substrate wafer and another on an n-InP wafer, Table 3.1(a). A quarter wafer was processed with arrays of FP lasers, bars of which were then cleaved for testing. Such bars can be seen in Figure 3.7. The top n-contacts were square metal pads attached to the thin $\sim 2.5\mu m$ ridges, and the top p-contact pads were the other pads connected to the wide p-contact ridge. The FP lasers could be cleaved to different lengths between the pads. For the growth on p-InP wafers, a bottom contact was made from a brass chuck beneath for the p-contact, removing the necessity for a top p-contact as evident in Figure 3.7b and c.

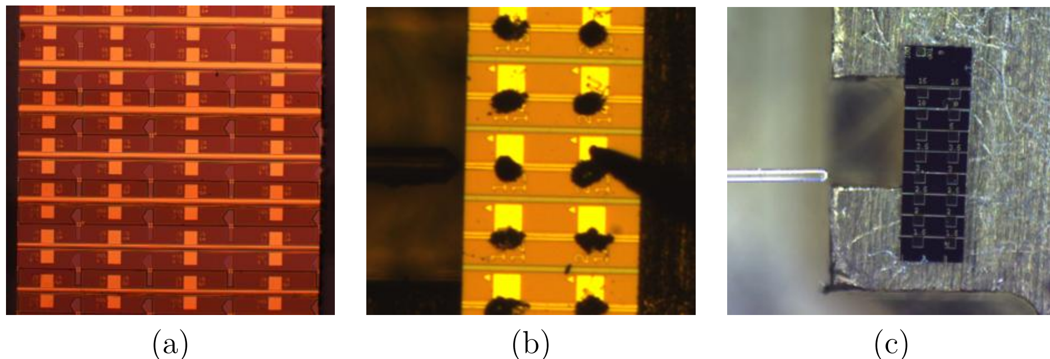

(a) (b) (c)

Figure 3.7: First growth n-i-p lasers, with reduced doping, under test. (a) FP cavities on the n-i-p-n growth required two top contacts, one for the topmost n and one for the p-substrate. (b) The n-i-p-p growth used a bottom p-contact. Here Ag epoxy can also be seen as dark patches over the pad and ridge to increase electrical contact. (c) A bar of FP cavities with different ridge widths, and a lensed fibre used to record optical emission.

Also seen in Figure 3.7b are dark patches over the pad and waveguide ridge. These dark patches are Ag epoxy, and were added to certain bars after fabrication in an attempt to increase electrical contact between the pad and ridge. A lensed fibre can be seen on the left of Figure 3.7b, used to capture optical emission from the FP ridge.

The processing for the initial batch of lasers underwent problems, and no optical emission could be recorded from them. With no information gathered, the mask process of Section 3.2 was designed to allow a full characterisation of new materials. Subsequent fabrications were thus more informative. Figure 3.8 displays a full wafer segment that was processed with the material test mask. The different test structures can be seen as blocks that were subsequently cleaved into individual device bars. A bar of FP cavities with different ridge widths is shown in Figure 3.7c.

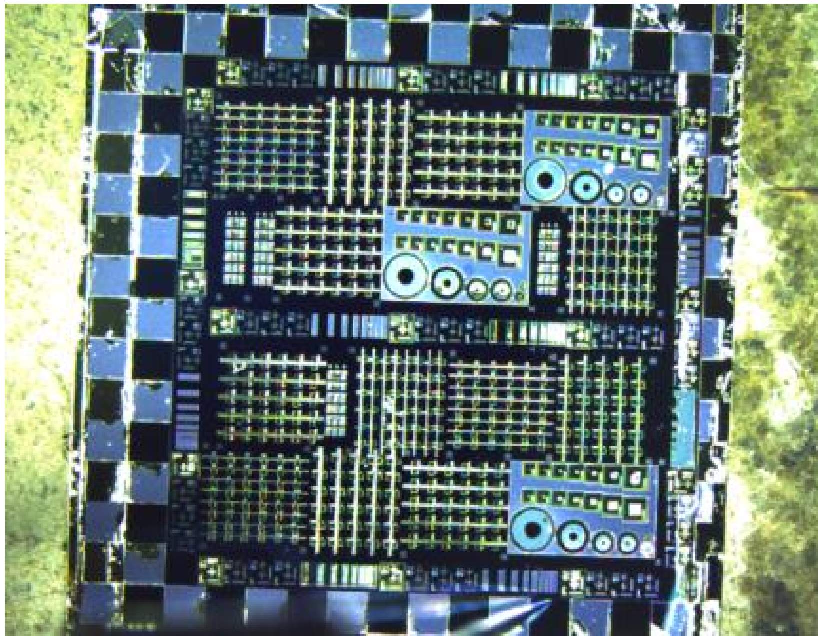

Figure 3.8: A wafer processed using the material test mask, before cleaving.

There was successful electrical contact to these devices, as verified by TLMs, but the lasers only produced weak optical emission. Figure 3.9 displays the spectrum of the p-substrate laser emission across the full range of the measuring OSA, with the noise level of the OSA placed in the foreground. From the wide OSA trace it was determined that there was no emission at unwanted wavelengths, so the injected carriers weren't being consumed elsewhere. What emission existed was correctly centred at $1.55\mu m$, indicating that the epitaxial growth was on the right track.

The above results prompted updated growths as outlined in Section 3.1 and Table 3.1. One iteration pulled back the p-doping entirely from the core region, Table 3.1(b). A second iteration doped a carbon blocking layer at the lowermost SCH layer, Table 3.1(c).

The second round of growths were more successful than the first, producing laser emission. Figure 3.10 plots comparison optical power vs. electrical current

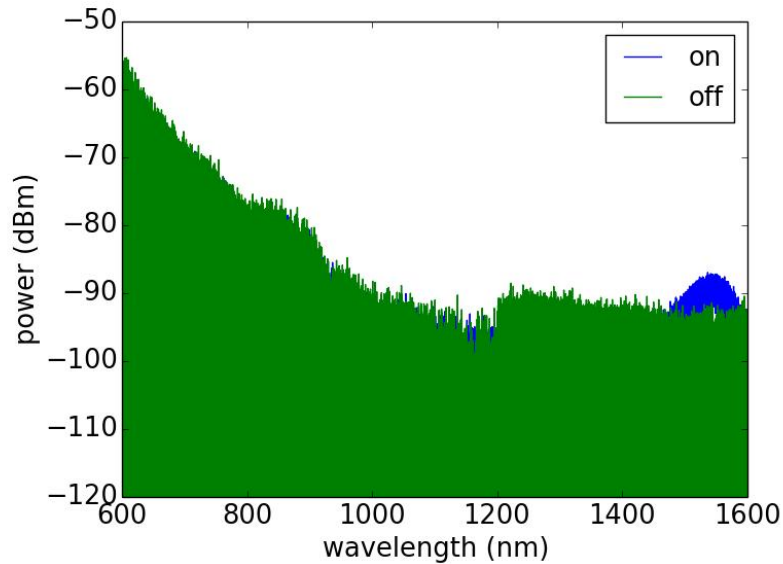

Figure 3.9: The full OSA trace of the optical emission from a p-substrate laser for growth with reduced doping. The noise level of the OSA is in the foreground for the current supply to the device turned off, with the biased output of the device visible at $1.55\mu m$.

plots (LIs) for all the growths, for FP cavities with ridge widths of $2.5\mu m$. The first growth LI shown in Figure 3.10 did not lase. The output optical power from the two updated growths reached the same power level after lasing, and this output power was comparable to a typical p-i-n laser.

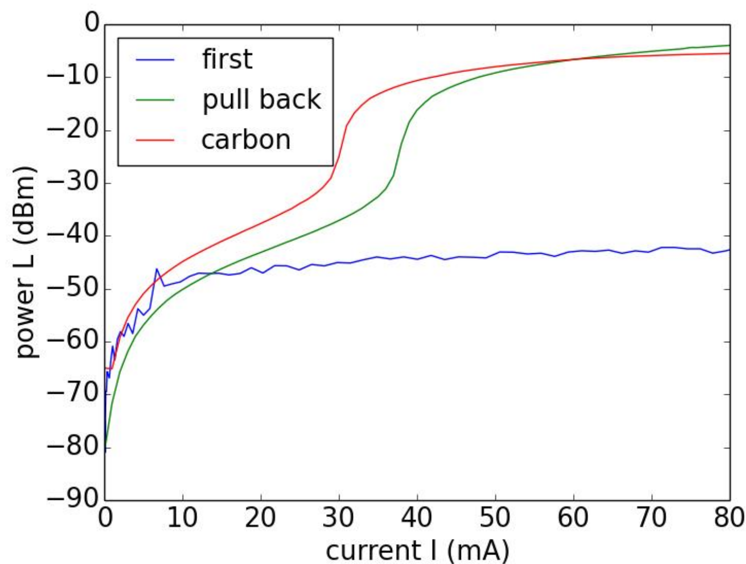

Figure 3.10: Comparison of the optical power vs. electrical current (L-I) plots of different n-i-p growths.

Figure 3.11 shows the optical output spectrum from the different growths recorded by an OSA. As mentioned previously, the first growth had the correct emission wavelength but very poor optical power, while the new growths maintained the centre wavelength of $1.55\mu m$ with higher optical output power. The different FP cavity modes are visible in the spectral results for the new growths.

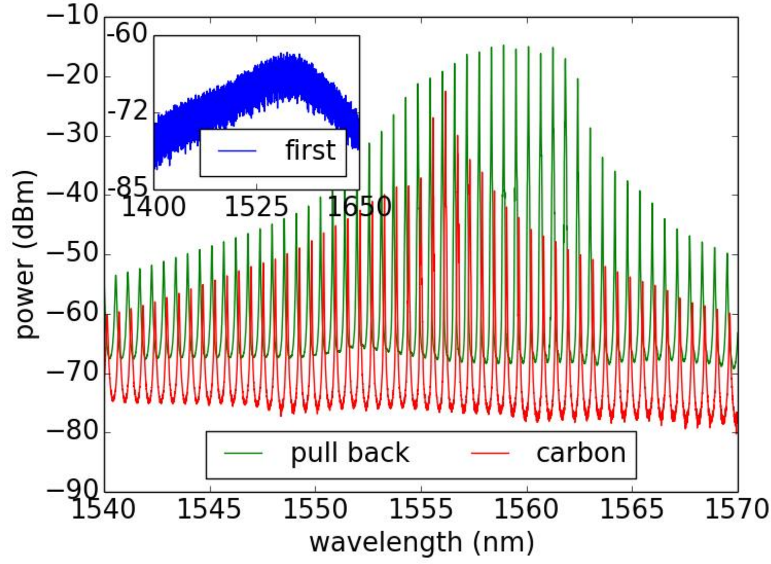

Figure 3.11: Comparison of OSA traces for spectra from different p-substrate laser growths.

The threshold currents of the two updated growths differed. The carbon blocking layer iteration had a lower current threshold than the pulled back doping, with a larger threshold bias voltage. This increase in bias intimated that there was an additional voltage drop over the carbon blocking layer that the electrical source had to overcome. Thus the application requirement will determine which growth is more suitable, carbon blocking would be preferable to minimise the current sourced while pulled back doping would be preferred to minimise potential.

The best determination may come from the power consumed by the lasers, for which the wall plug efficiency is the standard measure. The wall plug efficiency is given by the ratio of the power output to that input, and can be expressed by

$$\eta_{WP} = \frac{P_o}{P_i} = \frac{2\Delta L}{\Delta I \cdot V} \tag{3.2}$$

where the factor of 2 arises due to the two facets of the laser. The quantity $\frac{\Delta L}{\Delta I} = \frac{dL}{dI}$, the slope efficiency, is measurable from LI plots. Both types of laser exhibited the same behaviour, with the slope efficiency increasing with ridge width until $5\mu m$. Due to the carbon blocking iteration possessing a higher operating

voltage, its wall plug efficiency was lower than that of the pulled back doping iteration.

The behaviour of the current-voltage (IV) curve for both updated growths was the same, Figure 3.12, excepting this added voltage drop. The threshold current and the current density changed in the same way for both the updated growths. The threshold current increased with increasing ridgewidth, because current density decreases with increasing ridge width. The comparable behaviour indicates that the voltage drop introduced by the carbon is not dependent on any other factors than its layer composition itself.

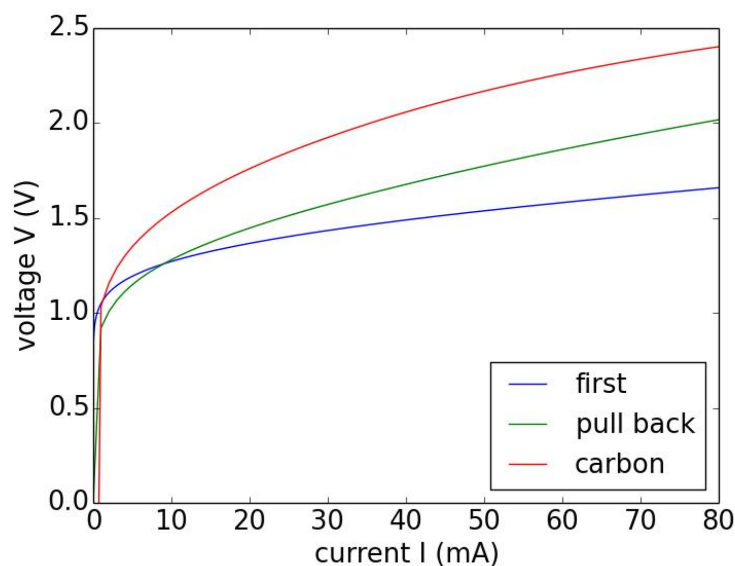

Figure 3.12: Comparison of the current-voltage (I-V) plots of different n-i-p growths.

The turn-on voltage of the p-substrate lasers can be seen in Figure 3.12 where the current begins to increase rapidly, and is higher than that of equivalent n-substrate lasers. For lasers emitting at $1.55\mu m$ the corresponding band-gap is $\frac{hc}{\lambda} = \frac{1.24eV\mu m}{1.55\mu m} = 0.8eV$, which is consistent with the usual turn-on voltage at which the junction bias is overcome. The turn on voltage of all these p-substrate growths was closer to $1V$, and it has already been shown in Figure 3.11 that the emission remained at $1.55\mu m$. Thus there was an increase in voltage for all growths, that must arise from the doping profiles, with a further voltage drop across the carbon doped layer, or from the metal contacts.

The slope of the IV curves was the same for the updated growths, and less for the first growth. SimWindows [216] was used to perform simulations for different doping concentrations and showed that $\frac{dV}{dI}$ decreases with increased doping

concentration. As the first growth had the smallest slope in Figure 3.12 it suggested that the doping was highest in this growth, as expected as the new growths reduced the doping further. This also indicated that the carbon doping, which was high in the SCH layer, does not contribute to the charge or p-doping of the material; it acts passively solely as a block.

The LIV and OSA traces of both the carbon blocking and pulled back doping iterations correlated closely. This was not surprising as the growths were the same, except for alterations in the p-doping. Thus both iterations successfully repressed excessive p-dopant diffusion during epitaxial growth, correcting the failures of the first growth. Either of the p-substrate laser designs can be used as the lower laser in the vertically integrated waveguides.

The different test mechanisms that allowed determination of the p-doping as responsible for laser failure, and suggested the new growth iterations, are discussed in the following sections.

3.3.2 Pulse Testing

Returning to the first failed laser growth, with reduced p-doping density, the devices were pulse tested in an effort to inject more carriers without overheating the device [219] and incurring carrier combination losses. A pulse measurement consists of a duty cycle of typically 0.1%, meaning that the signal is on for 0.1% of its period, with the resultant pulse width typically on the order of μs. High currents in excess of $100mA$ are possible, supplying an average current much less than this. A low duty cycle allows efficient operation of a device under test, so that it doesn't succumb to heating effects.

The spectrum of one of the pulse tested lasers is shown Figure 3.13. The pulse in this case had a duty cycle of 10%, which replicated steady state direct current (DC) biasing by injecting as much current as possible into the device. The high duty cycle simply increased the injected current, much the same as increasing the current in DC operation, but helped prevent the device from overheating and breaking.

Cavity modes were now visible from the pulsed spectrum, Figure 3.13a, of the first growth that was unsuccessful under DC operation. A Fourier Transform was performed on the spectrum to transform to the wavevector domain and from that the cavity length was calculated [164], Figure 3.13b. The modes correctly corresponded to the designed cavity length of $600\mu m$. The fact that the full cavity length was experienced by the light indicates that there were no abhorrent fabrication failures that placed unintended perturbations within the waveguides.

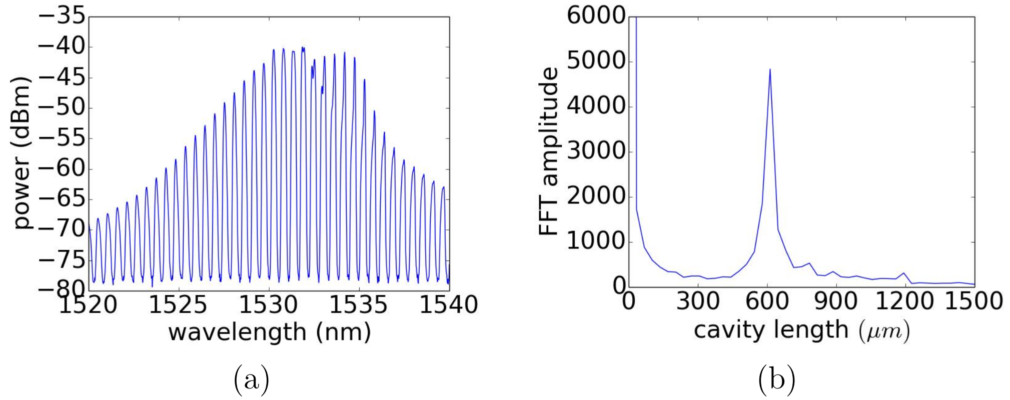

Figure 3.13: (a) OSA trace of the emission from a pulsed p-substrate laser for the first growth with reduced doping. The duty cycle of the current pulse was 10%, and gave rise to higher emission than DC biasing, with cavity modes visible. (b) An FFT converts the OSA trace to cavity lengths, with the resulting length of $600\mu m$ matching the designed cleave.

Further, Figure 3.14 displays SEM images of successfully fabricated waveguide ridges. The SEM images show full oxide openings on a ridge, which allowed metal to contact the semiconductor there, n-type InP in this case, but electrically isolated everywhere else. Also shown is metal coating up the sidewall of the ridge, supplying a contact from the probed pads to the oxide opening. These successful fabrication attributes were likewise visible in this fabrication, indicating that the fabrication was not responsible for the poor device performance, but rather it must be an epitaxial growth issue.

The pulsed current source hardware was restricted to minimum duty cycles of 0.1%, and any reflections in the electrical connections resulted in ringing of the pulse and the collapse of a proper pulse width. A pulsed voltage source is more resilient, and was used to produce the LI curves in Figure 3.15 [219]. The threshold current was a very large $150mA$, larger than a typical p-i-n InP-based laser would be. This correlated with the LI measurements and showed the material wasn't functioning properly.

A measurement of device performance is the external quantum efficiency, which gives the ratio of the number of photons emitted per carriers injected, and is expressed by

$$\eta = \frac{\frac{L}{h\nu}}{\frac{I}{q}} = \left(\frac{L}{I}\right)\frac{q\lambda}{hc} \tag{3.3}$$

where L is the optical power, I is the current, ν is the frequency and λ the wavelength, q is the electron charge and h is Planck's constant. It can be seen from this Eq. 3.3 that the slope of the LI curve provides a measurement for the

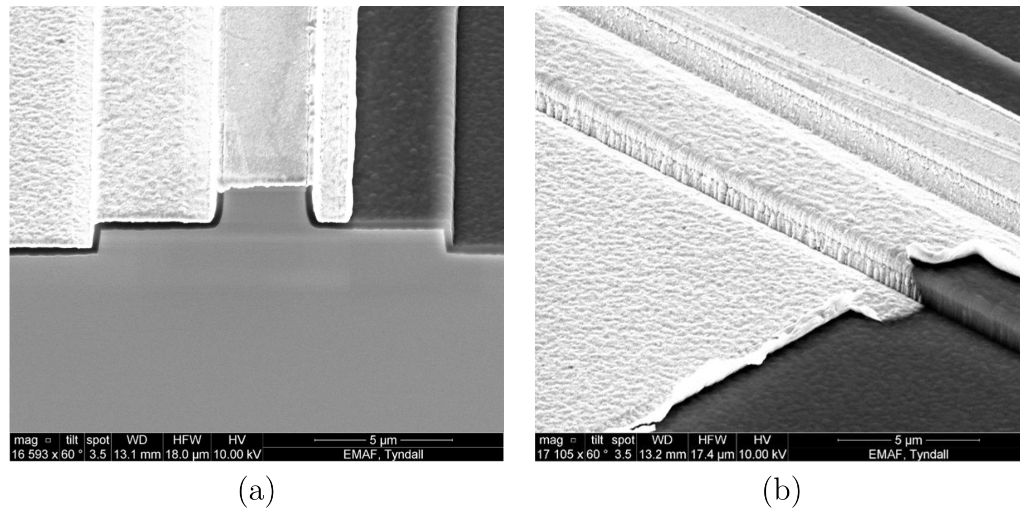

Figure 3.14: SEM image examples of successful metal contacts on an FP ridge. (a) An oxide opening at the top of the ridge is visible by the lack of a dark line as seen at all other locations. (b) Metal contact flows up the sidewall of the ridge, allowing electrical current to flow between a pad and the exposed semiconductor at the ridge summit.

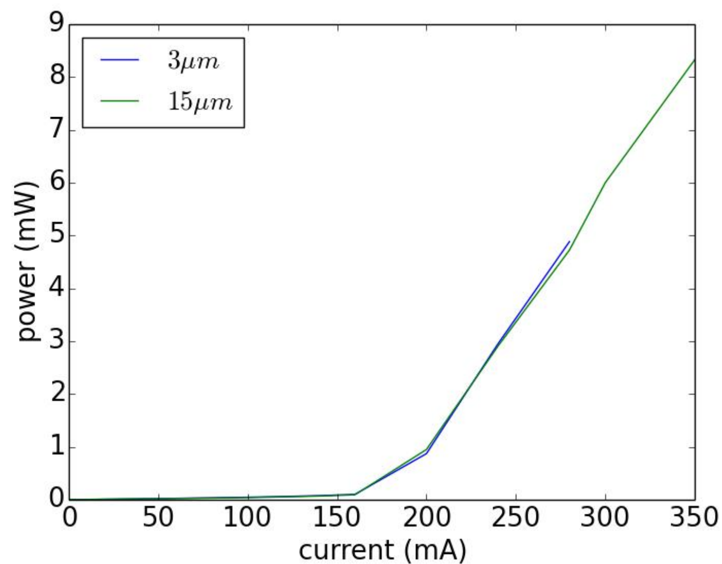

Figure 3.15: LI plot of first growth n-i-p lasers, with reduced doping, for different ridge widths. The duty cycle of the voltage pulse was 0.1%.

external quantum efficiency. For these pulsed lasers the quantum efficiency was a lowly 6%. This compares to 20% for a typical n-substrate InP laser, yet again inferring that the laser material was not correct.

The behaviour of the pulsed lasing matched for different ridge widths as evident in Figure 3.15. The matching behaviour of the ridge widths indicated that there were no carrier confinement issues. As mentioned at the start of this chapter, n-carriers have higher mobility than p-carriers. By placing n-carriers at the top of the epitaxial layers there was a fear that when devices were fabricated with shallow etches, stopping above the QW core, then the n-carriers could be susceptible to current spreading laterally across the device rather than vertically through the intrinsic region [220]. This was later overcome by a deep etch through the QWs to ensure confinement.

In this shallow-etch fabrication the different ridge widths should have indicated current spreading. If the current spreaded strongly, then narrower ridges would have been unable to confine the current vertically. However, wide ridges, such as the $15\mu m$ ridge included on the material test mask, cover such a large area that the current must have been somewhat confined within it. Thus, in the case of strong lateral current-spreading wide ridges should still have lased while narrow ridges would not. As this behaviour was not seen, it was concluded that the ridge etch satisfactorily confined the carriers, and the weak emission was due to poor optical efficiency in the QWs.

As will be discussed in Section 4.2 the full up-down structure process features only deep etches, through the waveguide core regions. Thus, the carrier's confinement becomes inherent. The updated n-i-p laser growths were therefore fabricated with deep etches as outlined in Section 3.2.1.

3.3.3 CV Measurements

The large area diodes included on the material test mask allowed robust IVs to be measured, along with capacitance-voltage (CV) measurements. The CV measurements allowed the extraction of the intrinsic thickness of the junction through the relationship

$$C = \frac{\epsilon A}{W} \tag{3.4}$$

where A is the area of the diode and W is the depletion width.

The capacitance of a semiconductor junction can be expressed by [221]

$$C = A\sqrt{\frac{\epsilon q}{2\left(V_{bi} + V_R\right)} \frac{N_D N_A}{N_D + N_A}} \tag{3.5}$$

where N_D and N_A are the n-donor and p-acceptor concentrations respectively, V_{bi} is the built in voltage of the semiconductor junction, and V_R is the reverse bias applied. This expression can be compared to that of Eq. 3.4 to give an expression for the intrinsic thickness as a function of applied voltage.

The predicted depletion width of the laser material as a function of bias is shown in Figure 3.16 for different p-doping concentrations. The intrinsic thickness reduces as the doping concentration increases, as the dopants penetrate further into the intrinsic region before cancelling each other's charge. The intersection of the curve with the x-axis denotes the built-in voltage of the junction. The depletion width changes more slowly with bias for increased doping.

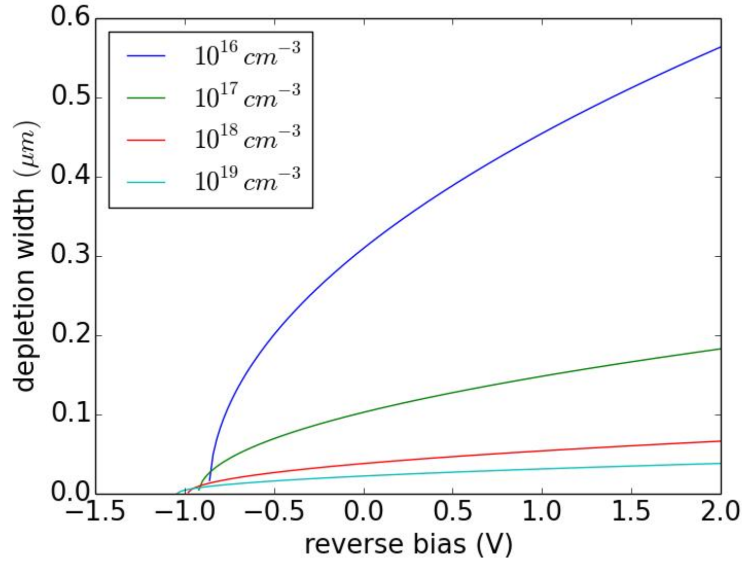

Figure 3.16: Theoretical plot of the depletion width vs. reverse bias for different p-doping concentrations, when the n-concentration is held constant.

The different components of the capacitance can be separated by writing the overall capacitance as the sum of contributions from the bulk and peripheral capacitances, C_B and C_P respectively, that is through the diode area A and the diode perimeter P,

$$\begin{aligned} C &= AC_B + PC_P \\ \Rightarrow \frac{C}{A} &= C_B + \frac{P}{A}C_P \end{aligned} \tag{3.6}$$

By measuring a number of different area diodes, such as in Figure 3.17a, a plot of $\frac{C}{A}$ vs. $\frac{P}{A}$ was made so that the slope and intercept of a linear fit supplied the peripheral and bulk components of the capacitance respectively.

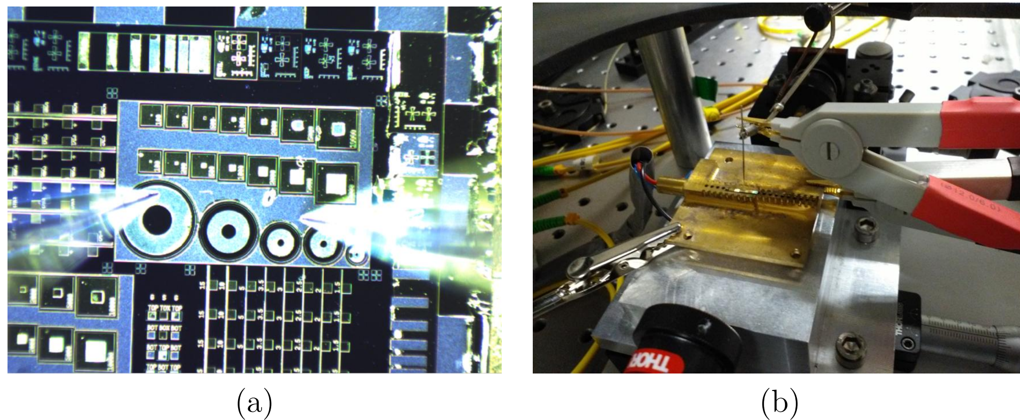

(a) (b)

Figure 3.17: CV measurements performed on laser diode devices. (a) A probe needle contacts the large area photodiode contact. (b) The devices are on a brass chuck for electrical contact. Standard DC probes can be used to contact the device due to the low frequency measurement. An LCR Bridge's measurement clips can simply be attached to the probe arms.

In order to correctly measure the capacitance of the material the measurement tools must operate in the correct regime. The theoretical formulas Eqs. 3.4 and 3.5 place the capacitance of a semiconductor junction between $100pF$ and $1nF$. Measurement accuracy charts state that such capacitance values are measurable using low frequencies. A frequency scan between $20Hz$ and $300kHz$ of the capacitance was performed on the large area photodiodes, and it was found that the results converge for frequencies above $100kHz$.

An LCR Bridge measured the capacitance of the device under test by injecting a current into the device and comparing the current throughput and the potential across the device. Figure 3.17b displays a functioning CV measurement set-up. The LCR Bridge's outputs were tested with RF cables, and due to the low frequencies were found to match exactly those measurements performed with DC probes. This simplified the CV measurement considerably. Shorted and open calibrations were first performed for the LCR Bridge before connecting to the diode.

The depletion width versus bias for the n-i-p laser growths are shown in Figure 3.18. The first failed growth had the lowest depletion width. This matched the theory that the p-dopants diffused into the QWs and closed the intrinsic region, leading to a reduction in optical efficiency. The pulled-back doping created an intrinsic region of sufficient thickness to allow efficient optical emission, while the carbon doped iteration surprisingly had the largest depletion width. This highlighted that the carbon doping, which was high concentration in the SCH layer, did not contribute to the charge of the material, it acted passively and

solely as a diffusion blocker.

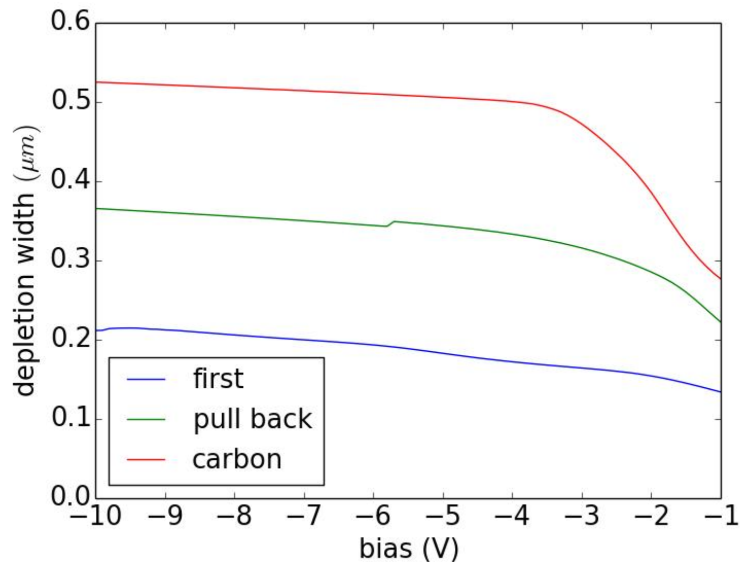

Figure 3.18: Comparison of depletion width vs. bias for different n-i-p growths, as extracted from CV measurements.

The depletion width of all the growths levelled off below $-4V$, but before this the slopes of the width versus bias curves differed. The carbon blocking layer had the greatest depletion width, and with it the highest slope leading up to this, which indicated the lowest doping concentration, as predicted in Figure 3.16. Low doping and large depletion width are equivalent in the view of p-dopant diffusion.

For the successful p-substrate lasers, the value of the capacitance was the same for different area diodes. This indicated that the peripheral component of the capacitance was negligible for the devices, Eq. 3.6. Devices that do differ in capacitance depending on area must have a non-negligible peripheral component. A low peripheral capacitance component is indicative of clean fabrication.

3.3.4 ECVP and SIMS

The material growth itself was validated using an electrochemical capacitance-voltage profile (ECVP) [222]. For an ECVP, a voltage is placed across the sample and capacitance measurements are performed as the material is etched-away. The material's atoms are attracted to electrodes differently depending on their charge and this allows a profile of the dopants in the sample to be measured. The drawback to ECVP is that it is destructive to the sample.

Figure 3.19 displays the ECVP of the n-i-p laser. Visible is the n-doping in blue, which followed the profile pattern designed in Figure 3.2 with the correct

doping concentration values. While the spatial recordings of the profile do not match that designed, it does not mean it is incorrect. The ECVP spatial component was transformed from the expected etch rate, but if the etch rate changed or differed then the transformation could be incorrect. Thus, only the pattern and magnitude of the doping profile could be relied upon.

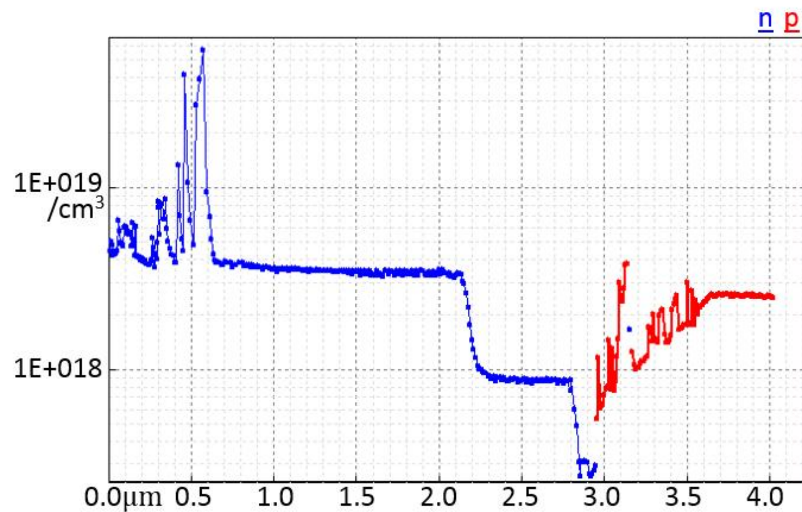

Figure 3.19: ECVP of first p-substrate laser growth with reduced doping, with the negative n-dopants in blue and the positive p-dopants in red.

The n-doping reduced to null in the intrinsic core region. The red trace line then outlined the p-doping profile, but it was erratic. The failure for a precise p-doping profile arose from the increase in errors as the etch depth increased, and at the point the p-dopants begin the depth was nearly $2\mu m$. With the n-doping profile reliably measured, a second sample was used for another ECVP measurement. The majority of the n-layers were first etched away to allow a more precise measurement. However, the etch was too deep and the ECVP immediately began with p-doping recordings, indicating greater than expected p-dopants.

Secondary Ion Mass Spectrometry (SIMS) is the most sensitive of all surface analytical techniques [223, 224]. It is credited with being able to detect as low as <1ppm concentrations. Like ECVP it is a destructive technique, and it costs considerably more [225]. In a SIMS measurement, a high energy ion beam bombards the sample and causes the ejection of secondary ions from the surface. The ejected ions are analysed with a mass spectrometer. SIMS measurements were carried out on the successful updated growths, and the resulting compositional profiles are shown in Figure 3.20.

The carbon blocking layer can be seen rigidly defined in Figure 3.20 for the carbon blocking layer iteration, while non-existent for the pull-back doping it-

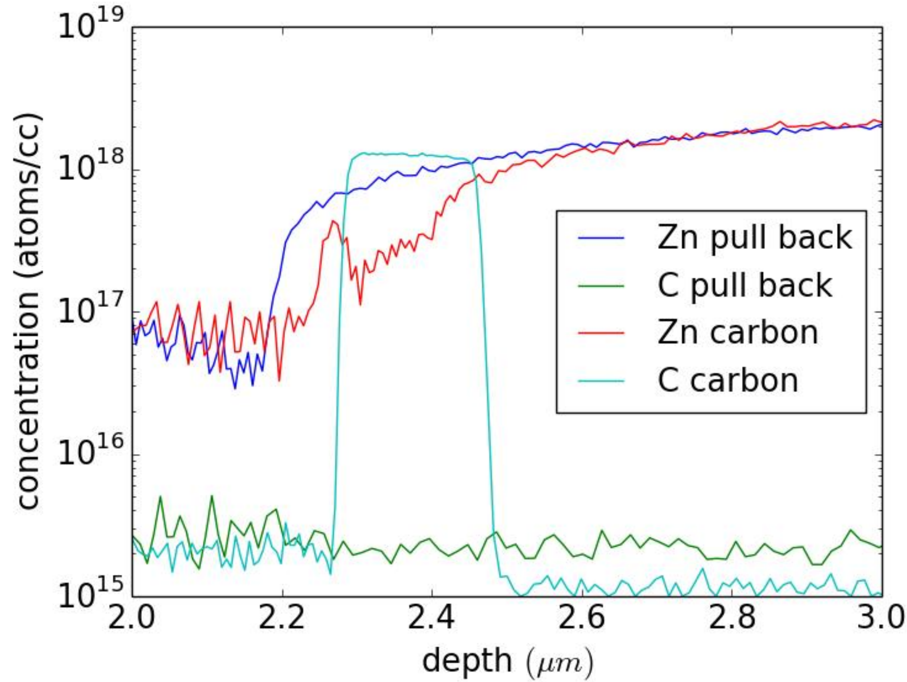

Figure 3.20: SIMS of successful n-i-p growths, indicating the Zn and C doping concentrations with depth for both the doping pull back and carbon blocking layer growth iterations.

eration. Comparing the Zn concentration profile between growths, the carbon blocking iteration reduced slightly more quickly than the pull-back doping iteration. This matched the results from the previous Sections 3.3.1 to 3.3.3, where the behaviour of both growths was similar but with minor differences arising from the slightly larger depletion width of the carbon doped iteration.

Figure 3.21 combines the experimentally obtained depletion widths from CV measurements and SIMS measurements with the designed doping profiles. Each measurement can be viewed in isolation in Figures 3.2, 3.18 and 3.20. The vertical dotted lines in the combined Figure 3.21 indicate the depletion width extracted from the CV measurements at $-1V$. The n-doping profile was taken to be precise, as was indicated by the ECVP, and so the depletion width changes were taken to occur on the p-side only.

Figure 3.21 shows that the first growth's diffusion closed the intrinsic region into the QWs, explaining the lasing failure. The pulled back doping resulted in a depletion width as originally desired, while the carbon blocking layer maintained a larger depletion width, holding the dopants back beyond the start of the SCH layers.

The SIMS measurements have been aligned with the intrinsic region in Figure

3.21. The overlayed SIMS measurements show that the difference in doping profile between the pulled back doping and carbon blocking layer growth iterations is the same as the difference obtained from the CV measurements.

The correlation between the different measurement techniques helps validate each measurement. The CV measurements prove their worth by providing the depletion width using a much quicker and cheaper experimental procedure than SIMS.

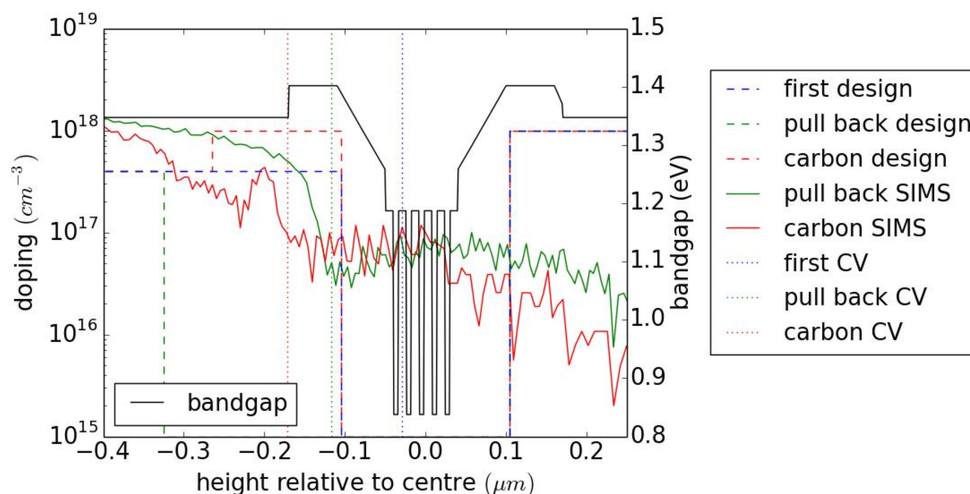

Figure 3.21: The bandgap design of the n-i-p lasers, overlayed with the designed doping profiles. The SIMS measurements are also overlayed, and the vertical dotted lines indicate the depletion width calculated from CV measurements.

3.4 Discussion and Conclusions

P-substrate InP-AlGaInAs lasers have been developed, for use in further monolithic vertical photonic integration. The laser material was characterised with LI measurements, both DC and pulsed, to obtain optical properties, with IV, CV, ECVP and SIMS measurements revealing carrier properties.

Zn dopant diffusion has been proven to narrow the depletion width of the laser diodes and thus ruin optical efficiency by altering the gain core's QWs. As Zn is the dominant p-dopant for InP p-substrates, it cannot be removed from the epitaxial structure so needed to be adapted.

The Zn p-dopant diffusion was overcome by two techniques. In the first the Zn p-doping profile was pulled back from the QW core, leaving a larger undoped InP region before the SCH layers. This pulled back doping allowed Zn dopants to diffuse safely during long growths, settling at their designed position in the case of no diffusion.

The second method carbon dopes the lowermost SCH layer, creating a dopant blocking layer. This carbon doped layer acted with neutral charge, and was found to restrict dopant diffusion most effectively.

The carbon doped blocking layer n-i-p laser maintained the largest depletion width, as measured via CV measurements, and its inclusion introduced a voltage drop across the device. The pulled back doping n-i-p laser also maintained a depletion width large enough to allow lasing characteristics equivalent to n-substrate InP lasers.

Either of the two updated p-substrate laser iterations in this Chapter suggest themselves for use in a full vertically stacked passive waveguide above a laser, as will now be discussed in the next Chapter 4.

Chapter 4

Up-Down Waveguide Device Design and Testing

Chapter 2 dealt with the design of a vertical coupler between an upper passive waveguide and a lower active waveguide. The optimum practical taper shape was found to be linear, with the main vertical transition taking place between upper ridge widths of $0.7\mu m$ and $0.4\mu m$.

Chapter 3 investigated the lower active waveguide, overcoming inherent growth difficulties to create a functioning p-substrate laser equivalent to standard n-substrate InP-based lasers. A p-substrate is required due to the stacking of intrinsic regions for each waveguide, so that the full structure has a p-i-n-i-p configuration.

This Chapter now combines the experience of the previous chapters. The upper passive waveguide was built above the lower laser made in Chapter 3, fabricated to the specifications of the vertical coupling taper designs of Chapter 2.

Test devices were designed with a new stacked waveguide process to supply experimental validation of the predicted waveguiding. Vertical mode transitions were proven to occur.

4.1 Epitaxial Growth

Table 3.1 displayed the updated realisitic p-substrate laser epitaxial layer structures in Chapter 3, upon which the upper waveguide layers were grown. Table 2.1 displayed the refractive index structure of a vertically coupling stacked waveguide structure in Chapter 2. The actual AlGaInAs compounds with the required refractive indexes were previously found in Table 2.2 and used now in the epitaxial

growth. Table 4.1 shows the resulting grown epitaxial layers for the full up-down structure.

Table 4.1: Full as-grown epitaxial layer design of the up-down WG. The active waveguide consists of 5 QWs at the bottom, with the upper WG being replaced by a thick bulk core at the top. In the middle is the additional passive WG solely to increase vertical coupling. The carbon blocking layer and pull-back doping iterations are both shown on the table with different layers (a) and (b) respectively. The carbon growth (a) does not require a layer #5.

	Layer #	Layer	Material	PL nm	Thick nm	Doping cm^{-3}	Type
Passive	24	P contact	InGaAs		20	$5 \cdot 10^{18}$	Zn+C
	23	P contact	InGaAs		80	$1 \cdot 10^{19}$	Zn
	22	P cladding	InP		1000	$5 \cdot 10^{17}$	Zn
	21	CIL	InGaAs		2		
	20	SCH	AlInGaAs	940	250	NUD	
	19	Core	AlGaInAs	1400	447	NUD	
	18	SCH	AlInGaAs	940	50	NUD	
Transition	17	N cladding	InP		200	$5 \cdot 10^{17}$	Si
	16	N cladding	InP		300	$1 \cdot 10^{18}$	Si
	15	CIL	InGaAs		2		Si
	14	Transition	AlGaInAs	1100	250	$1 \cdot 10^{18}$	Si
	13	N cladding	InP		250	$3 \cdot 10^{18}$	Si
	12	CIL	InGaAs		2		Si
Active	11	SCH	AlGaInAs	937	10	$1 \cdot 10^{18}$	Si
	10	SCH	AlGaInAs	913	60	$1 \cdot 10^{18}$	Si
	9	SCH	AlGaInAs	1030	60	NUD	
	8	Barrier	AlGaInAs	1100	10	NUD	
	7 (×5)	Well	AlGaInAs	1530	6	NUD	
	6 (×5)	Barrier	AlGaInAs	1100	10	NUD	
	5b	SCH	AlGaInAs	1030	60	NUD	
	4b	SCH	AlGaInAs	913	60	NUD	
	3b	P cladding	InP		160	NUD	
	2b	P cladding	InP		340	$4 \cdot 10^{17}$	Zn
	4a	SCH	AlGaInAs	1030	120	NUD	
	3a	SCH	AlGaInAs	880	160	$1 \cdot 10^{18}$	C
	2a	P cladding	InP		400	$4 \cdot 10^{17}$	Zn
	1	P+ cladding	InP		1000	$> 1.5 \cdot 10^{18}$	Zn
	Substrate	P Wafer	InP				Zn

At the bottom were the laser layers, and both pull back doping and the carbon blocking layers are shown in Table 4.1 and were grown onto p-InP wafers. 5 QWs with room temperature emission centred at $1550nm$ were grown above the p-doped layers.

N-doped layers were grown above the QWs to provide n-contact layers for

metal contacts. The n-contact metal completes the circuit for both the lower waveguide and upper waveguide.

The n-doped layers make up the barrier region, stretching across a thickness of $1\mu m$ to provide isolation of the upper passive mode from the lower absorbing active waveguide core. These layers were mostly InP, but in the middle of the InP barrier layers was an AlGaInAs layer with a thickness of $250nm$. This was the new, additional intermediate passive waveguide determined in Chapter 2.3.2, used solely to aid the vertical transition over the long barrier.

The upper waveguide core was placed above the n-doped barrier. The upper waveguide was grown initially as a single thick bulk layer with a thickness of $450nm$, rather than as a full QW containing modulator material. The AlGaInAs compound used had the same average refractive index and thickness of a proper MZM material with QWs.

Topping the structure were more p-doped layers to provide metal contact to finish the upper waveguide circuit. Highly doped InGaAs p-contact layers were the final layers in the structure. These layers were absorptive and could not be placed in the barrier region, a deciding factor resulting in the final p-i-n-i-p configuration. Instead of the p-InP substrate, a semi insulating substrate could have been used with highly doped contact layers grown onto it to provide for a p-contact. The InP layers between the QW core and these contact layers would have needed to be approximately $1\mu m$ thick to prevent the lower waveguide mode from overlapping into the absorptive layers and experiencing high loss.

X-ray diffraction (XRD) measurements were performed on the grown sample to quantify the quality of the lattice matching in the crystal. XRD measurments were made by rotating the wafer while impinging x-rays upon it. The diffracted light was recorded by a detector and the different angles support higher or lower magnitude diffraction depending on the epitaxial layer structure.

Photoluminescence (PL) measurements were also performed on the sample to reveal its emission wavelengths. In a PL measurement the wafer is excited by light of a lower wavelength (higher frequency and energy), which then causes emission from the wafer itself, revealing the band-gap energies [158, 226].

Figure 4.1 and Figure 4.2 show the XRD and PL data of the upper waveguide and lower laser material respectively.

In both the XRD data in Figures 4.1 and 4.2 the largest peak was centred within the central angle regions. This indicated good lattice matching to the substrate; the structure acted as a single block of crystal because the layers aligned. For the upper waveguide in Figure 4.1 the peak was a little to the

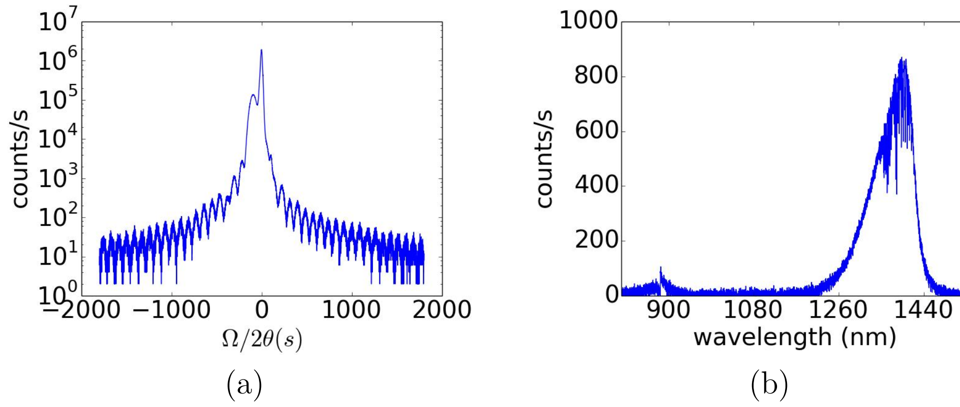

Figure 4.1: Calibration results for the upper passive material with (a) XRD data, showing the lattice mismatch is tolerable, and (b) PL data showing that the overall emission is 1390nm, close to the 1400nm requested.

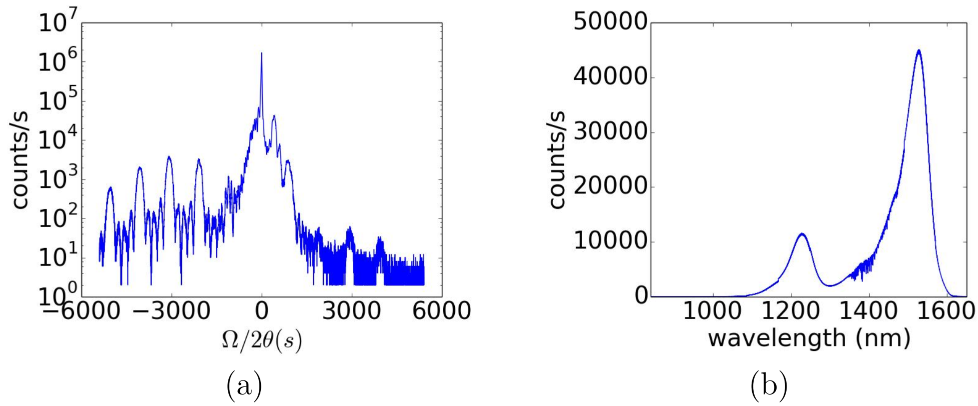

Figure 4.2: Calibration results for the lower laser material with (a) XRD data, showing QW peaks and that the lattice mismatch is tolerable, and (b) PL data showing that the overall emission is 1530nm as designed.

side, indicating a slight mismatch, but of a tolerable amount. For the lower waveguide, Figure 4.2 shows multiple peaks for the central angles, which displays the additional SCH layers in the laser. To the far left for the laser material in Figure 4.2 there are multiple peaks, and these were the result of the QWs. The QWs were created by periodic layers, which formed a grating for the XRD measurement, supporting high magnitude diffraction at multiple angles.

The PL data from Figure 4.2 shows the laser material had an emission peak at 1530nm as requested in the growth table. A secondary peak at 1200nm is evident too, which must have resulted from the SCH layers.

The emission from the upper waveguide in Figure 4.1 was 1390nm. The requested PL of the AlGaInAs layer was 1400nm, which possesses the required refractive index in the waveguiding simulations. However, the value of 1390nm was not too dissimilar and was deemed acceptable.

4.2 Process Design

4.2.1 Fabrication Tolerance Simulations

The waveguiding analysis in Chapter 2 predicted the dimensions required to achieve high vertical coupling between the upper and lower waveguides. In practice, achieving these dimensions can be challenging to fabricate using the tools available.

The key constraint was the submicron taper tips of $0.7\mu m$ and $0.4\mu m$. As seen in the BPM simulations and mode slice solutions, if the upper waveguide ridge width is as small as $0.4\mu m$ the mode will no longer reside in the upper waveguide, so the vertical transition will be complete. This means that the taper tip can be any width less than $0.4\mu m$, which could be thought to relax the fabrication tolerance. However, below $0.4\mu m$ the definition of lithographic patterning becomes unrefined. At such low dimensions the sidewalls of the ridge can become undulating which might affect the mode propagation by causing radiation out the sidewalls. As long as a width of $0.4\mu m$ can be achieved, any undulations or sidewall roughness thereafter do not matter. E-beam etching can be used instead of wet-etching to achieve more precise dimensions, which should allow the low submicron features to be achieved.

It was not wise to attempt a long taper from the standard ridge width of $2.5\mu m$ to the transition start of $0.7\mu m$. As already mentioned in Section 2.3.2 the size of the PIC overall will become unmanageably large if a slow taper slope is maintained for such a large change in width. Instead, a quick taper from $2.5\mu m$ to the transition region was used, where the losses remain negligible for taper lengths even lower than $50\mu m$ in this high overlap region.

Rather than tapering directly to where the coupling begins at $0.7\mu m$, fabricators determined it was safer to taper to above $1\mu m$ first, a width that could confidently be achieved. A ridge width value of $1.1\mu m$ was already used in the BPM simulations of Section 2.3.2 to accommodate for the fabrication tolerance $\pm 0.2\mu m$. A taper with a slope of $\frac{1}{2000}\mu m$ per μm was found to achieve a large vertical transition from this width, and thus was used in the device designs. A ridge width of $1.1\mu m$ ensures that the quick taper ceases above the transition point even in the most over-exposed fabrication case, and the slow adiabatic taper can cover the remainder of the transition.

The challenging fabrication to achieve submicron features was achieved by precise alignment in the plane of the taper width, perpendicular to the propagation direction. There were no other features that required such precision, so the

alignment only needed to be highly accurate in that single direction.

The ridge width considerations above are crucial for waveguiding, with the transitions achieved only through lateral tapers. But the etch depth also determines the confinement of the mode in the waveguides, as seen in Section 2.2.3.

The etch rate can be difficult to control precisely, as different material layers will etch at different rates. Figure 4.3 plots the full up-down-up BPM simulation results for etch depths around the optimum etch depth of $2.1\mu m$ that achieves the optimum mode solutions. From the simulations it can be seen that the transmission has a bit of tolerance to the etch depth, but etching beyond an extra 100nm decreases the throughput rapidly.

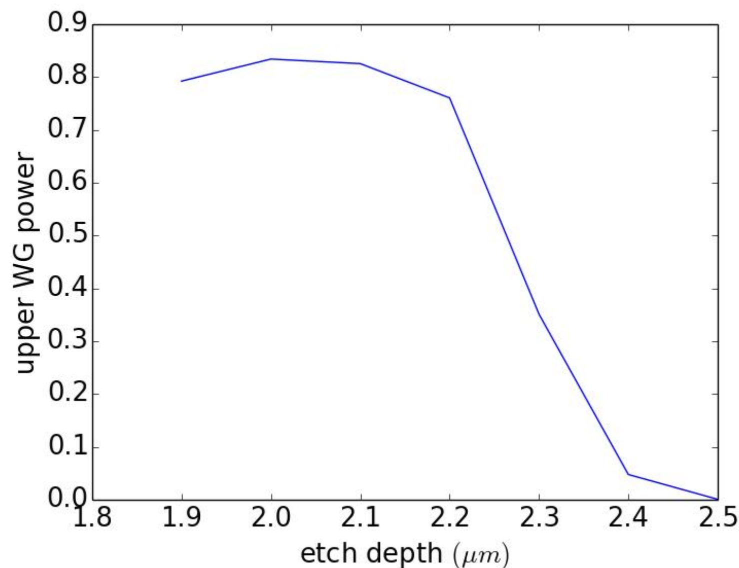

Figure 4.3: The power in the upper WG at the end of BPM simulations along the up-down WG structure for different upper etch depths.

To attain an accurate etch depth, an etch depth monitor measurement was performed on a segment of the material. Like the ECVP and SIMS measurements from Section 3.3.4, an etch monitor is a destructive test, so can ideally be performed on the leftover pieces after fabricating the $1cm^2$ material test mask outlined in Section 3.2.2.

Figure 4.4 shows the predicted etch depth monitor using software, alongside the measured results. The etch depth monitor was performed with a laser of wavelength $980nm$. The scales of the prediction and measurement differ, simply due to the measurement technique. The time of etching was recorded rather than the depth, because the exact depth wasn't measurable in real time. The recorded signal from the reflected laser light was also not normalised to supply

the reflectance that was modelled with the simulation. The refractive index, which mirrors the band-gap of the structure, was overlayed on the predicted etch monitor in Figure 4.4a. Dashed vertical lines are included within Figures 4.4a and 4.4b to highlight the beginning of the different core widths; the passive, intermediate transition and active. The predicted and measured results can be seen to match behaviour precisely, illustrating the accuracy of the theoretical model. The correct depth can be reached by monitoring the etch and ceasing after the correct number of periods. This allowed the critical etch depth of $2.1\mu m$ to be achieved for the upper etch.

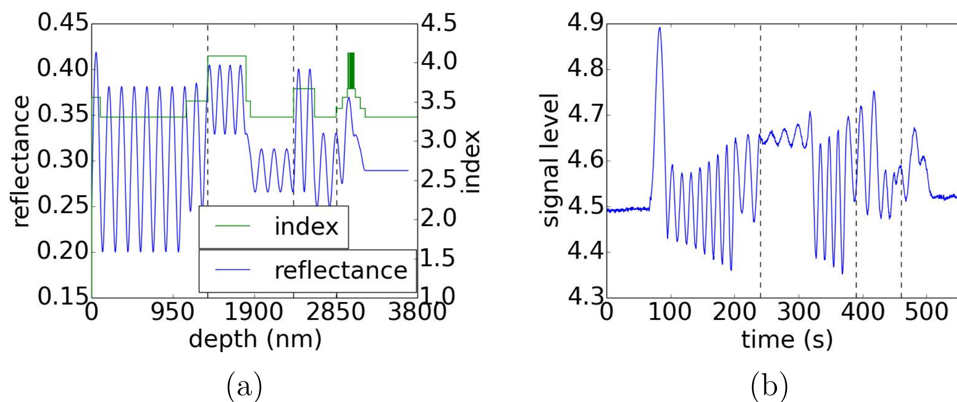

Figure 4.4: Etch depth monitor showing (a) the predicted result overlayed with the refractive index profile, and (b) the measurement, which correlates closely. The vertical dashed lines indicate the beginning of the passive core, transition layer, and active core, and highlight the similarity of the prediction and measurement. The etch depth monitor can be used to achieve accurate etch depths.

As well as the fabrication challenges, there may also be variations in the growth which either result in thicker or narrower layers. Any growth error would lead to etch depth errors, as the etches have to assume a perfect growth, and as seen in Figure 4.3 the etch depth is critical to the vertical mode coupling. Growth variations can be overcome using the etch monitor, which shows how effective a method it is. The growth in the case of Figure 4.4 was correct, as the monitor matches the theoretical curve. If the growth was incorrect then the correct layer could still be reached, as the monitor period would have varied according to the actual growth.

Variations in the growth would still affect the waveguiding. The barrier may not have been thick enough to isolate the upper waveguide mode from the absorbing lower waveguide, or it may have been too thick for even the additional intermediate waveguide to fully aid the transition.

Figure 4.5 shows BPM simulations through an up-down-up transition for vary-

ing barrier thicknesses. The thickness was altered between the lower waveguide and intermediate waveguide, recording the overlap with the ideal end mode. The more effective the taper transition is, the higher the overlap with the ideal end mode. It can be seen from Figure 4.5 that the taper transition is actually quite resilient to increases in the barrier thickness, so that even with an additional 150nm the transmission is not obliterated. Thus it is safe to increase the barrier thickness, and realistically the growth will not increase in thickness as much as simulated in Figure 4.5.

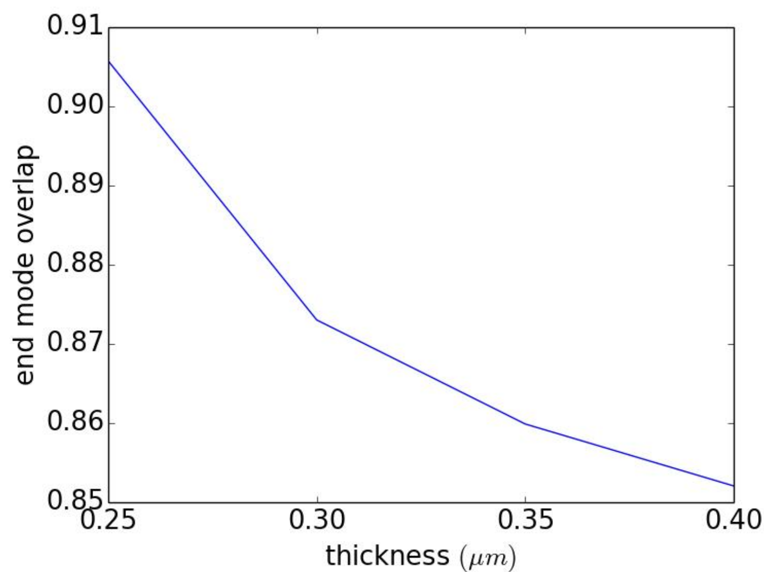

Figure 4.5: Overlap with the ideal end mode at the end of BPM simulations of the up-down-up transition through the stacked WG structure, for different thicknesses of InP above the lower WG.

4.2.2 Fabrication Design

The new vertically integrated waveguides required a new fabrication process. The aim of monolithic integration is to reduce cost by minimising fabrication complexity, and so the number of steps should be minimised [50, 93, 169].

In Chapter 3 the single waveguide ridge of the FP lasers could either be fabricated with a single deep etch through the QW core, or with a shallow etch to the top of the QWs. To achieve all top-side contacts to both n- and p-type semiconductor, a deep etch is required to reach the substrate material. In the case of a shallow etch for the ridge, the deep etch is a second etch step, while in the case of an existing deep etch no additional etch is required.

The upper waveguide in the vertically stacked structure required all top-side

contacts because it did not possess a backside. The n-contact lay in the barrier layers for both stacked waveguides. Thus, to minimise fabrication steps the upper waveguide was defined by a single deep etch. It may also be advantageous to have all top-side contacts for the lower waveguide, for future cases where the substrate may be insulating. Thus, the lower waveguide was also defined by a single deep etch.

It is a concern that deep etched waveguides will increase mode losses due to optical leakage out the sidewalls of the ridge. Conversely there is a higher index contrast across the ridge, as the semiconductor material is completely removed from the side of the ridge, unlike in the shallow etch case where some semiconductor material remains. The higher index contrast results in a greater mode confinement. Deep etched lower active waveguides were found to lase in Chapter 3, and ridgewidths of $2.5\mu m$, as designed for the structure, were found to be viable. These previous measurements indicated that the material should also lase in the full stacked structure.

Each ridge etch must be accompanied by an oxide opening step and a metal lift-off step, to create an electrical contact to the semiconductor in the ridge. Thus, for both waveguides combined, there were a minimum of 6 mask steps. Top-side metal contacts away from the ridge also require oxide openings and metal lift-off. However, these contacts were achieved with the same step as the ridge definitions.

The upper waveguide oxide opening and metal contact were performed independently because it was the highest layer. The base of the upper waveguide and the top of the lower waveguide shared the same layer, because they were defined by the same etch, and so their metal contacts were completed simultaneously. The lower waveguide's bottom p-contact then remained. In this growth iteration the lower waveguide was grown upon a p-InP wafer and so possessed a backside. The topside p-contacts were superfluous and their definition was not of primary importance. Thus the lower waveguide p-contact was performed at the same time as the n-contact, and while there could have been an error in definition arising from the different depths of the layers, the contact pad was of such a large width that it should have been defined satisfactorily regardless of accuracy.

The complete fabrication steps are outlined below, and the below colour chart indicates the relevant materials. The diagrams are in 3D to illustrate both the upper and lower waveguide ridges and transitions between them, but are not to scale.

Lower InP	Lower core	SiO_2	Photoresist
Upper InP	Upper core	SiN_x	Metal

i) The p-i-n-i-p wafer was grown to the specifications of Table 4.1.

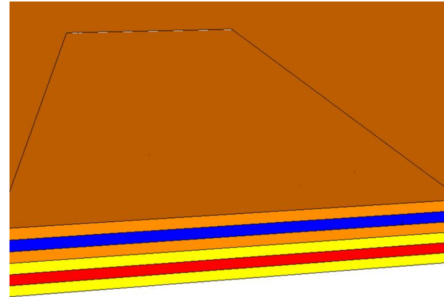

ii) The wafer was first covered by silicon dioxide.

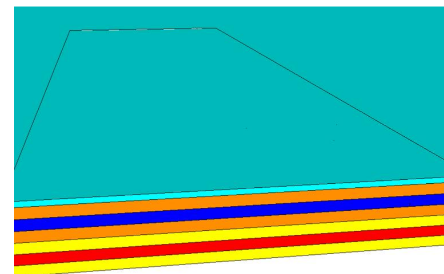

iii) Then the wafer was covered with photoresist.

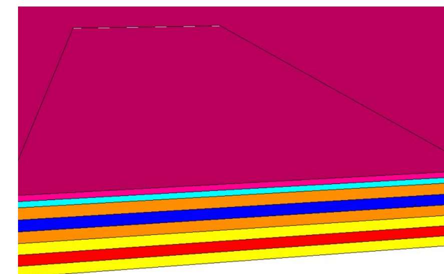

iv) The first mask step was used to pattern the photoresist and define where the upper ridge would eventually be.

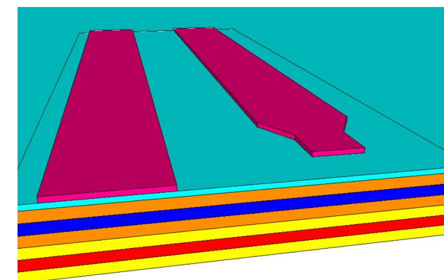

v) The uncovered silicon dioxide was then etched away to expose the semiconductor beneath.

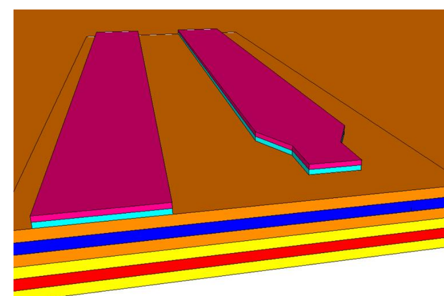

vi) The photoresist was removed before the next steps.

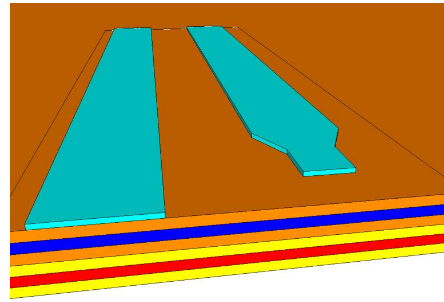

vii) To align the lower waveguide correctly with the upper waveguide, the oxide was left in place and the entire wafer was coated in silicon nitride. This was a self-aligning technique, as will become evident as the fabrication steps progress [118, 136].

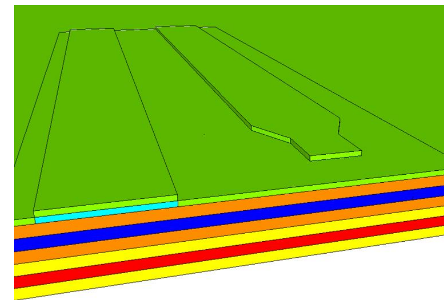

viii) The nitride was coated in photoresist.

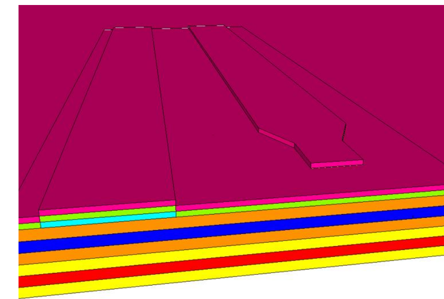

ix) The photoresist was then patterned with the second mask step to define the locations of the lower ridge.

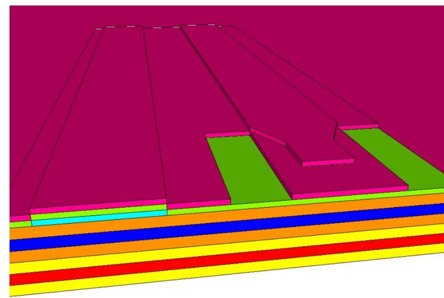

x) The exposed nitride was etched away to reveal the semiconductor where the lower deep etch would take place.

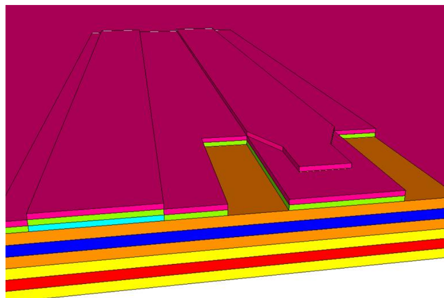

xi) The photoresist was removed so that it would not corrupt the next etch though the semiconductor material.

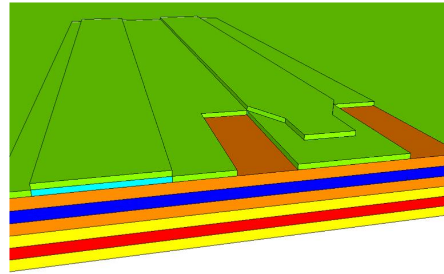

xii) The first etch was performed to remove the exposed semiconductor down to the required lower waveguide height. This etch partially defined the lower ridge, but at this point the etch remained in the upper layers.

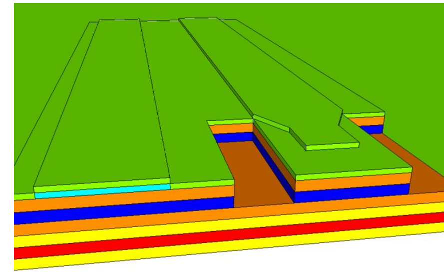

xiii) The nitride was then removed, leaving only the previously buried oxide.

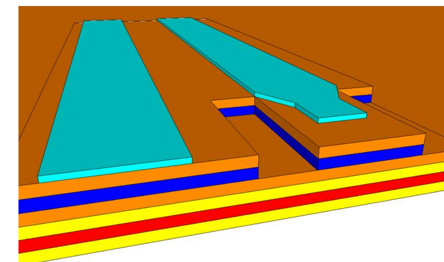

xiv) The second etch was then performed, which removed the exposed semiconductor creating the upper waveguide ridge. The lower ridge was simultaneously completed with this etch. The benefit of using both oxide and nitride was that the ridges were defined together, and so they were self-aligned. There was no lateral mismatch that would offset the waveguides and cause unwanted reflections within devices.

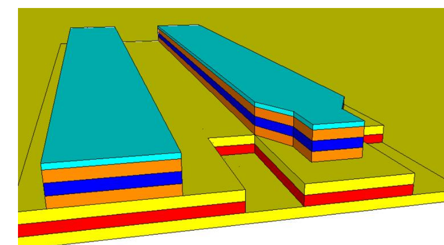

xv) With the two ridges etched using the steps above, oxide was coated onto the wafer.

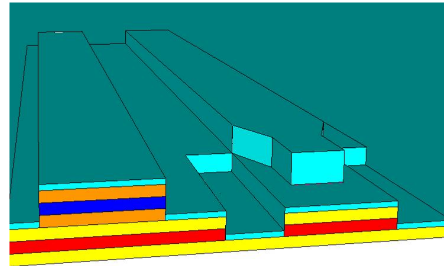

xvi) Then the wafer was covered once more with photoresist.

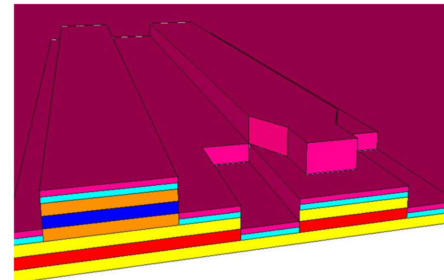

xvii) A third mask step was used to remove the photoresist wherever the oxide should be opened on the upper waveguide.

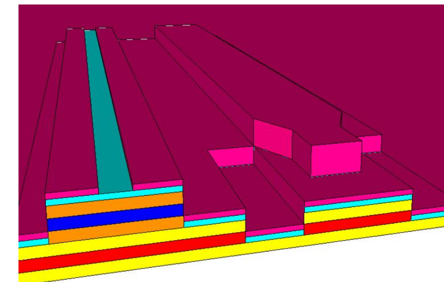

xviii) Once the photoresist had been patterned, the oxide was etched away to expose the upper waveguide semiconductor.

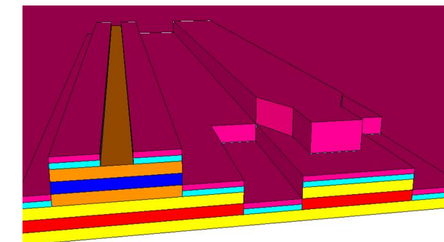

xix) The photoresist was then completely removed.

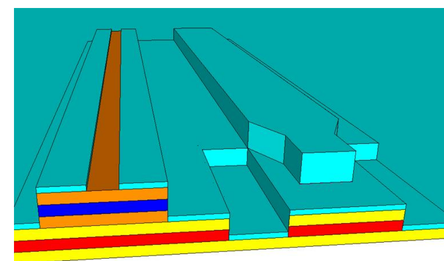

xx) A new coat of photoresist replaced the previous.

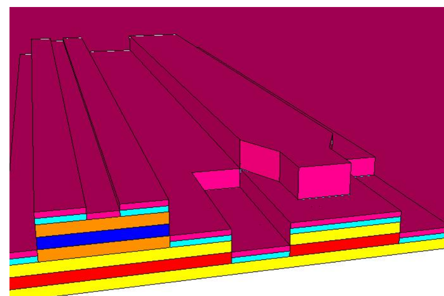

xxi) The photoresist was pattered using a fourth mask step, removing photoresist at those locations that required metal contact. The metal then touched the semiconductor of the upper waveguide at the exposed sections from the previous oxide opening.

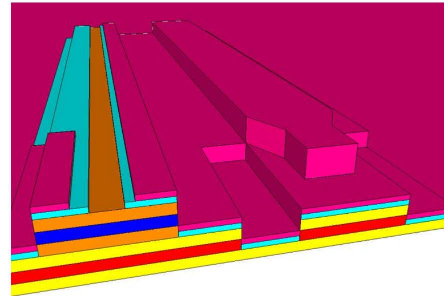

xxii) Metal was evaporated onto the wafer.

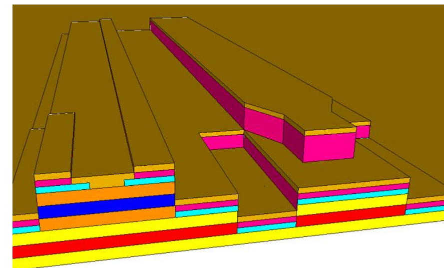

xxiii) The photoresist was dissolved to lift-off any metal on top of it. This technique left metal only on the exposed oxide and semiconductor sections, creating the metal contact pads.

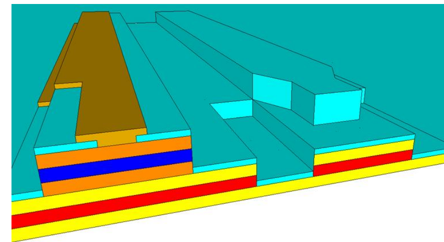

xxiv) The previous two mask steps were then repeated to achieve metal contact for the shared n-contact and the lower waveguide p-contact. Photoresist was coated onto the wafer.

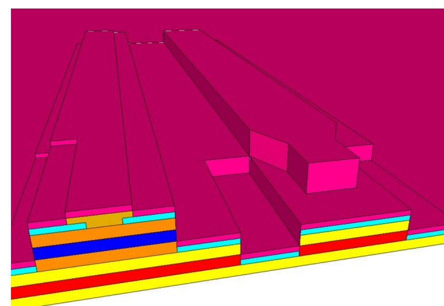

xxv) The photoresist was patterned by the fifth mask step to remove it from those places that required metal contact. In this case both the middle n and bottom p were patterned simultaneously despite their different depths. This was done to minimise steps as discussed previously.

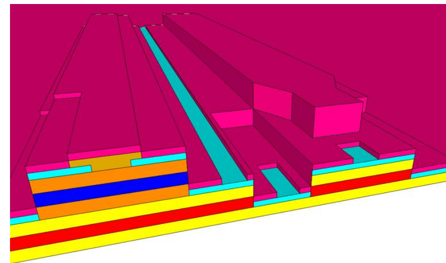

xxvi) The uncovered oxide was etched away to expose the semiconductor beneath.

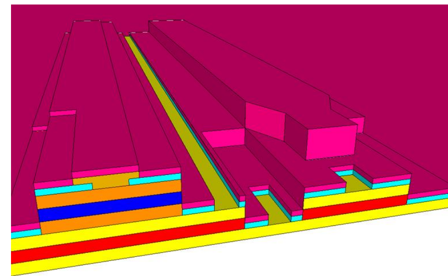

xxvii) The photoresist was then removed.

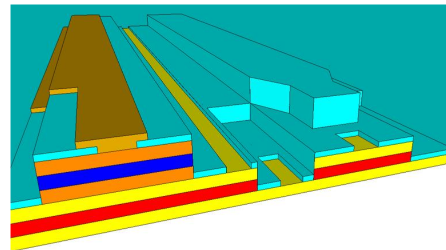

xxviii) A replacement coating of photoresist was put onto the wafer.

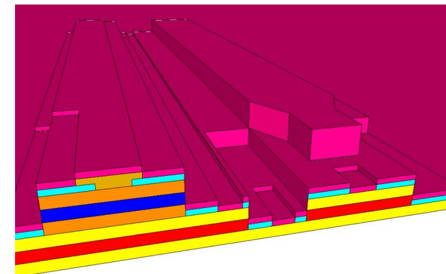

xxix) The photoresist was patterned with the sixth and final mask step to expose both semiconductor and oxide sections wherever the lower level metal was desired.

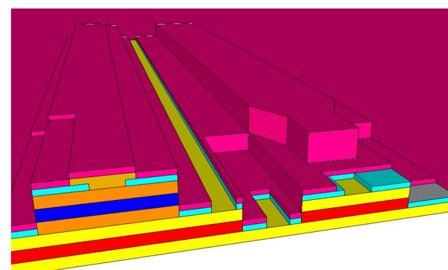

xxx) The wafer was covered in metal.

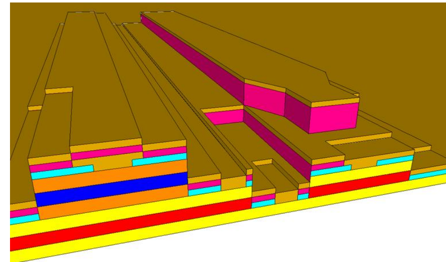

xxxi) Then the photoresist was removed so that metal only remained where metal pads were designed.

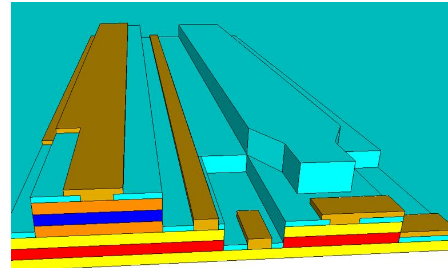

The final structure is shown at the end of the above steps. It illustrates two waveguides at different depths, the upper waveguide on the left, and the lower waveguide, including a taper transition from the upper waveguide, on the right-hand side. Metal contacts ran along the centre of the upper and lower ridges to provide current injection, and spanned further to the side to allow easier probing during experiments. Metal also contacted substrate sections away from the ridge to complete the circuit junctions. The sample taper from the upper waveguide to the lower waveguide illustrates that the ridges were self-aligned by the process so that the mode could transition smoothly between them.

4.2.3 Mask Design

The vertical integration fabrication process was outlined in the previous Section 4.2.2, and required 6 mask steps. Test devices were designed using these mask steps, resulting in the two mask plates shown in Figure 4.6. Each mask plate features 4 quadrants, as was discussed in Chapter 3.2.1, so that there was space on one plate for two more masks. The upper ridge mask was repeated because it contained the smallest feature sizes, belonging to the submicron taper tips. The three upper ridge mask sections were used simultaneously on a single wafer to define three quadrants of the wafer. The increased area allowed the wafer to be positioned on the stage easier and created a more uniform photoresist flow over the top, allowing better definition of the ridges.

The test devices included the material characterisation structures examined in Chapter 3.2.2. The large area diodes were placed on both the upper and lower ridges, to allow measurements of the depletion width of each waveguide

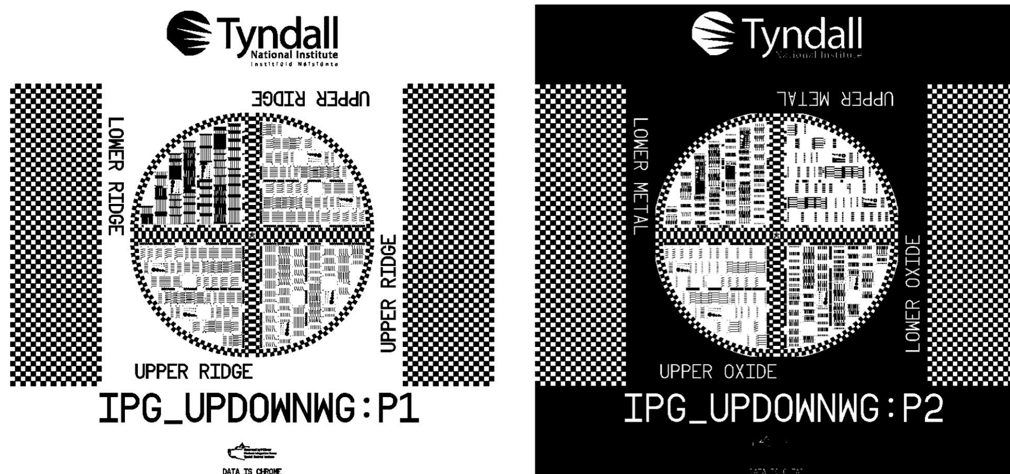

Figure 4.6: The two mask plates required to fabricate the up-down transition devices. Included mask steps are upper and lower ridges, oxide openings and metal lift-offs on both upper and lower levels. The upper ridge is repeated so that if desired it can be performed simultaneously on 3/4s of a wafer to increase the precision of the submicron tapers. Note that the polarity of the masks plates are different, owing to the abundance of cover required in the mask P2 relative to P1, but the final real plates look like P1.

through CV measurements, as well as IV and absorption measurements. FP cavities of varying widths were placed on each waveguide ridge also, to provide LIV measurements to characterise the emitting wavelength and the optical output's dependence on ridge width. TLM structures informed of the effectiveness of the metal contacts on each of the three layers defined by the process, the top p-, middle n- and bottom p-contacts. As always, alignment marks were included for each mask step to allow precision alignment. These test devices allowed each waveguide to be characterised independently.

New test structures were designed and added to characterise the vertical mode transition, three of which are shown designed in Figure 4.7 and fabricated and under test in Figure 4.8. In the simplest case the device was a straight cavity, Figure 4.7a and Figure 4.8a, featuring the taper transition dimensions predicted in Chapter 2.3.2. The upper waveguide is on the left of Figures 4.7a and 4.8a, and the lower waveguide with all the upper layers removed is on the right after a taper. Different taper lengths were fabricated on different bars to compare the transition performance with taper length. The length of the active region was maintained at $600\mu m$ for all the devices, to allow an even comparison.

A lensed fibre was brought up to the facet of the devices to capture emitted light. When the fibre was aligned to the biased lower waveguide the active material emission was expected, and when the fibre was aligned to the biased upper

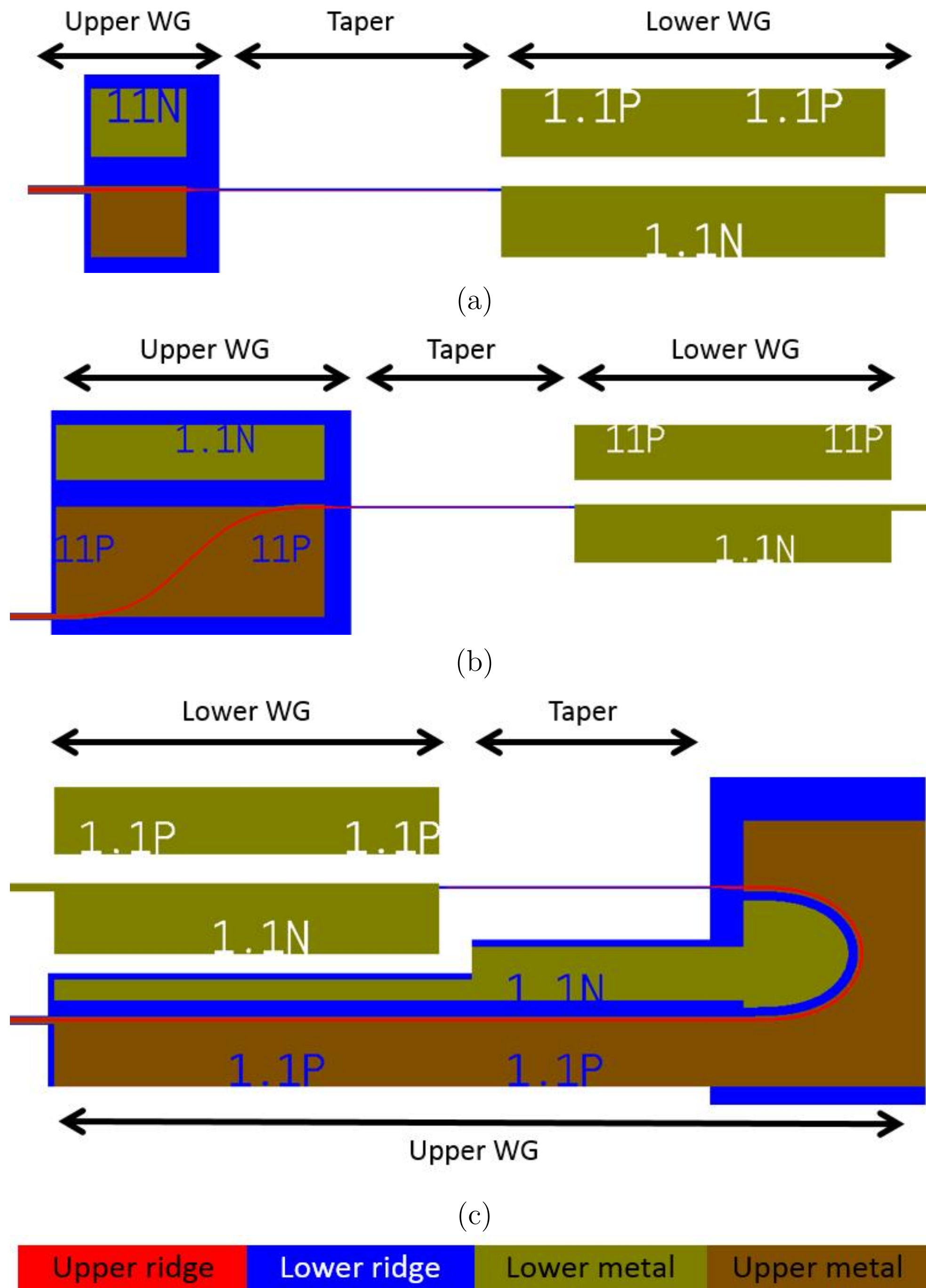

Figure 4.7: Overlay of lithographic masks for up-down WG test devices, indicating the upper and lower WGs and the taper transition between them; (a) A straight device, (b) an s-bend device and (c) a loop device. All devices feature lateral tapers to vertically transition the mode in the waveguides.

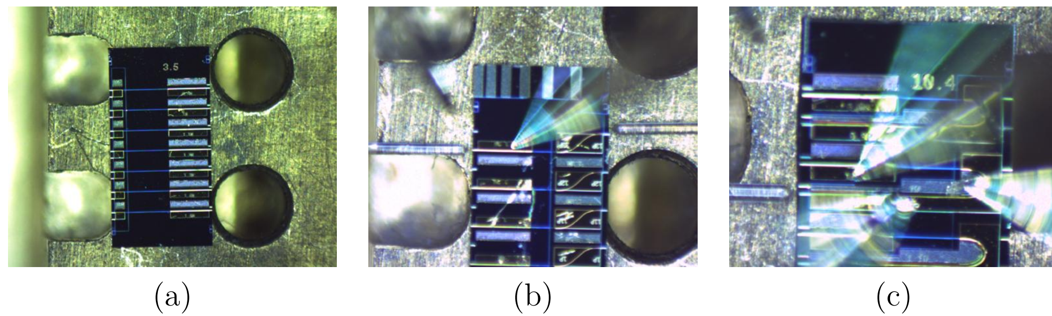

(a) (b) (c)

Figure 4.8: Fabricated up-down WG test devices; (a) A straight device, (b) an s-bend device and (c) a loop device. All devices feature lateral tapers to vertically transition the mode in the waveguides. The upper waveguide is on the left in (a) and (b), and the bottom of (c), but has been etched away to leave only the lower waveguide at the end of the taper.

waveguide facet blueshifted emission from the passive waveguide was expected.

There were also iterations that placed a slot between the active waveguide and the transition taper. This slot simulated a cleaved facet and introduced a reflectivity that could be used by the lower waveguide to achieve lasing operation. Otherwise, in the other iterations of devices, the light needed to transition vertically between the waveguides and use the cleaved facets at both the active and passive outputs as reflectors. The resulting cavity length could be very large considering the size of the adiabatic tapers, and losses in the taper transition may have prevented threshold from being reached.

It may have been possible for the lower active waveguide emission to pass straight through the substrate and produce erroneous measurement from the upper waveguide facets, without an actual vertical transition. This possibility was eliminated by incorporating an s-bend into the waveguide. This s-bend resided in the passive waveguide so that the active emission remained constrained along one dimension only. Figure 4.7b shows the design of an s-bend device, with the upper waveguide s-bend on the left, and the taper and lower waveguide section on the right just as in the straight waveguide of Figure 4.7a. Figure 4.8b shows a fabricated bar of s-bend devices, and lensed fibre can be seen approaching each facet to record optical output or inject optical input.

Furthermore, the bend could be extended to a full 180° to completely eliminate erroneous throughput from the active region to the passive. Figure 4.7c shows the design of a device with such a bend. The active lower waveguide has been folded next to the upper waveguide, compared to Figures 4.7a and b. As the active region was maintained at $600\mu m$ for all the devices, the upper waveguide in this case became longer. Figure 4.8c shows fabricated 180° bend devices, and a

single lensed fibre can be seen approaching the single cleave facet in this case. By bending the waveguides back onto themselves the emitted modes could also be imaged together using the same fibre, allowing a comparison of the mode shapes.

As seen in the fabricated devices of Figure 4.8, each device was repeated along the bar. The widths of these repetitions varied from each other by increments of $0.1\mu m$. The variation in width was included so that at least one device from each bar should have functioned despite any fabrication error. It has already been mentioned in previous Chapters, first at Section 2.2.5, that there is a fabrication tolerance, and that vertically coupled waveguides are reliant on precise submicron features. Thus any variation results in non-optimised devices. The taper width can be either over- or under-exposed during processing, so that the resulting ridge is either narrower or wider than desired. If the mask designs deliberately made the devices too wide or too narrow then over- or under-exposing resulted in the actual design being achieved.

The minimum feature size guaranteed on lithographic masks is actually $0.6\mu m$, with smaller dimensions achieved only on a best effort basis [227]. Smaller dimension guarantees are available, but they are increasingly expensive. Thus, in order to achieve the small taper dimensions down to $0.4\mu m$, the entire sample was deliberately over-exposed. The array of devices of different widths on each bar allow the designed dimensions to be achieved by at least one of those devices.

4.3 Testing and Characterisation

The vertically stacked waveguide materials of Table 4.1 were grown and subsequently fabricated with the steps outlined in Section 4.2. The test structures looked to be produced satisfactorily, and each bar of devices were then cleaved apart. The device bars were placed on the brass chuck as shown earlier in Figure 3.17b. Care had to be taken to apply bias in the correct orientation as the stacked structure features the p-i-n-i-p configuration which is inverted from the usual p-i-n. Two probes were required to bias the upper waveguide as it possessed only topside contacts, while the lower laser could utilise its back side p-contact.

The following sections outline the experimental results obtained from the different test devices, describing the characterisation of each waveguide and the transition between them.

4.3.1 LIV Measurements

The large area diode structures for material testing allowed easy probe contact to the devices. For the lower waveguide the p-contact was made with a back contact on the bottom of the substrate, while for the upper waveguide two probes were needed to make n- and p-contacts from the top.

The IV measurements of the two waveguides are shown in Figure 4.9. The lower laser material had a greater slope, arising from both its material composition and higher doping. The turn-on voltage of both waveguides was the same, illustrating that this was determined by the InP more than by the cores.

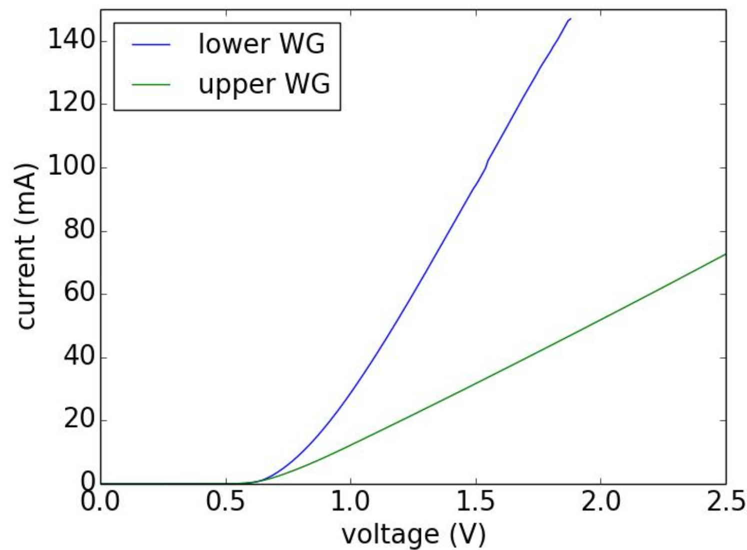

Figure 4.9: IV plot of both the lower laser and upper waveguide.

The turn-on voltage was reduced compared to the $1V$ seen earlier in Chapter 3.3.1 for the p-substrate lasers on their own. For the upper waveguide this may make sense as the p-InP wafer plays no part, but for the lower laser no difference was expected compared to the lasers on their own. The reason for the different voltages could result from the metal contact to the semiconductor rather than the semiconductor material itself.

The slope of the IV curves were used to calculate the resistances of the different waveguides. The resulting resistance of the full p-i-n-i-p structure's active material was a match to the 10Ω of the n-i-p lasers previously grown and tested. The failed n-i-p laser growth investigated in Chapter 3.3 had a lower resistance of 3Ω. The correlation between this growth and the previous successful lasers indicated that the material should lase.

The optical output power can be seen in the LI curves of Figure 4.10 for both

the lower and upper waveguides fabricated into FP cavities, as displayed in Figure 4.11. It can be seen that the FP cavity did not lase for either waveguide. It was expected that at least the QWs of the lower waveguide should lase, following the successful growth of the p-substrate lasers in Chapter 3.

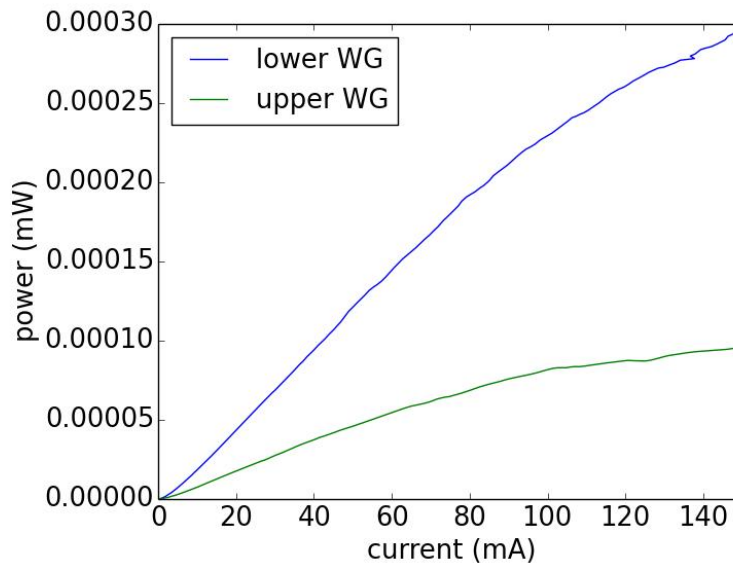

Figure 4.10: FP cavity LIs of the lower and upper WGs.

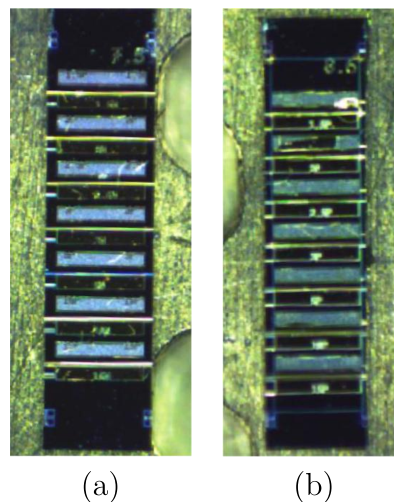

(a) (b)

Figure 4.11: FP cavities fabricated on (a) lower WG layers and (b) upper WG layers. The ridge and bottom contact metals can be differentiated by their colour, with the bottom contact metal having a blue tinge.

The active material had the greater output power in Figure 4.10. This was expected because the lower waveguide possessed 5 QWs to increase the carrier confinement and thus increase optical recombination and photon emission. However the comparison between the two waveguides, that neither lase, indicated that

the QWs were not functioning and the lower waveguide was acting more akin to a bulk layer.

Rather than DC injection, the waveguides could be injected with pulses of current in order to reduce the overall heating of the device. Figure 4.12 shows the resulting pulsed LIs, which show that the wide ridge waveguides can be made to lase. The threshold current was high, as it was for the failed p-substrate laser growth in Chapter 3, illustrating poor performance. Also, the upper waveguide lased comparably to the lower waveguide, insinuating further that the lower waveguide operated as a bulk layer rather than as QWs with increased carrier confinement.

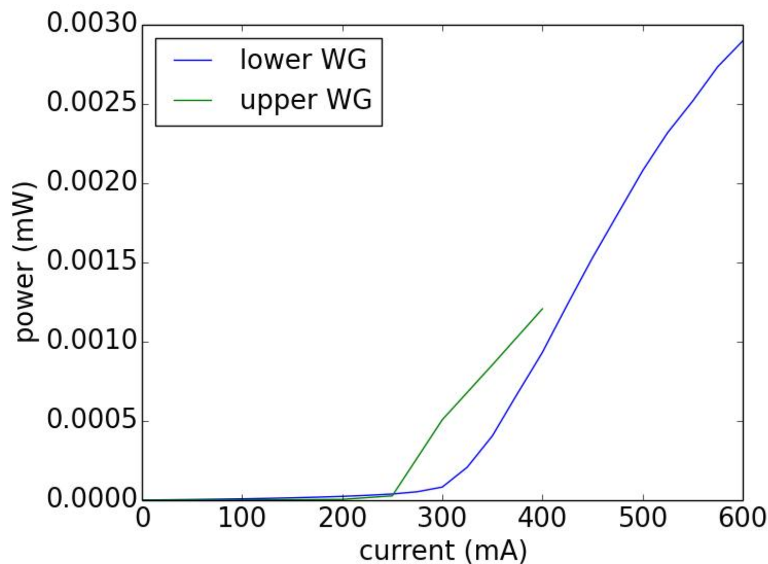

Figure 4.12: Pulsed LIs comparing the upper and lower WG emission, at optimum lasing conditions of 4% duty cycle and $0.35\mu s$ pulse width.

Only the wide ridges could be made to lase under pulse operation. For the narrower ridges the optical output was increased as the duty cycle of the pulse reached its maximum, approximating DC operation. Thus the optical power was simply increased by an increase in carriers. It may be that the narrower ridges could be made to lase for smaller duty cycles than the machinery could perform. For the wider ridges there is an optimum duty cycle at which the optical emission is maximised, with the output decreasing for duty cycles smaller or larger. At this optimum point the injected electrical power was enough to compensate the losses, while not high enough to overheat the device.

The spectrum of the lower waveguide FPs, as recorded with an OSA, is shown in Figure 4.13, and indicated an extreme error because the emission was centred

around 1500nm. The emission had the same spectrum under pulsed operation, so the laser emission was quite simply not as designed.

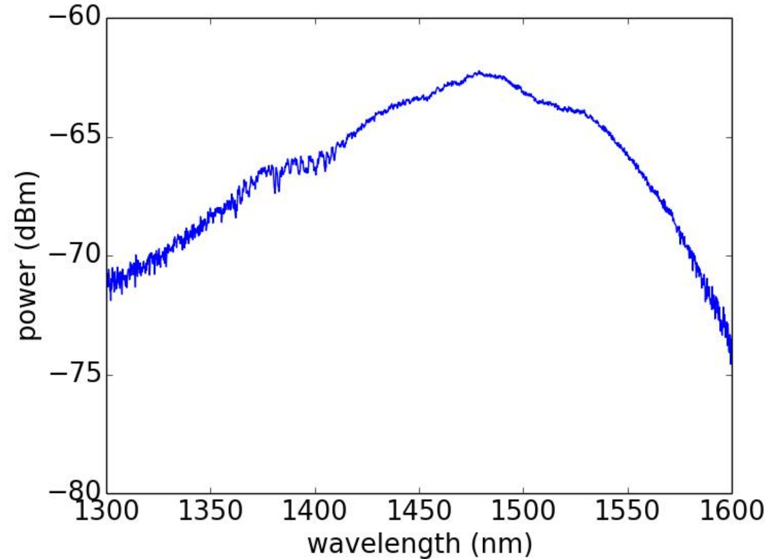

Figure 4.13: OSA trace from an FP cavity on the lower WG.

Even for the p-substrate lasers that failed in Chapter 3 the optical emission was centred at the desired wavelength. The fact that the emission in this full structure case differed, indicated that the growth was simply incorrect rather than suffering some mid-growth problem.

However, it needed to be proven that p-dopant diffusion was no longer responsible for the failure, because perhaps the increased material and growth time resulted in dopants filling the quantum wells to unwanted energy levels.

4.3.2 CV Measurements

The large area diode test structures were used once again to measure the capacitance of both the upper and lower waveguides. The CV measurement method was outlined previously in Section 3.3.3.

The resulting depletion widths extracted from the capacitance of the waveguides under bias is shown in Figure 4.14, along with the depletion widths of the previous p-substrate lasers of Chapter 3.

The upper waveguide had a much larger depletion width than the lower waveguide. This was expected from Table 4.1, where the upper waveguide's intrinsic region approached 800μm when the undoped SCH layers were included.

The lower active waveguides had depletion widths that behaved similarly to the pulled back doping p-substrate laser from Chapter 3, as comparable in Figure

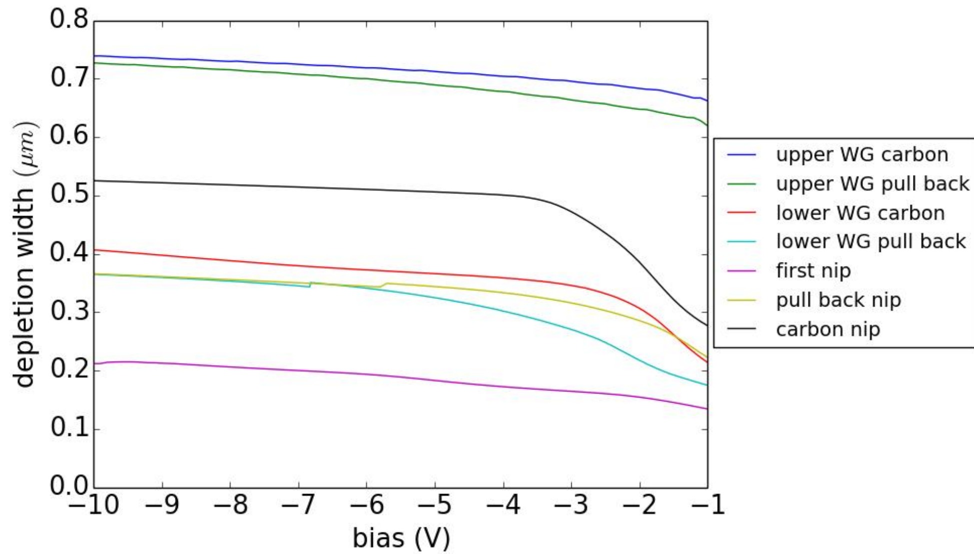

Figure 4.14: Depletion width versus bias for the two p-i-n-i-p structures' upper and lower WGs, and the previous n-i-p lasers, as extracted from CV measurements.

4.14. Thus it could be determined that the pull-back doping and carbon doping had maintained the intrinsic region and blocked p-dopants from diffusing into the core.

The pulled back doping growth of this full p-i-n-i-p structure is reduced in Figure 4.14 from the pulled back doping n-i-p growth. This indicates that the dopants diffused further into the intrinsic region during the longer stacked growth, as would be expected. However, the depletion width is still larger than the failed first n-i-p growth and comparable to the successful updated n-i-p growths.

The full p-i-n-i-p carbon blocking layer growth is also reduced in Figure 4.14 compared to the n-i-p growth. The resulting depletion width is very close to that of the successful pulled back doping n-i-p growth, and slightly larger. During the longer stacked growth the carbon blocking layer was less effective at restraining dopant diffusion, but remained effective enough to maintain an acceptable depletion width.

The fact that the intrinsic region was of the correct width indicates that the failure of the active material had a different source than p-dopant diffusion. This was further supported by the same emission behaviour from both the carbon blocking layer material and pulled-back doping material. Each growth iteration should have been affected differently if the p-doped section were responsible, so the fact they are not indicated problems with the QWs themselves.

4.3.3 Growth Reports

In order to correct the growth and design a functioning laser in the lower waveguide, material tests were carried out. Calibration growths had already been performed, Section 4.1, and presented waveguides with the correct emission wavelengths. Clearly something went wrong in the full stacked growth to cause the broad lower waveguide emission.

The upper waveguide functioned as desired and so did not require further testing. It had an emission wavelength close to that designed, and it will be shown in the following Sections that the taper displayed the wavelength dependence that it was constructed for. These upper layers were grown simultaneously onto the different growths of Table 4.1, and successfully behaved the same.

On a new unprocessed wafer piece, the working upper waveguide layers were etched away completely to allow the active layers beneath to be tested. XRD and PL results are shown in Figure 4.15.

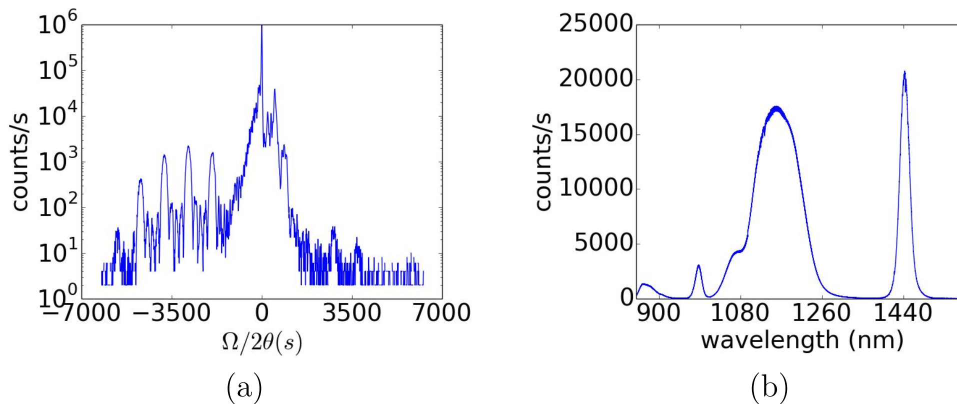

Figure 4.15: Calibration results for the grown lower active material with the upper layers removed. (a) XRD data showing that the lattice mismatch should be tolerable, and (b) PL data showing that the overall emission is at a much lower wavelength than requested for the laser.

The XRD data shows that the peaks reside close to the central angle, so the material should be satisfactorily lattice matched to the InP substrate. The additional peaks close to the centre were from the SCH layers. The periodic peaks to the left were the result of the QWs, which act as a grating and support multiple angles of measurement.

The low temperature PL measurement revealed that the emission of the material differed completely from that designed. There was a large emission centred around 1200nm, that must have arisen from either the intermediate waveguide in the barrier layers or the SCH layers beside the QWs, Table 4.1.

A direct repeat growth of the same pulled back doping material was made to test if the first growth had simply suffered a catastrophic failure independent of the design. The upper passive layers of the structure were immediately removed to allow a repeat of the PL measurement of the lower active layers. Figure 4.16 shows the PL result, which still displayed large emission at 1200nm. In this case though there was now weak emission at the desired 1555nm. The peak was so weak that it was unclear if the peak was genuinely a result of the material's emission or if it was due to the cut-off frequency of the measuring equipment.

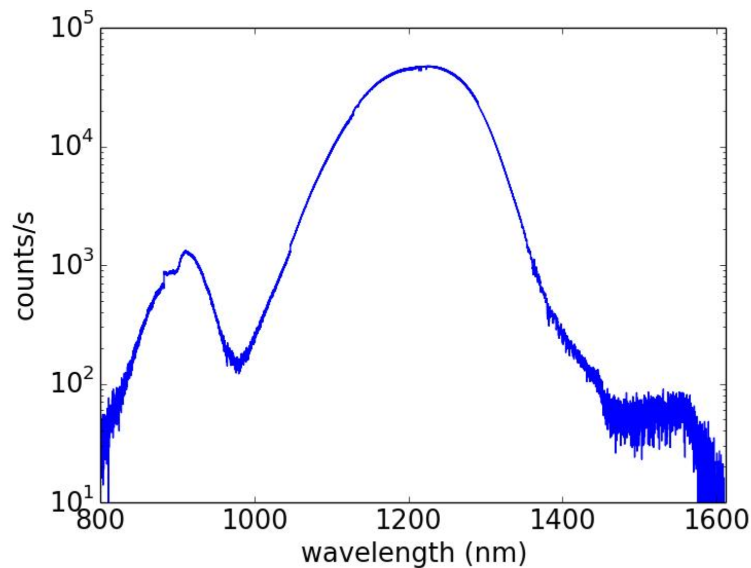

Figure 4.16: PL data of repeated stacked WG growth, with the upper layers removed to leave only the lower active layers.

Nevertheless, the material test mask of Chapter 3.2.2 was employed once more to fabricate FP cavities and large area diodes, as well as other test structures, onto the lower active waveguide with the upper layers removed. The FP cavities remained with weak non-lasing emission, and the spectrum is shown in the OSA trace of Figure 4.17. The OSA trace revealed that the repeated growth had emission indeed centred at 1550nm. Though the emission was still rather broad, it was not as broad as previously seen back in Figure 4.13, and was merely a result of the weak emission, comparable to the failed n-i-p lasers of Chapter 3.

Something was incorrect about the growth material, which may have arisen from the difficulty of growing such a thick structure. The active layers had poor optical efficiency. It was shown in Section 4.3.2 that the depletion width of the active region was as wide as previously functioning p-substrate lasers, indicating that p-dopant diffusion had been successfully restricted and was not responsible for the poor optical efficiency. The active layers were grown to emit at the desired

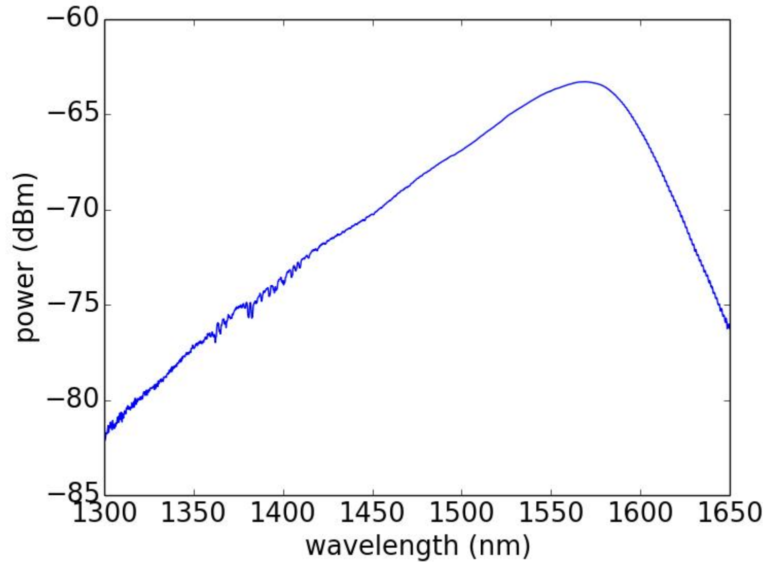

Figure 4.17: OSA trace from a 300μm long FP cavity fabricated on the repeated PINIP material with the upper layers removed to leave only the lower active layers.

wavelength of 1550nm, but just could not achieve a high conversion rate from carriers to photons.

4.3.4 Up-Down Transitions

The previous sections found that the lower waveguide in the stacked structure was not operating as designed, and the cause was unclear. The emission of the lower active waveguide in the processed growth was unfortunately not a laser and had a broad spectrum about 1.5μm.

The altered active waveguide actually presented the ability for informative measurements of the vertical transition. This broad spectrum stretched across both the C and L bands of telecommunication wavelengths, allowing a thorough measurement of the taper transition's wavelength dependence.

While the lower active waveguide had experienced some growth modifications, the upper waveguide remained as designed. All the layers above the laser layers were common to both growth iterations and were grown sequentially.

4.3.4.1 Wavelength Filtering

Section 4.3.1 displayed the optical emission of the lower waveguide biased independently in Figure 4.13. For the upper waveguide under test, if instead the shared n-contact was probed along with the backside p-contact, the active ma-

terial could be injected with current. The resulting optical emission was centred about 1550nm.

The active waveguide emission was thus altered from being broad 1500nm centred emission, when on its own, to the desired 1550nm. The upper layers had the affect of filtering the active waveguide wavelength emission.

It was shown in Chapter 2 that a mode is supported in the waveguide with the highest refractive index, which for the stacked structure was the upper waveguide. Thus, the light generated in the lower layers was guided and supported by the dominant upper waveguide, but only at the wavelengths supported by the vertical transition. The transition-assisting intermediate waveguide in the barrier layers was designed for a wavelength of $1.55\mu m$, and the filtering of the active waveguide emission matched this, showing that the epitaxial layer design was operating as desired.

The vertical transition from lower to upper waveguides was investigated properly using the test structures outlined in Section 4.2.3. Test structures featured both upper and lower waveguides with an upper waveguide taper to incite vertical coupling. By comparing the different emissions from the upper and lower waveguide facets the effect of the taper transition could be determined.

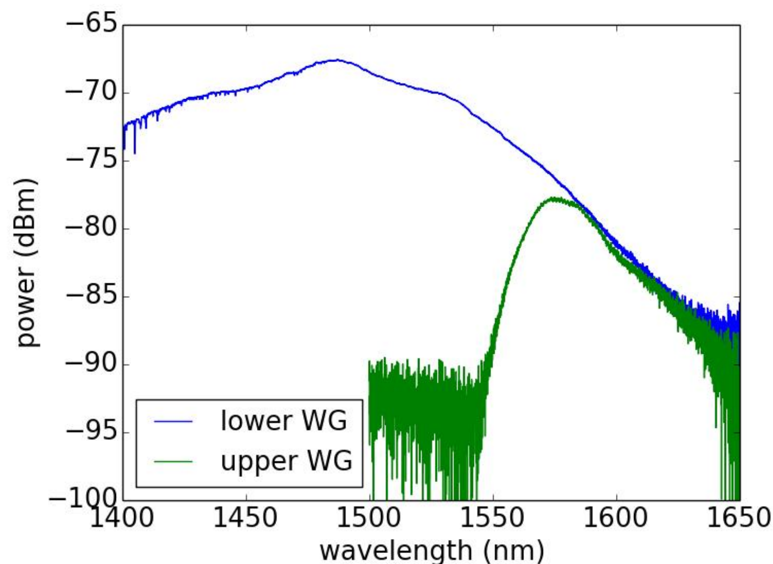

Figure 4.18: The spectra from the active lower WG and passive upper WG emission on an OSA, for the lower active WG biased only.

Injecting only the active waveguide with current produced the emission shown in Figure 4.18 from each of the waveguides. The lower waveguide emission remained the same as for its FPs in Section 4.3.1, but the upper waveguide emission

was filtered to above 1550nm. This indicated that a vertical mode transition was occurring and that the transition was operating at the designed wavelength of 1550nm.

4.3.4.2 Maximised Transmission

None of the devices lased, but this was not expected because the FP cavities did not lase, and the addition of the vertical transition would have introduced additional losses to be overcome.

The devices with the as-designed dimensions, that is with waveguide ridges of $2.5\mu m$ and a transition from $1.1\mu m$ to $0.4\mu m$, produced the highest optical output power. This indicated that the fabrication managed to achieve the exact specifications of the devices. Thus, precise alignment had been achieved to define submicron taper tips, verifying the validity of the monolithic lateral taper fabrication.

The maximum optical output power was achieved for a taper length of $200\mu m$. In the simulations of Chapter 2.3.2 a taper length of above $600\mu m$ was predicted to be necessary. It should be noted that these devices did not lase, and thus the maximised output for $200\mu m$ can be deemed to be the result of simply decreasing the length, and with it the material absorption losses. A taper length of $800\mu m$ was found to emit more power than a $600\mu m$ length, indicating perhaps that the longer taper begins to exhibit its adiabaticity and balance the increased material losses.

There was not enough optical power from this active material to robustly determine the length dependence of the taper. If indeed a $200\mu m$ taper is found to perform best then it would achieve the target of photonic integration by minimising the size beyond expectations.

4.3.4.3 Waveguiding

It can be noted that for all the test devices, such as in Figure 4.8, the measuring lensed fibre was aligned to the same position irrespective of which section was biased. When the upper waveguide was biased and the lensed fibre was aligned to the maximum optical output, this remained in the same position if instead the lower active waveguide section was biased. This indicated that the light was being waveguided up the taper transition.

The s-bend test devices, Figure 4.8b, indicated that the light was being guided both vertically and laterally by the waveguides. The s-bend was in the upper waveguide layers so that the active emission should have been confined along

the direction of the lower cavity, it should not have been able to diffract to the offset output. When the lensed fibre on the upper waveguide output side was aligned to the direction of the active waveguide of the s-bend device, there was no coupling. When instead the fibre was coupled to the upper waveguide output, Figure 4.8b, there was coupling, proving that lateral and vertical waveguiding was taking place. The s-bend devices also displayed the wavelength filtering of the vertical transition shown before in Figure 4.18 in Section 4.3.4.1.

The loop-back device of Figure 4.8c also verified that the light produced by the lower active waveguide was guided up the taper and around the bend back to the upper waveguide output. The lensed fibre could be shifted from upper to lower waveguide outputs to compare the emission. A lesser magnitude was received out the upper waveguide, as expected because the mode experiences losses along the waveguide and taper, especially as the active emission was not powerful in this case.

The lensed fibre was mounted on a piezoelectric motor to allow precise, minute computer control of its position. The lensed fibre was then scanned across the plane of the facet to record the optical power at different positions, creating an image of the emitted mode.

The lower waveguide and upper waveguide output mode images are shown in Figure 4.19, for only the lower active waveguide forward biased. The imaged modes are different, displaying that the mode undergoes a transition within the device. Figure 4.19 shows the theoretical mode solutions for comparison with the measured results.

The mode imaged from the lower waveguide matched the shape predicted by the numerical solution of the geometry. Characteristically, the mode reached vertically downward into the substrate. On the other hand, the upper waveguide imaged mode was confined more vertically, matching predictions, arising from the narrower ridge and barrier region beneath it.

The loop-back device of Figure 4.8c was designed to allow a single fibre scan across both waveguide outputs. However, there was an inherent tilt which either derived from the laboratory stage or from the wafer thinning of the sample itself. The tilt was minuscule, but the dimensions being considered were so small that the tilt was substantial. The tilt resulted in the upper waveguide mode seemingly residing below the lower waveguide. This could be corrected by imaging two adjacent lower waveguide modes. The lower waveguides shared the same layer and so the tilt could be extracted from the difference in their imaged position.

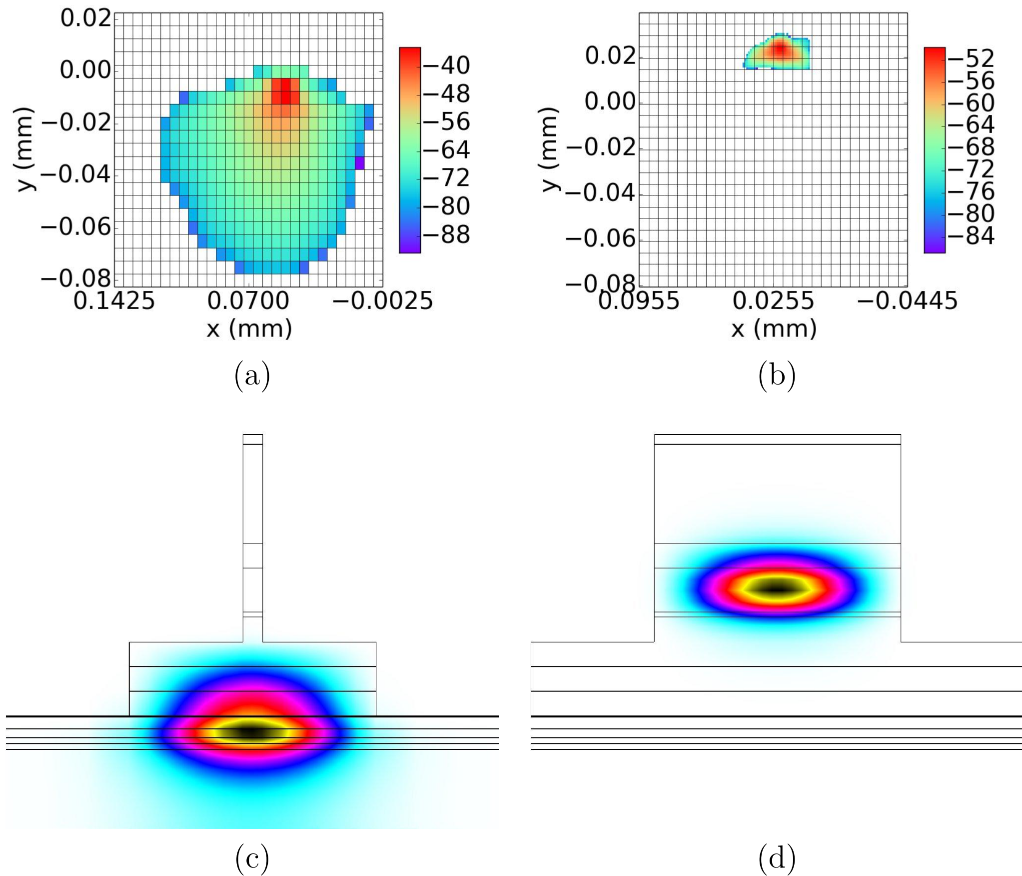

Figure 4.19: The scanned images of the emitted mode from the (a) lower and (b) upper WGs, and calculated mode solutions in the (c) lower and (d) upper waveguide.

4.3.5 TLS Measurements

The inherent vertical transitions have been observed in the previous Section 4.3.4, showing that the designed operating wavelength of 1550nm transitioned successfully. Each separate wavelength was tested by using a tunable laser source (TLS).

A lensed fibre at one side of the device injected the TLS into a facet, while a second lensed fibre at the other side of the device was used to record the throughput. An optical circulator was placed between the TLS and the lensed fibre to ensure no reflections from the device facet interfered with the TLS itself. The circulator only allowed light to travel unidirectionally along the path of the TLS to the device, and then from the device to a separate output. This other output path allowed a measurement of any reflections or emission from the device.

Setting up a TLS with an optical circulator allowed the topography of the facet to be imaged [228]. The lensed fibre was moved across the plane of the facet, and the reflected TLS light was detected at each point to create an image.

The imaged facet of a vertically stacked waveguides structure is shown in Figure 4.20. While this was a quick measurement without any decided accuracy, the two ridges of the waveguides can nevertheless be seen stacked above each other, rising from the plane of the wafer.

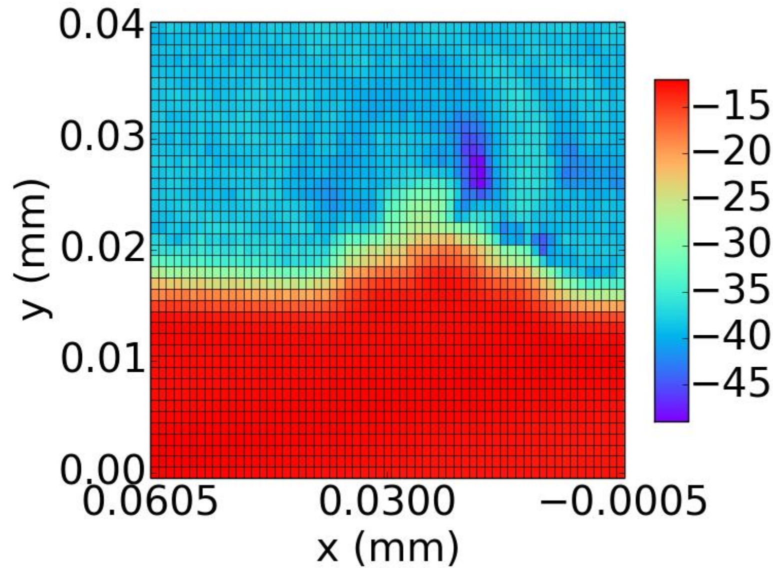

Figure 4.20: Scanned image of vertically stacked waveguide structure, using the reflections from a TLS transmitting through a lensed fibre mounted on piezoelectric motors.

As has been mentioned, s-bends and loops, Figure 4.8b, were included in the test devices to prevent transmission through the substrate that would create false measurements. This was still valid for TLS injection, but free space coupling through the air over the device was now another concern. The s-bend radius was selected to be large so that a high magnitude of the TLS could not disperse through the air and reach the recording lensed fibre. An s-bend device with two lensed fibres, one for input and one for recording, are shown in Figure 4.8a aligned separately to the upper and lower waveguides. In fact, the TLS spread was large enough that it was recorded by the opposite lensed fibre even when offset. However the magnitude of the recorded TLS became small when a device under test was placed between the fibres and blocked the light.

The waveguide was reverse biased to check that the TLS was aligned properly to a waveguide facet. By reverse biasing the waveguide it acted as a photodetector, producing photocurrent for incident light. When the lensed fibre emitting the TLS was correctly aligned to the waveguide, the photocurrent was largest owing to the greatest optical coupling.

It was found that once the TLS had been optimally aligned to a waveguide, the

recording lensed fibre on the other side still recorded the TLS emission even when the waveguide was highly reverse biased. The reverse biased waveguide should have absorbed most of the TLS light, and the fact that it did not indicated that free space coupling was substantial, and made measurement difficult.

Rather than using a lensed fibre opposite the injecting TLS, the device itself was operated as a photodiode. The TLS was coupled to the upper waveguide by maximising the photocurrent. With the TLS coupling into the device, the upper waveguide was unbiased to allow it to assume its passive state. The lower waveguide was then reverse biased to operate as a photodetector. It was found that the photocurrent generated in the lower laser was high when the TLS was aligned to the upper waveguide facet. When the TLS was unaligned from the upper waveguide, even when placed in the line of the active waveguide, the photocurrent reduced towards null. This proved that the upper waveguide guided the light around the s-bend and down the taper transition to the lower waveguide.

Mounting the lensed fibre on piezoelectric motors allowed the fibre to be scanned across the facet to image the emitted mode just as in Figure 4.19 in Section 4.3.4.3. Figure 4.21 compares the lower active waveguide emission and the TLS throughput from the same device. The throughput TLS signal can be seen to have assumed the same shape as that of the lower waveguide on its own. The free space coupling TLS can be seen coming over the device on the top left, illustrating the usefulness of the s-bend as it allowed the guided light to be resolved separately.

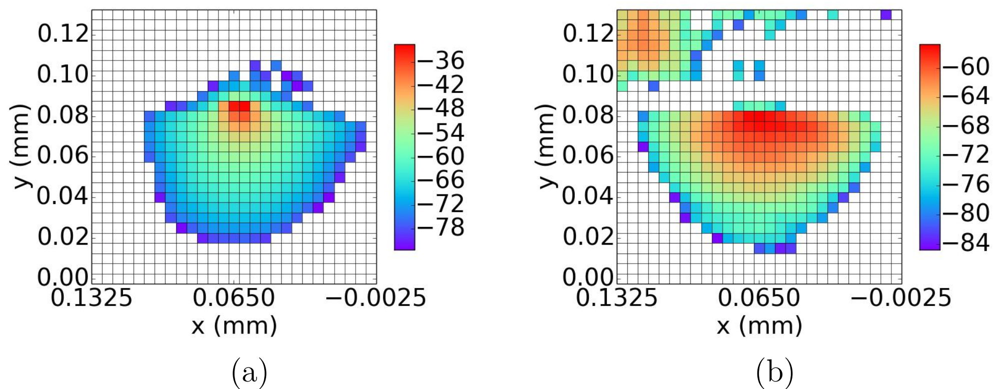

Figure 4.21: Scanned image of (a) the lower active waveguide mode and (b) the vertically guided TLS throughput.

The wavelength dependence of the taper transition was measured using the single frequency TLS. The wavelength dependence was simulated with BPM just like in Chapter 2.2.4. The initial mode in the lower waveguide was numerically solved for at each wavelength, and then launched along a down-to-up vertical

transition taper, recording the power at the end. The BPM simulation results are shown in Figure 4.22 alongside the measured results from the s-bend device.

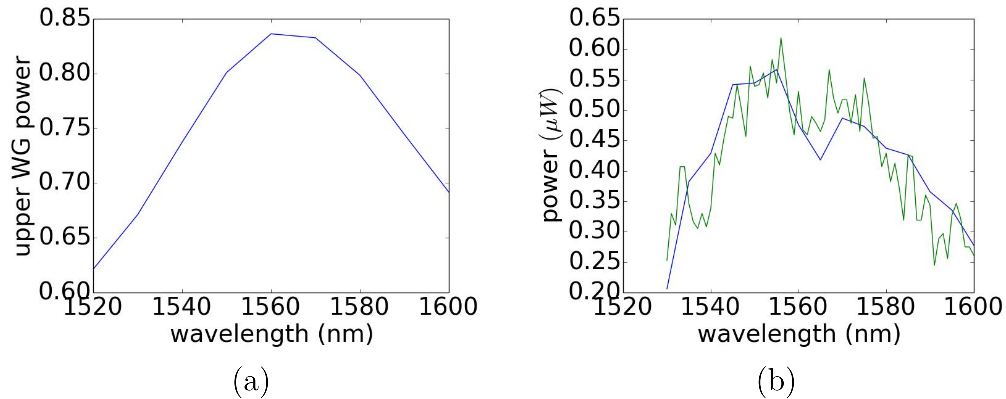

(a) (b)

Figure 4.22: The wavelength dependence of the vertical transition, for (a) the simulated BPM results and (b) two sets of measured throughput.

The simulation and experimental wavelength dependence results line-up quite well. The optimum transmission occurred at 1550nm, as was designed for the layer structure. Away from the peak wavelength the transmission decreased. In fact in the simulation the transmission began to increase once again, for the same reasons as previously discussed for a 3D constant overlap taper in Section 2.2.3. The mode solution begins to straddle both the upper and lower waveguides at larger wavelengths and thus the vertical transition becomes meaningless and the simulated power increases. In reality the higher wavelength modes are unsupported in the structure because they are absorbed by the lower waveguide.

4.4 Discussion and Conclusions

A vertical transition between an upper passive waveguide monolithically integrated above a lower active waveguide has been experimentally shown.

The stacked waveguides were grown to the specifications designed with theoretical simulations, and a new 6 mask process was designed to fabricate numerous test devices to prove the vertical transition. 6 mask steps is a low number to define two waveguides made of different material; regrowth techniques would require many more. The fewer steps are the benefit of monolithic integration, simplifying the fabrication and reducing the time and cost required to create devices.

The transition was shown by comparing the optical output from the lower active waveguide facet and the upper waveguide facet. The emission from the upper waveguide had filtered wavelengths compared to the lower waveguide, showing

that the taper transition had a wavelength dependence centred on $1.55\mu m$ as designed with simulations.

Bends incorporated into the test devices proved that the light was waveguided both laterally and vertically in the structure. Lensed fibre mounted on piezoelectric motors were used to scan images of the emitted mode shapes, proving that the modes from each stacked waveguide differed and matched numerical mode solutions of the geometry.

The upper passive layers performed as designed, allowing the correct wavelengths to transition vertically between the stacked waveguides. However the active layers had poor optical efficiency, which must result from the challenging thick epitaxial layers making up the stacked structure. CV measurements showed that the depletion width remained large enough in the active waveguide to allow operation, as proven in Chapter 3, so that p-dopant diffusion remained contained and could not be the cause of the poor optical performance. Despite its deviation from design, the actual grown active waveguide proved beneficial as it allowed an inherent measurement of the wavelength dependence of the taper transition.

In lieu of a laser, a TLS was injected into the device to prove that laser light of different single colours was guided. The wavelength dependence of the taper transition operated the same in the single wavelength case as for the broad spectrum, as would be expected.

The poorly performing active waveguide did not allow a definitive measurement of the transition performance with taper length. The transition is predicted to be more adiabatic for longer tapers, but increased length also introduces material losses and so some optimum length was expected. Measurements with these devices may support the predictions that the taper needs to be very long, $> 600\mu m$, to become adiabatic. The optical output power reduced with increasing taper length due to material absorption, but at the longest taper length of $800\mu m$ the power began to increase.

Chapter 5

Conclusions and Future Work

5.1 Summary

Data usage continues to increase exponentially as users demand multimedia applications, cloud services, and other things related to the internet. This data growth requires a likewise growth in bandwidth, which can only be successfully supplied by optical communications, which places information on transmitted laser light. Under the accelerated growth even optical infrastructures are coming under strain to keep up with the amount of data. This is leading to spectrally efficient solutions that utilise both amplitude and phase modulation of optical signals to increase the number of bits per symbol. The primary modulators are Mach-Zehnder Modulators (MZMs) because they can achieve this advanced modulation. Thus this work looked to integrate the passive MZM with a laser source, to create a single chip transmitter.

Integration of multiple optical components onto single chips to form Photonic Integrated Circuits (PICs) provides the benefits of compactness and with it reliability, simpler coupling, and lower power consumption. The reduction in power and manufacturing time, and the volume scalability of the minimised PICs, allows a reduction in cost, which chiefly motivates their study.

Photonic integration is challenging because different devices are made of different materials so that they cannot usually be placed on the same chip. This makes integration of a passive MZM with an active laser extremely difficult. Existing integration techniques use regrowth steps to selectively replace the correct materials around the chip, but crucially this is costly, and requires growth and fabrication labs to be combined.

This work thus used regrowth-free monolithic integration to combine passive and active materials. The passive material was placed vertically above the active

material, and we believe this is the first time that has been performed on InP. The stacked material formed a PIC with an additional degree of freedom in the vertical direction. Both materials consisted of AlGaInAs alloys on InP, and again we believe this is the first time two AlGaInAs waveguides have been vertically integrated on a regrowth-free monolithic PIC.

Waveguides were defined using standard lithography processes, providing the benefit over regrowth techniques. Coupling between the vertically stacked waveguides was achieved through laterally defined tapers. The tapers reduced the effective refractive index of the upper passive waveguide so that the light mode supported within the structure became more confined by the lower active waveguide. Again, these tapers were achieved with standard lithography and did not require any regrowth.

The taper transitions were designed using BPM simulations, which correlated to analytical investigations. The optimum taper shape was found to be a linear taper because it outperforms taper shapes that slowly change in the transition region. Furthermore, performance between different tapers is comparable due to the tiny dimensions, and as a linear taper is easiest to draw on a lithographic mask it presents itself for selection.

The vertical coupling between the two waveguides on their own was not satisfactory, having high optical power loss, once a thick isolating InP barrier was included between the stacked waveguides. The isolating barrier is critical to integrated performance, as arbitrary optimised photonic devices can then be combined without a redesign to accommodate for the devices it is integrated with. Other works have neglected this isolation barrier, claiming that the coupling is weak enough to allow satisfactory integrated performance. In this work however, the component of interest was an MZM which is destined for high-speed advanced modulation and thus cannot be interfered with.

The poor vertical coupling of the two waveguides was overcome with the addition of an intermediate passive waveguide into the barrier region. This additional waveguide was based on CTAP, which provides an adiabatic transition of a mode from a first to a second waveguide through a third, and this third waveguide possesses no light at the end of the transition. Operation with the added intermediate waveguide was simulated with BPM to find the refractive index of the waveguide, such that the vertical coupling was greatly increased while the MZM waveguide remained isolated from the active waveguide below.

One of the two stacked waveguides must be inverted in order to form junctions for both the waveguides. As the MZM is the more advanced component, the laser

was chosen for inversion in order to leave the MZM untouched. P-dopant diffusion was seen to be considerable for the inverted laser, arising from the longer growth time experienced by the new p-substrate. The laser material was characterised using simple test structures, upon which current-voltage and capacitance-voltage measurements were performed to extract electrical and optical properties. ECVP and SIMS measurements were also performed on samples to profile the growth itself. These measurements indicated that p-dopants were closing the depletion width of the semiconductor junction and ruining optical efficiency. Following this determination of the laser failure, updated growths were made that successfully overcame the p-dopant diffusion and allowed laser performance the equal of traditional n-substrate lasers. The updated growths used pulled-back p-doping profile from the QW core, or a carbon doped blocking layer in the SCH layer between the QW core and the p-InP. Either of the updated growths are candidates for vertical integration.

The experimentally validated inverted lasers were incorporated into a full stacked waveguide design. The upper passive MZM material was substituted with a single passive core with the same thickness and average refractive index. This substitution was made to simplify the initial growth, as the key investigation was the vertical coupling rather than the MZM performance itself. The materials for the passive upper waveguide and intermediate waveguide were determined from material models, such that they had the correct refractive indices from the coupling simulations while being transparent to the laser output at the desired telecommunications wavelength of $1.55\mu m$.

New fabrication steps were required for the full grown stacked structure, as existing steps were only for a single waveguide. The vertically stacked structure was fabricated using a mere 6 mask steps, which were designed in this work along with the process steps to minimise complexity and thus minimise cost, as per the aims of PICs. Test structures were designed to experimentally prove a vertical transition between the stacked waveguides. These test structures featured bends in the upper passive layers in order to avoid any suggestion of erroneous throughput from the lower laser. Also included were the material characterisation pieces used with the inverted laser. Current-voltage and capacitance-voltage measurements were performed to determine the electrical properties and measure the depletion width of the waveguides, indicating that the inverted laser design should have held up to the longer growth. Indications of a successful growth was also provided by XRD measurements. However, current-voltage and PL measurements provided optical emission from which the optical power could be measured and its

spectrum observed, and unfortunately the emission of the lasers was incorrectly centred and weak.

While the vertically integrated laser failed to create strong optical emission, its spectrum was broad and this allowed a wavelength dependent measurement of the vertical coupling. Using the test structures it was measured that the desired operating wavelength of $1.55\mu m$ was filtered from the broad active waveguide emission in the vertical transitions showing a vertical transition had taken place within the tapered device.

Lensed fibre mounted on piezoelectric motors was used to scan across the facets of both the lower and upper waveguides to image the mode shapes. Again for the lower waveguide forward biased and the upper waveguide unbiased, optical emission was recorded from the upper waveguide output and imaged. Comparing the mode shape of the upper output to the lower waveguide output showed that the mode shapes differed and matched the shapes predicted from mode solutions of the different waveguide geometries.

All these measurements were also attained using an injected TLS rather than the lower active waveguide. Emission from the biased lower active waveguide was recorded from the unbiased passive upper waveguide output. Thus a vertical transition has been proven to take place in the vertically integrated waveguides.

5.2 Conclusions

A vertical transition of the lower active waveguide mode to the upper waveguide was proven by experimental measurement. This result illustrates that a vertical monolithic PIC is possible. The vertical coupling occurred at the desired operating wavelength of $1.55\mu m$, proving that the design simulations were correct and the technique could again be applied to similar problems.

The integrated laser failed to operate as well as the previous lasers with the same epitaxial structure had. Those previous sole lasers were experimentally characterised, and the integrated lasers indicated the same depletion width, yet still did not lase. It is unclear what caused the laser failure, but owing to the incorrect emission spectrum it may be determined that the growth failed, despite XRD measurements indicating lattice matching to InP.

The upper waveguide behaviour was as designed, allowing vertical coupling around the operating wavelength. The material choices were thus correct, and unlike the lower active waveguide were epitaxially grown successfully. This may be due to their placement at the top of the growth so that the growth time was

typical of single waveguide growths, and the layers were not inverted.

While the integrated p-substrate laser suffered failure, p-substrate lasers on their own were successfully grown and fabricated to overcome inherent high p-dopant diffusion. These lasers can find their use in other vertically stacked waveguides, or in any other avenue where a p-InP substrate is desired.

In the experimental measurement of this work's vertically integrated PIC, different test structures were designed, along with the processing steps to create them, in order to thoroughly characterise the material. These structures were designed to be tested easily with standard photonic laboratory equipment, not requiring any extra expensive set-ups.

Extensive computer simulations were performed for the stacked waveguides, providing the refractive index profile that would lead to vertical coupling. These numerical simulations were also supported by analytical waveguiding expressions as extracted from the wave equation, allowing greater understanding of the mode behaviour.

Altogether, a vertically stacked regrowth-free monolithic PIC has been designed, epitaxially grown, fabricated with 6 mask steps, and experimentally characterised to prove a successful vertical transition between a lower AlGaInAs active waveguide and an upper passive AlGaInAs waveguide on an InP platform. This PIC is destined to provide low cost spectrally efficient advanced modulation formats required by the continued exponential growth of bandwidth due to data growth.

5.3 Future Work

It has been noted that the lower laser of the vertical PIC was unsuccessful. So firstly, this lower laser needs to be grown and processed to emit laser light at $1.55\mu m$ as it did when processed on its own. This may require precise, but expensive, SIMS measurements of the full epitaxial structure to determine how the p-dopants truly behaved, or if there are other growth issues that prevented success. Once the growth failure can be determined, it can be overcome as in the inverted lasers of Chapter 3.

Integration of a laser would then allow characterisation of the vertical coupler. The same test structures could be fabricated using the same processing steps as in this work. The taper length dependence of the coupling could then be experimentally measured for comparison with the simulated results, and the optimum taper could be determined.

Following a successful integration of the laser layers with the already achieved upper waveguide layers in this work, those upper layers can be replaced by fully optimised MZM QW layers. Once the full layers are grown, the overall aim of this work would be achieved, the low cost integration of a laser and MZM. The MZM would need to be characterised to ensure that its operation is as good as when on its own.

Beyond a successful vertical integration, the vertical coupling could be investigated even further to attempt improvements. The vertical coupling technique was inspired by CTAP. The CTAP technique allows the coupling coefficients of the waveguides to have any dependence on propagation distance, but of course certain dependencies are supposed to perform better than others. In this work the simplest case of a single taper was used, but future work could investigate the ordering of multiple tapers on multiple layers. If the coupling can be increased with acceptable increases in fabrication complexity then the taper transition could be updated.

On a similar note; the submicron taper tips provided the most challenging aspect of the fabrication in this work, so if they can be simplified it would further simplify the integration process. Considering the difficult task of vertically integrating waveguides, it can be seen as a positive that the height of complication comes only from taper tips. Grating couplers were introduced in Chapter 1 where it was shown they can reduce the effective index of a waveguide. In this work gratings were omitted for simplicity, but if they could be incorporated into the waveguide tapers they may be able to increase the taper dimensions above the submicron range. Once again, the addition of grating couplers is only viable if the increase in fabrication complexity is acceptable.

On the topic of p-substrate lasers, there is room for more characterisation of the growth behaviour. Further investigation is required into how the carbon doped AlGaInAs acts neutrally and blocks Zn diffusion, as well as how far the p-doping profile needs to be pulled back from the QW core of the laser. As with all the other points in this section, these investigations will require more growths and processing than was manageable within the time frame of this thesis.

While the focus of this thesis has been on telecommunications applications, the vertical regrowth-free monolithic PIC techniques outlined here could be applied to any other field that warrants any combination of active and passive photonic devices.

References

[1] A. E. Willner, S. Khaleghi, M. R. Chitgarha, and O. F. Yilmaz, "All-optical signal processing," *Journal of Lightwave Technology*, vol. 32, no. 4, pp. 660–680, 2014.

[2] E. Agrell, M. Karlsson, A. R. Chraplyvy, D. J. Richardson, P. M. Krummrich, P. Winzer, K. Roberts, J. K. Fischer, S. J. Savory, B. J. Eggleton, M. Secondini, F. R. Kschischang, A. Lord, J. Prat, I. Tomkos, J. E. Bowers, S. Srinivasan, M. Brandt-Pearce, and N. Gisin, "Roadmap of optical communications," *Journal of Optics*, vol. 18, no. 6, p. 063002, 2016.

[3] B. Tossoun, R. Stephens, Y. Wang, S. Addamane, G. Balakrishnan, A. Holmes, and A. Beling, "High-speed InP-based p-i-n photodiodes with InGaAs/GaAsSb type-II quantum wells," *IEEE Photonics Technology Letters*, vol. 30, no. 4, pp. 399–402, 2018.

[4] S. J. B. Yoo, B. Guan, and R. P. Scott, "Heterogeneous 2D/3D photonic integrated microsystems," *Microsystems & Nanoengineering*, vol. 2, p. 16030, 2016.

[5] P. R. A. Binetti, M. Lu, E. J. Norberg, R. S. Guzzon, J. S. Parker, A. Sivananthan, A. Bhardwaj, L. A. Johansson, M. J. Rodwell, and L. A. Coldren, "Indium phosphide photonic integrated circuits for coherent optical links," *IEEE Journal of Quantum Electronics*, vol. 48, no. 2, pp. 279–291, 2012.

[6] R. Essiambre, G. Kramer, P. J. Winzer, G. J. Foschini, and B. Goebel, "Capacity limits of optical fiber networks," *Journal of Lightwave Technology*, vol. 28, no. 4, pp. 662–701, 2010.

[7] A. D. Ellis, J. Zhao, and D. Cotter, "Approaching the non-linear shannon limit," *Journal of Lightwave Technology*, vol. 28, no. 4, pp. 423–433, 2010.

[8] K. Nakahara, T. Tsuchiya, E. Nomoto, and M. Mukaikubo, "Transmission properties of 1.3μm InGaAlAs MQW FP lasers in 10-Gb/s uncooled operation," *Journal of Lightwave Technology*, vol. 23, no. 12, p. 3997, 2005.

[9] D. F. Welch, F. A. Kish, S. Melle, R. Nagarajan, M. Kato, C. H. Joyner, J. L. Pleumeekers, R. P. Schneider, J. Back, A. G. Dentai, V. G. Dominic, P. W. Evans, M. Kauffman, D. J. H. Lambert, S. K. Hurtt, A. Mathur, M. L. Mitchell, M. Missey, S. Murthy, A. C. Nilsson, R. A. Salvatore, M. F. V. Leeuwen, J. Webjorn, M. Ziari, S. G. Grubb, D. Perkins, M. Reffle, and D. G. Mehuys, "Large-scale InP photonic integrated circuits: Enabling efficient scaling of optical transport networks," *IEEE Journal of Selected Topics in Quantum Electronics*, vol. 13, no. 1, pp. 22–31, 2007.

[10] O. G. López, D. Lasaosa, M. López-Amo, and M. Galarza, "Highly-efficient fully resonant vertical couplers for InP active-passive monolithic integration using vertically phase matched waveguides," *Optics Express*, vol. 21, no. 19, pp. 22717–22727, 2013.

[11] X. Li, S. Zhou, H. Ji, M. Luo, Q. Yang, L. Yi, R. Hu, C. Li, S. Fu, A. Alphones, W. Zhong, and C. Yu, "Transmission of 4×28-Gb/s PAM-4 over 160-km single mode fiber using 10G-class DML and photodiode," in *2016 Optical Fiber Communications Conference and Exhibition (OFC)*, pp. 1–3, 2016.

[12] P. D. Pukhrambam, S. L. Lee, and G. Keiser, "Electroabsorption modulated lasers with high immunity to residual facet reflection by using lasers with partially corrugated gratings," *IEEE Photonics Journal*, vol. 9, no. 2, pp. 1–16, 2017.

[13] K. Hasebe, T. Sato, K. Takeda, T. Fujii, T. Kakitsuka, and S. Matsuo, "High-speed modulation of lateral p-i-n diode structure electro-absorption modulator integrated with DFB laser," *Journal of Lightwave Technology*, vol. 33, no. 6, pp. 1235–1240, 2015.

[14] J. Li, S. Tang, J. Wang, Y. Liu, X. Chen, and J. Cheng, "An eight-wavelength BH DFB laser array with equivalent phase shifts for WDM systems," *IEEE Photonics Technology Letters*, vol. 26, no. 16, pp. 1593–1596, 2014.

[15] H. Yamaguchi, T. Nagira, G. Sakaino, K. Ono, and M. Takemi, "Electric

characteristics of ruthenium doped InP and its application for buried heterostructure lasers," *physica status solidi (c)*, vol. 9, pp. 342–345, 2 2012.

[16] R. Nagarajan, C. H. Joyner, R. P. Schneider, J. S. Bostak, T. Butrie, A. G. Dentai, V. G. Dominic, P. W. Evans, M. Kato, M. Kauffman, D. J. H. Lambert, S. K. Mathis, A. Mathur, R. H. Miles, M. L. Mitchell, M. J. Missey, S. Murthy, A. C. Nilsson, F. H. Peters, S. C. Pennypacker, J. L. Pleumeekers, R. A. Salvatore, R. K. Schlenker, R. B. Taylor, T. Huan-Shang, M. F. V. Leeuwen, J. Webjorn, M. Ziari, D. Perkins, J. Singh, S. G. Grubb, M. S. Reffle, D. G. Mehuys, F. A. Kish, and D. F. Welch, "Large-scale photonic integrated circuits," *IEEE Journal of Selected Topics in Quantum Electronics*, vol. 11, no. 1, pp. 50–65, 2005.

[17] T. Suganuma, S. Ghosh, M. Kazi, R. Kobayashi, Y. Nakano, and T. Tanemura, "Fully integrated stokes vector receiver with MQW-based photodetectors on InP," in *2017 European Conference on Optical Communication (ECOC)*, pp. 1–3, 2017.

[18] R. Stabile, A. Rohit, and K. A. Williams, "Monolithically integrated 8×8 space and wavelength selective cross-connect," *Journal of Lightwave Technology*, vol. 32, no. 2, pp. 201–207, 2014.

[19] L. A. Coldren, S. C. Nicholes, L. Johansson, S. Ristic, R. S. Guzzon, E. J. Norberg, and U. Krishnamachari, "High performance InP-based photonic ICs—A tutorial," *Lightwave Technology, Journal of*, vol. 29, no. 4, pp. 554–570, 2011.

[20] V. Tolstikin, S. Wagner, and J. S. Aitchison, "High-capacity optical interconnects using WDM photonic integrated circuits in GaAs," in *2012 Optical Interconnects Conference*, pp. 80–81, 2012.

[21] L. Hou, M. Haji, J. Akbar, J. H. Marsh, and A. C. Bryce, "AlGaInAs/InP monolithically integrated DFB laser array," *IEEE Journal of Quantum Electronics*, vol. 48, no. 2, pp. 137–143, 2012.

[22] C. Kachris and I. Tomkos, "A roadmap on optical interconnects in data centre networks," in *2015 17th International Conference on Transparent Optical Networks (ICTON)*, pp. 1–3, 2015.

[23] M. J. R. Heck, J. F. Bauters, M. L. Davenport, J. K. Doylend, S. Jain, G. Kurczveil, S. Srinivasan, Y. Tang, and J. E. Bowers, "Hybrid silicon

photonic integrated circuit technology," *IEEE Journal of Selected Topics in Quantum Electronics*, vol. 19, pp. 6100117–6100117, July 2013.

[24] Cisco, "Cisco visual networking index: Global mobile data traffic forecast update, 2016-2021 white paper," 2018.

[25] V. Beal, "Webopedia." `https://www.webopedia.com/TERM/B/bandwidth.html`, 2018. Accessed December-2018.

[26] K. Lawniczuk, O. Patard, R. Guillamet, N. Chimot, A. Garreau, C. Kazmierski, G. Aubin, and K. Merghem, "40-Gb/s colorless reflective amplified modulator," *IEEE Photonics Technology Letters*, vol. 25, no. 4, pp. 341–343, 2013.

[27] Y. Wang, Y. Yang, S. Zhang, L. Wang, and J. J. He, "Narrow linewidth single-mode slotted Fabry-Pérot laser using deep etched trenches," *IEEE Photonics Technology Letters*, vol. 24, no. 14, pp. 1233–1235, 2012.

[28] C. Caillaud, G. Glastre, F. Lelarge, R. Brenot, S. Bellini, J. F. Paret, O. Drisse, D. Carpentier, and M. Achouche, "Monolithic integration of a semiconductor optical amplifier and a high-speed photodiode with low polarization dependence loss," *IEEE Photonics Technology Letters*, vol. 24, no. 11, pp. 897–899, 2012.

[29] J. Alexander, P. Morrissey, H. Yang, M. Yang, Y. Zhao, M. Rensing, P. O'Brien, and F. Peters, "Butterfly packaged low-linewidth optical comb source," *Electronics Letters*, vol. 53, no. 9, pp. 615–616, 2017.

[30] S. Chen, W. Li, J. Wu, Q. Jiang, M. Tang, S. Shutts, S. N. Elliott, A. Sobiesierski, A. J. Seeds, I. Ross, P. M. Smowton, and H. Liu, "Electrically pumped continuous-wave III–V quantum dot lasers on silicon," *Nature Photonics*, vol. 10, p. 307, 2016.

[31] H. Fan, K. Liu, Q. Wei, M. Zhang, X. Ren, Y. Huang, and X. Duan, "The simulation of monolithic vertical integration of VCSEL and RCE photodiode," in *2017 16th International Conference on Optical Communications and Networks (ICOCN)*, pp. 1–3, 2017.

[32] M. Shirao, K. Kojima, and H. Itamoto, "53.2 Gb/s NRZ transmission over 10 km using high speed EML for 400GbE," in *2015 Opto-Electronics and Communications Conference (OECC)*, pp. 1–3, 2015.

[33] D. Pérez-Galacho, R. Zhang, A. Ortega-Moñux, R. Halir, C. Alonso-Ramos, P. Runge, K. Janiak, G. Zhou, H.-G. Bach, A. G. Steffan, and Í. Molina-Fernández, "Integrated polarization beam splitter for 100/400 GE polarization multiplexed coherent optical communications," *Journal of Lightwave Technology*, vol. 32, no. 3, pp. 361–368, 2014.

[34] T. Fujisawa, T. Itoh, S. Kanazawa, K. Takahata, Y. Ueda, R. Iga, H. Sanjo, T. Yamanaka, M. Kotoku, and H. Ishii, "Ultracompact, 160-Gbit/s transmitter optical subassembly based on 40-Gbit/s $\times$ 4 monolithically integrated light source," *Optics Express*, vol. 21, no. 1, pp. 182–189, 2013.

[35] M. Lu, H. C. Park, A. Sivananthan, J. S. Parker, E. Bloch, L. A. Johansson, M. J. W. Rodwell, and L. A. Coldren, "Monolithic integration of a high-speed widely tunable optical coherent receiver," *IEEE Photonics Technology Letters*, vol. 25, no. 11, pp. 1077–1080, 2013.

[36] N. Chimot, S. Joshi, J. G. Provost, K. Mekhazni, F. Blache, F. Pommereau, C. Fortin, Y. Gottesman, L. A. Neto, M. Gay, M. Thual, and F. Lelarge, "Monolithic integration on InP of a DML and a ring resonator for future access networks," *IEEE Photonics Technology Letters*, vol. 28, no. 19, pp. 2039–2042, 2016.

[37] J. Fu, Y. Xi, X. Li, and W.-P. Huang, "Narrow spectral width FP lasers for high-speed short-reach applications," *Journal of Lightwave Technology*, vol. 34, no. 21, pp. 4898–4906, 2016.

[38] R. Yu, S. Cheung, Y. Li, K. Okamoto, R. Proietti, Y. Yin, and S. J. B. Yoo, "A scalable silicon photonic chip-scale optical switch for high performance computing systems," *Optics Express*, vol. 21, no. 26, pp. 32655–32667, 2013.

[39] F. Wu, "4 x 25 GB/s receiver photonic integrated circuits in InP for applications in data center interconnects," in *Asia Communications and Photonics Conference 2013*, OSA Technical Digest (online), p. AF4B.3, Optical Society of America, 2013.

[40] G. K. Periyanayagam, T. Nishiyama, N. Kamada, Y. Onuki, and K. Shimomura, "Lasing characteristics of 1.2 μm GaInAsP LD on InP/Si substrate," *Physica Status Solidi (a)*, 1 2018.

[41] L. Yuan, L. Tao, H. Yu, W. Chen, D. Lu, Y. Li, G. Ran, and J. Pan, "Hybrid InGaAsP-Si evanescent laser by selective-area metal-bonding method," *IEEE Photonics Technology Letters*, vol. 25, no. 12, pp. 1180–1183, 2013.

[42] L. Thylén and L. Wosinski, "Integrated photonics in the 21st century," *Photonics Research*, vol. 2, no. 2, pp. 75–81, 2014.

[43] D. F. Welch, F. A. Kish, R. Nagarajan, C. H. Joyner, J. R. P. Schneider, V. G. Dominic, M. L. Mitchell, S. G. Grubb, T.-K. Chiang, D. D. Perkins, and A. C. Nilsson, "The realization of large-scale photonic integrated circuits and the associated impact on fiber-optic communication systems," *Journal of Lightwave Technology*, vol. 24, no. 12, pp. 4674–4683, 2006.

[44] I. Moerman, P. P. Van Daele, and P. M. Demeester, "A review on fabrication technologies for the monolithic integration of tapers with III-V semiconductor devices," *IEEE Journal of Selected Topics in Quantum Electronics*, vol. 3, no. 6, pp. 1308–1320, 1998.

[45] D. Liang and J. E. Bowers, "Photonic integration: Si or InP substrates?," *Electronics Letters*, vol. 45, no. 12, pp. 578–581, 2009.

[46] Z. Huang, T. Cao, L. Chen, Y. Yu, and X. Zhang, "Monolithic integrated chip with SOA and tunable DI for multichannel all-optical signal processing," *IEEE Photonics Journal*, vol. 10, no. 2, pp. 1–9, 2018.

[47] P. J. Winzer, "Modulation and multiplexing in optical communications," in *Lasers and Electro-Optics, 2009 and 2009 Conference on Quantum electronics and Laser Science Conference. CLEO/QELS 2009. Conference on*, pp. 1–2, IEEE, 2009.

[48] F. Bontempi, S. Faralli, N. Andriolli, and G. Contestabile, "An InP monolithically integrated unicast and multicast wavelength converter," *IEEE Photonics Technology Letters*, vol. 25, no. 22, pp. 2178–2181, 2013.

[49] M. A. Taubenblatt, "Optical interconnects for high-performance computing," *Journal of Lightwave Technology*, vol. 30, no. 4, pp. 448–457, 2012.

[50] J. J. G. M. van der Tol, Y. S. Oei, U. Khalique, R. Nötzel, and M. K. Smit, "InP-based photonic circuits: Comparison of monolithic integration techniques," *Progress in Quantum Electronics*, vol. 34, no. 4, pp. 135–172, 2010.

[51] P. A. Alvi, L. Pyare, S. Dalela, and M. J. Siddiqui, "An extensive study on simple and GRIN SCH-based In0.71Ga0.21Al0.08As/InP lasing heterostructures," *Physica Scripta*, vol. 85, no. 3, p. 035402, 2012.

[52] R. Nagarajan, M. Kato, D. Lambert, P. Evans, S. Corzine, V. Lal, J. Rahn, A. Nilsson, M. Fisher, M. Kuntz, J. Pleumeekers, A. Dentai, H.-S. Tsai, D. Krause, H. Sun, K.-T. Wu, M. Ziari, T. Butrie, M. Reffle, M. Mitchell, F. Kish, and D. Welch, “Terabit/s class InP photonic integrated circuits,” *Semiconductor Science and Technology*, vol. 27, no. 9, p. 094003, 2012.

[53] M. Dernaika, L. Caro, N. P. Kelly, M. Shayesteh, and F. H. Peters, “Tunable L-band semiconductor laser based on Mach–Zehnder interferometer,” *Optics Communications*, vol. 402, pp. 56–59, 2017.

[54] N. P. Kelly, L. Caro, M. Dernaika, and F. H. Peters, “Regrowth-free integration of injection locked slotted laser with an electroabsorption modulator,” *Optics Express*, vol. 25, no. 4, pp. 4054–4060, 2017.

[55] N. Kikuchi, E. Yamada, Y. Shibata, and H. Ishii, “High-speed InP-based Mach-Zehnder modulator for advanced modulation formats,” in *2012 IEEE Compound Semiconductor Integrated Circuit Symposium (CSICS)*, pp. 1–4, 2012.

[56] T. Takiguchi, T. Saito, K. Matsumoto, K. Takagi, Y. Morita, S. Hatakenaka, C. Watatani, K. Akiyama, M. Gotoda, E. Ishimura, T. Aoyagi, and A. Shima, “40G RZ-DQPSK transmitter monolithically integrated with tunable DFB laser array and Mach-Zehnder modulators,” in *2011 Optical Fiber Communication Conference and Exposition and the National Fiber Optic Engineers Conference*, pp. 1–3, 2011.

[57] S. W. Corzine, P. Evans, M. Fisher, J. Gheorma, M. Kato, V. Dominic, P. Samra, A. Nilsson, J. Rahn, I. Lyubomirsky, A. Dentai, P. Studenkov, M. Missey, D. Lambert, A. Spannagel, R. Muthiah, R. Salvatore, S. Murthy, E. Strzelecka, J. L. Pleumeekers, A. Chen, R. Schneider, R. Nagarajan, M. Ziari, J. Stewart, C. H. Joyner, F. Kish, and D. F. Welch, “Large-scale InP transmitter PICs for PM-DQPSK fiber transmission systems,” *IEEE Photonics Technology Letters*, vol. 22, no. 14, pp. 1015–1017, 2010.

[58] Y. Sasahata, T. Saito, T. Takiguchi, K. Takagi, K. Matsumoto, T. Nagira, H. Sakuma, D. Suzuki, R. Makita, M. Takabayashi, M. Gotoda, and E. Ishimura, “Tunable DFB laser array integrated with Mach-Zehnder modulators for 44.6 Gb/s DQPSK transmitter,” *IEEE Journal of Selected Topics in Quantum Electronics*, vol. 19, no. 4, pp. 1501507–1501507, 2013.

[59] S. Tsukamoto, D.-S. Ly-Gagnon, K. Katoh, and K. Kikuchi, “Coherent demodulation of 40-Gbit/s polarization-multiplexed QPSK signals with 16-GHz spacing after 200-km transmission,” in *Optical Fiber Communication Conference and Exposition and The National Fiber Optic Engineers Conference*, Technical Digest (CD), p. PDP29, Optical Society of America, 2005.

[60] D. Cui, J. Cao, A. Nazemi, T. He, G. Li, B. Catli, K. Hu, H. Zhang, B. Rhew, S. Sheng, Y. Shim, B. Zhang, and A. Momtaz, “High speed data converters and their applications in optical communication system,” in *2017 IEEE Compound Semiconductor Integrated Circuit Symposium (CSICS)*, pp. 1–4, 2017.

[61] C. L. M. Daunt and F. H. Peters, “Correction methods for electroabsorption modulator-based phase-shift keying photonic integrated circuits,” *IEEE Journal of Selected Topics in Quantum Electronics*, vol. 19, pp. 21–27, Nov 2013.

[62] A. Wieczorek, B. Roycroft, F. H. Peters, and B. Corbett, “TE/TM-mode pass polarizers and splitter based on an asymmetric twin waveguide and resonant coupling,” *Optical and Quantum Electronics*, vol. 44, no. 3, pp. 175–181, 2012.

[63] S. B. Estrella, L. A. Johansson, M. L. Masanovic, J. A. Thomas, and J. S. Barton, “First monolithic widely tunable photonic coherent transmitter in InP,” *IEEE Photonics Technology Letters*, vol. 25, no. 7, pp. 641–643, 2013.

[64] P. Runge, S. Schubert, A. Seeger, K. Janiak, J. Stephan, D. Trommer, and M. L. Nielsen, “Monolithic InP receiver chip with a variable optical attenuator for colorless WDM detection,” *IEEE Photonics Technology Letters*, vol. 26, no. 4, pp. 349–351, 2014.

[65] A. E. Willner, R. L. Byer, C. J. Chang-Hasnain, S. R. Forrest, H. Kressel, H. Kogelnik, G. J. Tearney, C. H. Townes, and M. N. Zervas, “Optics and photonics: Key enabling technologies,” *Proceedings of the IEEE*, vol. 100, no. Special Centennial Issue, pp. 1604–1643, 2012.

[66] J. J. G. M. v. d. Tol, Y. Jiao, L. Shen, A. Millan-Mejia, V. Pogoretskii, J. P. v. Engelen, and M. K. Smit, “Indium phosphide integrated photonics in membranes,” *IEEE Journal of Selected Topics in Quantum Electronics*, vol. 24, no. 1, pp. 1–9, 2018.

[67] K. Lawniczuk, C. Kazmierski, J. G. Provost, M. J. Wale, R. Piramidowicz, P. Szczepanski, M. K. Smit, and X. J. M. Leijtens, "InP-based photonic multiwavelength transmitter with DBR laser array," *IEEE Photonics Technology Letters*, vol. 25, no. 4, pp. 352–354, 2013.

[68] Y. Shibata, "Integration of semiconductor Mach-Zehnder modulator with tunable-wavelength laser diode," in *CLEO:2011 - Laser Applications to Photonic Applications*, OSA Technical Digest (CD), p. CFJ1, Optical Society of America, 2011.

[69] R. W. Tkach, "Scaling optical communications for the next decade and beyond," *Bell Labs Technical Journal*, vol. 14, no. 4, pp. 3–9, 2010.

[70] T. Yamamoto, T. Simoyama, S. Tanaka, M. Matsuda, A. Uetake, S. Okumura, M. Ekawa, and K. Morito, "AlGaInAs based photonic devices for high-speed data transmission," in *IPRM 2011 - 23rd International Conference on Indium Phosphide and Related Materials*, pp. 1–4, 2011.

[71] N. Dupuis, C. R. Doerr, L. Zhang, L. Chen, N. J. Sauer, P. Dong, L. L. Buhl, and D. Ahn, "InP-based comb generator for optical OFDM," *Journal of Lightwave Technology*, vol. 30, no. 4, pp. 466–472, 2012.

[72] K. N. Nguyen, P. J. Skahan, J. M. Garcia, E. Lively, H. N. Poulsen, D. M. Baney, and D. J. Blumenthal, "Monolithically integrated dual-quadrature receiver on InP with 30 nm tunable local oscillator," *Optics Express*, vol. 19, no. 26, pp. B716–B721, 2011.

[73] F. A. Kish, D. Welch, R. Nagarajan, J. L. Pleumeekers, V. Lal, M. Ziari, A. Nilsson, M. Kato, S. Murthy, P. Evans, S. W. Corzine, M. Mitchell, P. Samra, M. Missey, S. DeMars, R. P. Schneider, M. S. Reffle, T. Butrie, J. T. Rahn, M. V. Leeuwen, J. W. Stewart, D. J. H. Lambert, R. C. Muthiah, H. S. Tsai, J. S. Bostak, A. Dentai, K. T. Wu, H. Sun, D. J. Pavinski, J. Zhang, J. Tang, J. McNicol, M. Kuntz, V. Dominic, B. D. Taylor, R. A. Salvatore, M. Fisher, A. Spannagel, E. Strzelecka, P. Studenkov, M. Raburn, W. Williams, D. Christini, K. J. Thomson, S. S. Agashe, R. Malendevich, G. Goldfarb, S. Melle, C. Joyner, M. Kaufman, and S. G. Grubb, "Current status of large-scale InP photonic integrated circuits," *IEEE Journal of Selected Topics in Quantum Electronics*, vol. 17, pp. 1470–1489, Nov 2011.

[74] C. Grasse, G. Boehm, M. Mueller, T. Gruendl, R. Meyer, and M. C. Amann, "Empirical modeling of the refractive index for (AlGaIn)As lattice matched to InP," *Semiconductor Science and Technology*, vol. 25, no. 4, p. 045018, 2010.

[75] I. Fatadin, D. Ives, and S. J. Savory, "Laser linewidth tolerance for 16-QAM coherent optical systems using QPSK partitioning," *IEEE Photonics Technology Letters*, vol. 22, no. 9, pp. 631–633, 2010.

[76] G. Bosco, A. Carena, V. Curri, P. Poggiolini, and F. Forghieri, "Performance limits of Nyquist-WDM and CO-OFDM in high-speed PM-QPSK systems," *IEEE Photonics Technology Letters*, vol. 22, no. 15, pp. 1129–1131, 2010.

[77] J. Lee, M. Chen, and H. Wang, "Design and comparison of three 20-Gb/s backplane transceivers for duobinary, PAM4, and NRZ data," *IEEE Journal of Solid-State Circuits*, vol. 43, no. 9, pp. 2120–2133, 2008.

[78] F. Kish, R. Nagarajan, D. Welch, P. Evans, J. Rossi, J. Pleumeekers, A. Dentai, M. Kato, S. Corzine, R. Muthiah, M. Ziari, R. Schneider, M. Reffle, T. Butrie, D. Lambert, M. Missey, V. Lal, M. Fisher, S. Murthy, R. Salvatore, S. Demars, A. James, and C. Joyner, "From visible light-emitting diodes to large-scale III-V photonic integrated circuits," *Proceedings of the IEEE*, vol. 101, no. 10, pp. 2255–2270, 2013.

[79] R. A. Griffin and A. C. Carter, "Optical differential quadrature phase-shift key (oDQPSK) for high capacity optical transmission," in *Optical Fiber Communication Conference and Exhibit*, pp. 367–368, 2002.

[80] R. Nagarajan, J. Rahn, M. Kato, J. Pleumeekers, D. Lambert, V. Lal, H.-S. Tsai, A. Nilsson, A. Dentai, M. Kuntz, R. Malendevich, J. Tang, J. Zhang, T. Butrie, M. Raburn, B. Little, W. Chen, G. Goldfarb, V. Dominic, B. Taylor, M. Reffle, F. Kish, and D. Welch, "10 channel, 45.6 Gb/s per channel, polarization-multiplexed DQPSK, InP receiver photonic integrated circuit," *Journal of Lightwave Technology*, vol. 29, no. 4, pp. 386–395, 2011.

[81] H. I. Cantú, A. McKee, I. Eddie, and A. E. Kelly, "Parametric study of 1310nm ridge waveguide AlGaInAs-InP semi-conductor laser dynamics," *IET Optoelectronics*, vol. 9, no. 6, pp. 341–347, 2015.

[82] N. Kikuchi, Y. Shibata, K. Tsuzuki, H. Sanjoh, T. Sato, E. Yamada, T. Ishibashi, and H. Yasaka, "80-Gb/s low-driving-voltage InP DQPSK

modulator with an n-p-i-n structure," *IEEE Photonics Technology Letters*, vol. 21, no. 12, pp. 787–789, 2009.

[83] C. R. Doerr, L. Zhang, P. J. Winzer, J. H. Sinsky, A. L. Adamiecki, N. J. Sauer, and G. Raybon, "Compact high-speed InP DQPSK modulator," *IEEE Photonics Technology Letters*, vol. 19, no. 15, pp. 1184–1186, 2007.

[84] T. Yasui, Y. Shibata, K. Tsuzuki, N. Kikuchi, Y. Kawaguchi, M. Arai, and H. Yasaka, "Lossless 10-Gbit/s InP n-p-i-n Mach-Zehnder modulator monolithically integrated with semiconductor optical amplifier," in *OFC/NFOEC 2008 - 2008 Conference on Optical Fiber Communication/National Fiber Optic Engineers Conference*, pp. 1–3, 2008.

[85] T. Yasui, Y. Shibata, K. Tsuzuki, N. Kikuchi, M. Ishikawa, Y. Kawaguchi, M. Arai, and H. Yasaka, "10-Gb/s 100-km SMF transmission using InP Mach-Zehnder modulator monolithically integrated with semiconductor optical amplifier," *IEEE Photonics Technology Letters*, vol. 20, no. 13, pp. 1178–1180, 2008.

[86] K. Tsuzuki, T. Ishibashi, T. Ito, S. Oku, Y. Shibata, R. Iga, Y. Kondo, and Y. Tohmori, "40 Gbit/s n-i-n InP Mach-Zehnder modulator with a π voltage of 2.2 V," *Electronics Letters*, vol. 39, no. 20, pp. 1464–1466, 2003.

[87] S. Lange, R. Kaiser, M. Gruner, M. Hamacher, K. O. Velthaus, and M. Schell, "Low switching voltage InP-based travelling wave electrode Mach-Zehnder modulator monolithically integrated with DFB-laser for 60 Gb/s NRZ," in *2015 Optical Fiber Communications Conference and Exhibition (OFC)*, pp. 1–3, 2015.

[88] K. Tsuzuki, T. Ishibashi, T. Ito, S. Oku, Y. Shibata, T. Ito, R. Iga, Y. Kondo, and Y. Tohmori, "A 40-Gb/s InGaAlAs-InAlAs MQW n-i-n Mach-Zehnder modulator with a drive voltage of 2.3 V," *IEEE Photonics Technology Letters*, vol. 17, no. 1, pp. 46–48, 2005.

[89] Y. A. Akulova, G. A. Fish, P. Koh, P. Kozodoy, M. Larson, C. Schow, E. Hall, H. Marchand, P. Abraham, and L. A. Coldren, "10 Gb/s Mach-Zehnder modulator integrated with widely-tunable sampled grating DBR laser," in *Optical Fiber Communication Conference*, Technical Digest (CD), p. TuE4, Optical Society of America, 2004.

[90] B. E. Saleh and M. C. Teich, "Fundamentals of photonics," 1991.

[91] J.-M. Liu, *Photonic devices.* Cambridge University Press, 2005.

[92] K. Higuma, S. Mori, T. Kawanishi, and M. Izutsu, "A bias condition monitor technique for the nested Mach-Zehnder modulator," *IEICE Electronics Express*, vol. 3, no. 11, pp. 238–242, 2006.

[93] V. I. Tolstikhin, C. D. Watson, K. Pimenov, R. Moore, Y. Logvin, and F. Wu, "Laterally coupled DFB lasers for one-step growth photonic integrated circuits in InP," *IEEE Photonics Technology Letters*, vol. 21, no. 10, pp. 621–623, 2009.

[94] A. Wieczorek, B. Roycroft, F. H. Peters, and B. Corbett, "Loss analysis and increasing of the fabrication tolerance of resonant coupling by tapering the mode beating section," *Optical and Quantum Electronics*, vol. 42, no. 8, pp. 521–529, 2011.

[95] N. Andriolli, S. Faralli, X. J. M. Leijtens, J. Bolk, and G. Contestabile, "Monolithically integrated all-optical regenerator for constant envelope WDM signals," *Journal of Lightwave Technology*, vol. 31, no. 2, pp. 322–327, 2013.

[96] W. Liu, M. Li, R. S. Guzzon, E. J. Norberg, J. S. Parker, M. Lu, L. A. Coldren, and J. Yao, "A fully reconfigurable photonic integrated signal processor," *Nature Photonics*, vol. 10, p. 190, 2016.

[97] G. Gilardi, W. Yao, H. R. Haghighi, M. K. Smit, and M. J. Wale, "Substrate thickness effects on thermal crosstalk in InP-based photonic integrated circuits," *Journal of Lightwave Technology*, vol. 32, no. 17, pp. 3061–3066, 2014.

[98] M. Nawrocka, Q. Lu, W.-H. Guo, A. Abdullaev, F. Bello, J. O'Callaghan, T. Cathcart, and J. F. Donegan, "Widely tunable six-section semiconductor laser based on etched slots," *Optics Express*, vol. 22, no. 16, pp. 18949–18957, 2014.

[99] S. Tahvili, S. Latkowski, B. Smalbrugge, X. J. M. Leijtens, P. J. Williams, M. J. Wale, J. Parra-Cetina, R. Maldonado-Basilio, P. Landais, M. K. Smit, and E. A. J. M. Bente, "InP-based integrated optical pulse shaper: Demonstration of chirp compensation," *IEEE Photonics Technology Letters*, vol. 25, no. 5, pp. 450–453, 2013.

[100] K. Ławniczuk, M. Augustin Luc, N. Grote, J. Wale Michael, K. Smit Meint, and A. Williams Kevin, "Open access to technology platforms for InP-based photonic integrated circuits," 2015.

[101] C. R. Doerr, L. Zhang, P. J. Winzer, N. Weimann, V. Houtsma, T. C. Hu, N. J. Sauer, L. L. Buhl, D. T. Neilson, S. Chandrasekhar, and Y. K. Chen, "Monolithic InP dual-polarization and dual-quadrature coherent receiver," *IEEE Photonics Technology Letters*, vol. 23, no. 11, pp. 694–696, 2011.

[102] S. Liu, H. Wang, M. Sun, L. Zhang, W. Chen, D. Lu, L. Zhao, R. Broeke, W. Wang, and C. Ji, "AWG-based monolithic 4×12 GHz multichannel harmonically mode-locked laser," *IEEE Photonics Technology Letters*, vol. 28, no. 3, pp. 241–244, 2016.

[103] C.-W. Lee, "A review of polarization dependence applications for asymmetric waveguides vertical couplers in compound semiconductor indium phosphide," *International Journal of Optics*, vol. 2011, 2011.

[104] Y. Xuejin, M. L. Masanovic, E. J. Skogen, Z. Hu, D. J. Blumenthal, and L. A. Coldren, "Optical mode converter integration with InP-InGaAsP active and passive waveguides using a single regrowth process," *IEEE Photonics Technology Letters*, vol. 14, no. 9, pp. 1249–1251, 2002.

[105] M.-K. Chin, C.-W. Lee, and J. Shen, "Polarization-independent vertical coupler for photonics integration," *Optics Express*, vol. 12, no. 1, pp. 117–123, 2004.

[106] L. Chee-Wei, M. K. Chin, M. K. Iyer, and A. Popov, "Asymmetric waveguides vertical couplers for polarization-independent coupling and polarization-mode splitting," *Journal of Lightwave Technology*, vol. 23, no. 4, pp. 1818–1827, 2005.

[107] F.-Z. Lin, Y.-J. Chiu, S.-A. Tsai, and T.-H. Wu, "Laterally tapered undercut active waveguide fabricated by simple wet etching method for vertical waveguide directional coupler," *Optics Express*, vol. 16, no. 11, pp. 7588–7594, 2008.

[108] V. Tolstikhin, S. Saeidi, and K. Dolgaleva, "Design optimization and tolerance analysis of a spot-size converter for the taper-assisted vertical integration platform in InP," *Applied Optics*, vol. 57, no. 13, pp. 3586–3591, 2018.

[109] T. Komljenovic, S. Srinivasan, E. Norberg, M. Davenport, G. Fish, and J. E. Bowers, "Widely tunable narrow-linewidth monolithically integrated external-cavity semiconductor lasers," *IEEE Journal of Selected Topics in Quantum Electronics*, vol. 21, no. 6, pp. 214–222, 2015.

[110] T. Tekin, "Review of packaging of optoelectronic, photonic, and MEMS components," *IEEE Journal of Selected Topics in Quantum Electronics*, vol. 17, pp. 704–719, May 2011.

[111] R. Broeke, "European InP photonic integrated circuit foundry platform development," in *Optical Fiber Communication Conference*, OSA Technical Digest (online), p. W4H.5, Optical Society of America, 2016.

[112] K. T. Shiu, S. S. Agashe, and S. R. Forrest, "A simple monolithically integrated optical receiver consisting of an optical preamplifier and a p-i-n photodiode," *IEEE Photonics Technology Letters*, vol. 18, no. 8, pp. 956–958, 2006.

[113] M. Galarza, D. Van Thourhout, R. Baets, and M. Lopez-Amo, "Compact and highly-efficient vertical couplers for active-passive monolithic integration," in *Integrated Photonics Research and Applications*, p. IWG3, Optical Society of America, 2005.

[114] X. Duan, Y. Huang, H. Huang, X. Ren, Q. Wang, Y. Shang, X. Ye, and S. Cai, "Monolithically integrated photodetector array with a multistep cavity for multiwavelength receiving applications," *Journal of Lightwave Technology*, vol. 27, no. 21, pp. 4697–4702, 2009.

[115] M. Galarza, D. Van Thourhout, R. Baets, and M. Lopez-Amo, "Compact and highly-efficient polarization independent vertical resonant couplers for active-passive monolithic integration," *Optics Express*, vol. 16, no. 12, pp. 8350–8358, 2008.

[116] C.-H. Du and Y.-P. Chiou, "Vertical directional couplers with ultra-short coupling length based on hybrid plasmonic waveguides," *Journal of Lightwave Technology*, vol. 32, no. 11, pp. 2065–2071, 2014.

[117] I. P. Kaminow, "Optical integrated circuits: A personal perspective," *Journal of Lightwave Technology*, vol. 26, no. 9, pp. 994–1004, 2008.

[118] L. Caro, M. Dernaika, N. P. Kelly, P. E. Morrissey, J. K. Alexander, and F. H. Peters, "An integration-friendly regrowth-free tunable laser," *IEEE Photonics Technology Letters*, vol. 30, no. 3, pp. 270–272, 2018.

[119] C. S. Seibert and D. C. Hall, "High-index-contrast ridge waveguide laser with thermally oxidised etched facet and metal reflector," *Electronics Letters*, vol. 46, no. 15, pp. 1077–1078, 2010.

[120] F. Morichetti, S. Grillanda, and A. Melloni, "Breakthroughs in photonics 2013: Toward feedback-controlled integrated photonics," *IEEE Photonics Journal*, vol. 6, no. 2, pp. 1–6, 2014.

[121] M. Smit, J. v. d. Tol, and M. Hill, "Moore's law in photonics," *Laser & Photonics Reviews*, vol. 6, no. 1, pp. 1–13, 2012.

[122] S. Stopinski, L. Augustin, and R. Piramidowicz, "Single-frequency integrated ring laser for application in optical gyroscope systems," *IEEE Photonics Technology Letters*, vol. 30, no. 9, pp. 781–784, 2018.

[123] A. Bhardwaj, M. Larson, M. Moewe, and Y. Feng, "Low-loss InGaAsP/InP surface ridge waveguides for photonic integrated circuits," *IEEE Photonics Technology Letters*, vol. 28, no. 13, pp. 1403–1405, 2016.

[124] Q. Chen, Q. Lu, and W. Guo, "Theory and simulation of multi-channel interference (MCI) widely tunable lasers," *Optics Express*, vol. 23, no. 14, pp. 18040–18051, 2015.

[125] K. Chen, Z. Huang, G. Dong, and X. Zhang, "Design of an ultra-short coupler in an asymmetric twin-waveguide structure using transformation optics," *Applied Optics*, vol. 53, no. 33, pp. 7831–7837, 2014.

[126] C. Kazmierski, D. Carrara, K. Ławniczuk, G. Aubin, J. G. Provost, and R. Guillamet, "12.5GB operation of a novel monolithic 1.55μm BPSK source based on prefixed optical phase switching," in *2013 Optical Fiber Communication Conference and Exposition and the National Fiber Optic Engineers Conference (OFC/NFOEC)*, pp. 1–3, 2013.

[127] C. R. Doerr, "Highly integrated monolithic photonic integrated circuits," in *39th European Conference and Exhibition on Optical Communication (ECOC 2013)*, pp. 1–2, 2013.

[128] J. Akbar, L. Hou, M. Haji, M. J. Strain, J. H. Marsh, A. C. Bryce, and A. E. Kelly, "High-power AlGaInAs mode-locked DBR laser with integrated tapered optical amplifier," *IEEE Photonics Technology Letters*, vol. 25, no. 3, pp. 253–256, 2013.

[129] V. Tolstikhin, "Regrowth-free multi-guide vertical integration in inp for optical communications," in *IPRM 2011 - 23rd International Conference on Indium Phosphide and Related Materials*, pp. 1–4, 2011.

[130] K. Young-Shik, K. Sung-Bock, C. Yong-Duck, and K. Jeha, "Optical coupling analysis of dual-waveguide structure for monolithic integration of photonic devices," *IEEE Photonics Technology Letters*, vol. 17, no. 11, pp. 2304–2306, 2005.

[131] C. Watson, V. Tolstikhin, K. Pimenov, F. Wu, and Y. Logvin, "On-chip emitter for regrowth-free multi-guide vertical integration in InP," in *IEEE Photonic Society 24th Annual Meeting*, pp. 336–337, 2011.

[132] S. Arafin and L. A. Coldren, "Advanced InP photonic integrated circuits for communication and sensing," *IEEE Journal of Selected Topics in Quantum Electronics*, vol. 24, no. 1, pp. 1–12, 2018.

[133] N. P. Kelly, M. Dernaika, L. Caro, P. E. Morrissey, A. H. Perrott, J. K. Alexander, and F. H. Peters, "Regrowth-free single mode laser based on dual port multimode interference reflector," *IEEE Photonics Technology Letters*, vol. 29, no. 3, pp. 279–282, 2017.

[134] K. A. Williams, E. A. J. M. Bente, D. Heiss, Y. Jiao, K. Ławniczuk, X. J. M. Leijtens, J. J. G. M. van der Tol, and M. K. Smit, "InP photonic circuits using generic integration [invited]," *Photonics Research*, vol. 3, no. 5, pp. B60–B68, 2015.

[135] P. E. Morrissey, H. Yang, R. N. Sheehan, B. Corbett, and F. H. Peters, "Design and fabrication tolerance analysis of multimode interference couplers," *Optics Communications*, vol. 340, pp. 26–32, 2015.

[136] H. Yang, P. Morrissey, W. Cotter, C. L. M. Daunt, J. O. Callaghan, B. Roycroft, N. Ye, N. Kelly, B. Corbett, and F. H. Peters, "Monolithic integration of single facet slotted laser, SOA, and MMI coupler," *IEEE Photonics Technology Letters*, vol. 25, no. 3, pp. 257–260, 2013.

[137] C. Liu, G. Zhao, F. Yang, Q. Lu, and W. Guo, "Design of compact but fabrication-tolerant vertical coupler for active & passive integration," *Journal of Lightwave Technology*, vol. 36, no. 3, pp. 755–762, 2018.

[138] X. Liang, J. Mu, X. Li, and Y. Xi, "Efficient active-to-passive light coupling of InGaAsP/InP laser using subwavelength coupler," *IEEE Photonics Journal*, vol. 5, no. 6, pp. 6602408–6602408, 2013.

[139] V. I. Tolstikhin, A. Densmore, K. Pimenov, Y. Logvin, W. Fang, S. Laframboise, and S. Grabtchak, "Monolithically integrated optical channel monitor for DWDM transmission systems," *Journal of Lightwave Technology*, vol. 22, no. 1, pp. 146–153, 2004.

[140] G. Zhou and P. Runge, "Modeling of multiple-quantum-well p-i-n photodiodes," *IEEE Journal of Quantum Electronics*, vol. 50, no. 4, pp. 220–227, 2014.

[141] V. I. Tolstikhin, R. Moore, K. Pimenov, Y. Logvin, F. Wu, and C. D. Watson, "One-step growth optical transceiver PIC in InP," in *2009 35th European Conference on Optical Communication*, pp. 1–2, Sept 2009.

[142] X. Chen, W. Liu, J. An, Y. Liu, K. Xu, X. Wang, J. Liu, Y. Ji, and N. Zhu, "Photonic integrated technology for multi-wavelength laser emission," *Chinese Science Bulletin*, vol. 56, no. 28, p. 3064, 2011.

[143] F. v. Dijk, G. Kervella, M. Lamponi, M. Chtioui, F. Lelarge, E. Vinet, Y. Robert, M. J. Fice, C. C. Renaud, A. Jimenez, and G. Carpintero, "Integrated InP heterodyne millimeter wave transmitter," *IEEE Photonics Technology Letters*, vol. 26, no. 10, pp. 965–968, 2014.

[144] P. V. Studenkov, M. R. Gokhale, J. C. Dries, and S. R. Forrest, "Monolithic integration of a quantum-well laser and an optical amplifier using an asymmetric twin-waveguide structure," *IEEE Photonics Technology Letters*, vol. 10, no. 8, pp. 1088–1090, 1998.

[145] L. M. Augustin, R. Santos, E. d. Haan, S. Kleijn, P. J. A. Thijs, S. Latkowski, D. Zhao, W. Yao, J. Bolk, H. Ambrosius, S. Mingaleev, A. Richter, A. Bakker, and T. Korthorst, "InP-based generic foundry platform for photonic integrated circuits," *IEEE Journal of Selected Topics in Quantum Electronics*, vol. 24, no. 1, pp. 1–10, 2018.

[146] M. Dernaika, L. Caro, N. P. Kelly, J. K. Alexander, F. Dubois, P. E. Morrissey, and F. H. Peters, “Deeply etched inner-cavity pit reflector,” *IEEE Photonics Journal*, vol. 9, no. 1, pp. 1–8, 2017.

[147] F. Xia, V. M. Menon, and S. R. Forrest, “Photonic integration using asymmetric twin-waveguide (ATG) technology: part I-concepts and theory,” *Selected Topics in Quantum Electronics, IEEE Journal of*, vol. 11, no. 1, pp. 17–29, 2005.

[148] P. V. Studenkov, M. R. Gokhale, W. Lin, I. Glesk, P. R. Prucnal, and S. R. Forrest, “Monolithic integration of an all-optical Mach-Zehnder demultiplexer using an asymmetric twin-waveguide structure,” *IEEE Photonics Technology Letters*, vol. 13, no. 6, pp. 600–602, 2001.

[149] Q. Lv, Q. Han, P. Pan, H. Ye, D. Yin, and X. Yang, “Monolithic integration of a InP AWG and InGaAs photodiodes on InP platform,” *Optics & Laser Technology*, vol. 90, pp. 122–127, 2017.

[150] D. d’Agostino, D. Lenstra, H. Ambrosius, and M. Smit, “Coupled cavity laser based on anti-resonant imaging via multimode interference,” *Optics letters*, vol. 40, no. 4, pp. 653–656, 2015.

[151] X. Fengnian, W. Jian, V. Menon, and S. R. Forrest, “Monolithic integration of a semiconductor optical amplifier and a high bandwidth p-i-n photodiode using asymmetric twin-waveguide technology,” *IEEE Photonics Technology Letters*, vol. 15, no. 3, pp. 452–454, 2003.

[152] G. Grasso, P. Galli, M. Romagnoli, E. Iannone, and A. Bogoni, “Role of integrated photonics technologies in the realization of terabit nodes [invited],” *Journal of Optical Communications and Networking*, vol. 1, no. 3, pp. B111–B119, 2009.

[153] S. S. Saini, E. G. Johnson, D. R. Stone, W. Zhou, H. Shen, and M. Dagenais, “A 2×2 crosspoint switch fabricated on the passive active resonant coupler (PARC) platform,” *IEEE Photonics Technology Letters*, vol. 13, no. 3, pp. 203–205, 2001.

[154] T. Fujii, T. Sato, K. Takeda, K. Hasebe, T. Kakitsuka, and S. Matsuo, “Epitaxial growth of InP to bury directly bonded thin active layer on SiO_2/Si substrate for fabricating distributed feedback lasers on silicon,” *IET Optoelectronics*, vol. 9, no. 4, pp. 151–157, 2015.

[155] S. Kakimoto, "Temperature dependence of threshold currents of 1.55μm p-substrate buried crescent laser diodes," *Japanese journal of applied physics*, vol. 43, no. 9R, p. 6079, 2004.

[156] J. Piprek, J. K. White, and A. J. SpringThorpe, "What limits the maximum output power of long-wavelength AlGaInAs/InP laser diodes?," *IEEE Journal of Quantum Electronics*, vol. 38, no. 9, pp. 1253–1259, 2002.

[157] S. R. Selmic, T.-M. Chou, J. Sih, J. B. Kirk, A. Mantle, J. K. Butler, D. Bour, and G. A. Evans, "Design and characterization of 1.3μm AlGaInAs-InP multiple-quantum-well lasers," *IEEE Journal of selected topics in Quantum Electronics*, vol. 7, no. 2, pp. 340–349, 2001.

[158] O. J. Pitts, W. Benyon, and A. J. SpringThorpe, "Modeling and process control of MOCVD growth of InAlGaAs MQW structures on InP," *Journal of Crystal Growth*, vol. 393, pp. 81–84, 2014.

[159] M. Smit, X. Leijtens, H. Ambrosius, E. Bente, J. van der Tol, B. Smalbrugge, T. de Vries, E.-J. Geluk, J. Bolk, R. van Veldhoven, L. Augustin, P. Thijs, D. D'Agostino, H. Rabbani, K. Lawniczuk, S. Stopinski, S. Tahvili, A. Corradi, E. Kleijn, D. Dzibrou, M. Felicetti, E. Bitincka, V. Moskalenko, J. Zhao, R. Santos, G. Gilardi, W. Yao, K. Williams, P. Stabile, P. Kuindersma, J. Pello, S. Bhat, Y. Jiao, D. Heiss, G. Roelkens, M. Wale, P. Firth, F. Soares, N. Grote, M. Schell, H. Debregeas, M. Achouche, J.-L. Gentner, A. Bakker, T. Korthorst, D. Gallagher, A. Dabbs, A. Melloni, F. Morichetti, D. Melati, A. Wonfor, R. Penty, R. Broeke, B. Musk, and D. Robbins, "An introduction to InP-based generic integration technology," *Semiconductor Science and Technology*, vol. 29, no. 8, p. 083001, 2014.

[160] Z. Liao, S. J. Wagner, M. Z. Alam, V. Tolstikhin, and J. Stewart Aitchison, "Vertically integrated spot-size converter in algaas-gaas," *Optics Letters*, vol. 42, no. 20, pp. 4167–4170, 2017.

[161] S. S. Saini, V. Vusirikala, R. Whaley, F. G. Johnson, D. Stone, and M. Dagenais, "Compact mode expanded lasers using resonant coupling between a 1.55μm ingaasp tapered active region and an underlying coupling waveguide," *IEEE Photonics Technology Letters*, vol. 10, no. 9, pp. 1232–1234, 1998.

[162] Z. Liao and J. S. Aitchison, "Precision etching for multi-level AlGaAs waveguides," *Optical Materials Express*, vol. 7, no. 3, pp. 895–903, 2017.

[163] S. Saini, F. Johnson, Z. Dilli, Y. Hu, R. Grover, D. Stone, P. Shen, J. Pamulapati, W. Zhou, and M. Dagenais, “Compact low-loss vertical resonant mode coupling between two well-confined waveguides,” 1999.

[164] P. E. Morrissey, N. Kelly, M. Dernaika, L. Caro, H. Yang, and F. H. Peters, “Coupled cavity single-mode laser based on regrowth-free integrated MMI reflectors,” *IEEE Photonics Technology Letters*, vol. 28, no. 12, pp. 1313–1316, 2016.

[165] K. H. Lee, B. Roycroft, J. O. Callaghan, C. L. L. M. Daunt, H. Yang, J. H. Song, F. H. Peters, and B. Corbett, “Integration of AlInGaAs-MQW Fabry-Pérot lasers with emission at two wavelength ranges via quantum-well intermixing,” *IEEE Photonics Technology Letters*, vol. 23, no. 1, pp. 27–29, 2011.

[166] L. M. Augustin, J. J. G. M. v. d. Tol, E. J. Geluk, and M. K. Smit, “Short polarization converter optimized for active & passive integration in InGaAsP/InP,” *IEEE Photonics Technology Letters*, vol. 19, no. 20, pp. 1673–1675, 2007.

[167] E. Kleijn, D. Melati, A. Melloni, T. d. Vries, M. K. Smit, and X. J. M. Leijtens, “Multimode interference couplers with reduced parasitic reflections,” *IEEE Photonics Technology Letters*, vol. 26, no. 4, pp. 408–410, 2014.

[168] G. Kurczveil, P. Pintus, M. J. R. Heck, J. D. Peters, and J. E. Bowers, “Characterization of insertion loss and back reflection in passive hybrid silicon tapers,” *IEEE Photonics Journal*, vol. 5, no. 2, pp. 6600410–6600410, 2013.

[169] L. Chee-Wei, L. Shuh-Ying, and C. Mee-Koy, “Demonstration of a single-mesa vertical coupler and its integration with a multimode interferometer,” *Semiconductor Science and Technology*, vol. 26, no. 7, p. 075008, 2011.

[170] M. Dernaika, N. P. Kelly, L. Caro, and F. H. Peters, “Single mode semiconductor laser based on coupled cavities of an active ring laser and Fabry Perot,” *IET Optoelectronics*, 2017.

[171] Q. Lu, W. Guo, M. Nawrocka, A. Abdullaev, C. Daunt, J. O’Callaghan, M. Lynch, V. Weldon, F. Peters, and J. F. Donegan, “Single mode lasers based on slots suitable for photonic integration,” *Optics Express*, vol. 19, no. 26, pp. B140–B145, 2011.

[172] A. Wieczorek, B. Roycroft, J. O. Callaghan, K. Thomas, E. Pelucchi, F. H. Peters, and B. Corbett, “Polarizers in an asymmetric twin waveguide based on resonant coupling,” *IEEE Photonics Technology Letters*, vol. 25, no. 14, pp. 1301–1304, 2013.

[173] Y. Suematsu, M. Yamada, and K. Hayashi, “Integrated twin-guide AlGaAs laser with multiheterostructure,” *IEEE Journal of Quantum Electronics*, vol. 11, no. 7, pp. 457–460, 1975.

[174] H. Yu, X. Fengnian, V. M. Menon, S. R. Forrest, and M. Gokhale, “Reduction of absorption loss in asymmetric twin waveguide laser tapers using argon plasma-enhanced quantum-well intermixing,” *IEEE Photonics Technology Letters*, vol. 16, no. 10, pp. 2221–2223, 2004.

[175] W. Hongsheng, L. Chunqian, and S. R. Forrest, “A fully integratable 1.55μm wavelength continuously tunable asymmetric twin-waveguide distributed bragg reflector laser,” *IEEE Photonics Technology Letters*, vol. 15, no. 9, pp. 1189–1191, 2003.

[176] P. V. Studenkov, F. Xia, M. R. Gokhale, and S. R. Forrest, “Asymmetric twin-waveguide 1.55μm wavelength laser with a distributed bragg reflector,” *IEEE Photonics Technology Letters*, vol. 12, no. 5, pp. 468–470, 2000.

[177] P. V. Studenkov, M. R. Gokhale, and S. R. Forrest, “Efficient coupling in integrated twin-waveguide lasers using waveguide tapers,” *IEEE Photonics Technology Letters*, vol. 11, no. 9, pp. 1096–1098, 1999.

[178] M. Raburn, L. Bin, K. Rauscher, O. Yae, N. Dagli, and J. E. Bowers, “3-D photonic circuit technology,” *IEEE Journal of Selected Topics in Quantum Electronics*, vol. 8, no. 4, pp. 935–942, 2002.

[179] Y. Fu, T. Ye, W. Tang, and T. Chu, “Efficient adiabatic silicon-on-insulator waveguide taper,” *Photon. Res.*, vol. 2, pp. A41–A44, Jun 2014.

[180] S.-Y. Tseng and X. Chen, “Engineering of fast mode conversion in multimode waveguides,” *Optics Letters*, vol. 37, no. 24, pp. 5118–5120, 2012.

[181] X. Sun, H. C. Liu, and A. Yariv, “How short can an adiabatic mode transformer be in a coupled waveguide system?,” in *2009 Conference on Lasers and Electro-Optics and 2009 Conference on Quantum electronics and Laser Science Conference*, pp. 1–2, 2009.

[182] X. Sun, H.-C. Liu, and A. Yariv, "Adiabaticity criterion and the shortest adiabatic mode transformer in a coupled-waveguide system," *Optics Letters*, vol. 34, no. 3, pp. 280–282, 2009.

[183] S.-Y. Tseng, R.-D. Wen, Y.-F. Chiu, and X. Chen, "Short and robust directional couplers designed by shortcuts to adiabaticity," *Optics Express*, vol. 22, no. 16, pp. 18849–18859, 2014.

[184] S.-Y. Tseng, "Counterdiabatic mode-evolution based coupled-waveguide devices," *Optics Express*, vol. 21, no. 18, pp. 21224–21235, 2013.

[185] G. T. Paloczi, A. Eyal, and A. Yariv, "Wavelength-insensitive nonadiabatic mode evolution couplers," *IEEE Photonics Technology Letters*, vol. 16, no. 2, pp. 515–517, 2004.

[186] R. Blanchard, C. Grezes, S. Menzel, C. Pflügl, L. Diehl, Y. Huang, J. H. Ryou, R. D. Dupuis, and F. Capasso, "Vertical monolithic integration of quantum cascade lasers for high-power broadband applications," in *2012 Conference on Lasers and Electro-Optics (CLEO)*, pp. 1–2, 2012.

[187] J.-M. Liu, *Photonic devices.* Cambridge University Press, 2009.

[188] K. Kawano and T. Kitoh, *Introduction to Optical Waveguide Analysis: Solving Maxwell's Equation and the Schrödinger Equation.* John Wiley & Sons, 2004.

[189] L. A. Coldren, S. W. Corzine, and M. L. Mashanovitch, *Diode lasers and photonic integrated circuits*, vol. 218. John Wiley & Sons, 2012.

[190] A. Yariv and P. Yeh, *Photonics: optical electronics in modern communications*, vol. 6. Oxford University Press New York, 2007.

[191] H. Klein, *Integrated InP Mach-Zehnder Modulators for 100 Gbit/s Ethernet Applications using QPSK Modulation.* Berlin, Techn. Univ., Diss., 2010, 2010.

[192] RSoft, *BeamPROP.* Synopsys Inc., Optical Solutions Group, v2014.09.

[193] IQE. `http://www.iqep.com/`. Accessed December-2018.

[194] S. Longhi, G. Della Valle, M. Ornigotti, and P. Laporta, "Coherent tunneling by adiabatic passage in an optical waveguide system," *Physical Review B*, vol. 76, no. 20, p. 201101, 2007. PRB.

[195] S. Longhi, "Quantum-optical analogies using photonic structures," *Laser & Photonics Reviews*, vol. 3, no. 3, pp. 243–261, 2009.

[196] S. Longhi, "Adiabatic passage of light in coupled optical waveguides," *Physical Review E*, vol. 73, no. 2, p. 026607, 2006. PRE.

[197] I. Vorobeichik, M. Orenstein, and N. Moiseyev, "Intermediate-mode-assisted optical directional couplers via embedded periodic structure," *IEEE Journal of Quantum Electronics*, vol. 34, no. 9, pp. 1772–1781, 1998.

[198] S. Longhi, "Optical realization of multilevel adiabatic population transfer in curved waveguide arrays," *Physics Letters A*, vol. 359, no. 2, pp. 166–170, 2006.

[199] U. Hohenester, J. Fabian, and F. Troiani, "Adiabatic passage schemes in coupled semiconductor nanostructures," *Optics Communications*, vol. 264, no. 2, pp. 426–434, 2006.

[200] N. V. Vitanov, A. A. Rangelov, B. W. Shore, and K. Bergmann, "Stimulated Raman adiabatic passage in physics, chemistry, and beyond," *Reviews of Modern Physics*, vol. 89, no. 1, p. 015006, 2017. RMP.

[201] E. Paspalakis, "Adiabatic three-waveguide directional coupler," *Optics Communications*, vol. 258, no. 1, pp. 30–34, 2006.

[202] Y. Lahini, F. Pozzi, M. Sorel, R. Morandotti, D. N. Christodoulides, and Y. Silberberg, "Effect of nonlinearity on adiabatic evolution of light," *Physical Review Letters*, vol. 101, no. 19, p. 193901, 2008. PRL.

[203] M. V. Berry, "Quantal phase factors accompanying adiabatic changes," *Proceedings of the Royal Society of London. A. Mathematical and Physical Sciences*, vol. 392, no. 1802, p. 45, 1984.

[204] J. Oreg, F. T. Hioe, and J. H. Eberly, "Adiabatic following in multilevel systems," *Physical Review A*, vol. 29, no. 2, pp. 690–697, 1984. PRA.

[205] K. Bergmann, H. Theuer, and B. W. Shore, "Coherent population transfer among quantum states of atoms and molecules," *Reviews of Modern Physics*, vol. 70, no. 3, pp. 1003–1025, 1998. RMP.

[206] F. Dreisow, M. Ornigotti, A. Szameit, M. Heinrich, R. Keil, S. Nolte, A. Tünnermann, and S. Longhi, "Polychromatic beam splitting by frac-

tional stimulated Raman adiabatic passage," *Applied Physics Letters*, vol. 95, no. 26, p. 261102, 2009.

[207] A. D. Greentree, J. H. Cole, A. R. Hamilton, and L. C. L. Hollenberg, "Coherent electronic transfer in quantum dot systems using adiabatic passage," *Physical Review B*, vol. 70, no. 23, p. 235317, 2004. PRB.

[208] A. M. Kenis, I. Vorobeichik, M. Orenstein, and N. Moiseyev, "Non-evanescent adiabatic directional coupler," *IEEE Journal of Quantum Electronics*, vol. 37, no. 10, pp. 1321–1328, 2001.

[209] S. Longhi, "Coherent transfer by adiabatic passage in two-dimensional lattices," *Annals of Physics*, vol. 348, pp. 161–175, 2014.

[210] E. F. Schubert, "Chapter 12: Visible-spectrum LEDs." `https://www.ecse.rpi.edu/~schubert/Light-Emitting-Diodes-dot-org/chap12/F12-06%20III-V%20bandgap%20energie.jpg`, 2001. Accessed December-2018.

[211] Ioffe Institute, "NSM archive - physical properties of semiconductors." `http://www.ioffe.ru/SVA/NSM/Semicond/InP/electric.html#Basic`, 2001. Accessed November-2018.

[212] S. P. Duggan, N. P. Kelly, L. Caro, M. Dernaika, M. Shayesteh, J. K. Alexander, H. Yang, P. E. Morrissey, A. M. Gocalińska, K. K. Thomas, *et al.*, "Development of inverted p-substrate InP/AlGaInAs lasers for vertical integration with multiple passive or active intrinsic regions," in *European Conference on Integrated Optics 2017*, European Conference on Integrated Optics, 2017.

[213] S. P. Duggan, H. Yang, N. P. Kelly, L. Caro, M. Dernaika, M. Shayesteh, A. Gocalinska, K. Thomas, E. Pelucchi, B. Corbett, and F. H. Peters, "P-substrate InP-based 1.5μm lasers using an internal carbon-doped layer to block p-dopant diffusion," *Microwave and Optical Technology Letters*, vol. 60, no. 10, pp. 2363–2367, 2018.

[214] H. Yamaguchi, T. Nagira, Z. Kawazu, K. Ono, and M. Takemi, "Dependence of the diffusion of zinc from zinc-into ruthenium-doped indium phosphide on zinc concentration," in *26th International Conference on Indium Phosphide and Related Materials (IPRM)*, pp. 1–2, 2014.

[215] K. L. Lear, H. Q. Hou, J. J. Banas, B. E. Hammons, J. Furioli, and M. Osinski, "Vertical cavity lasers on p-doped substrates," *Electronics Letters*, vol. 33, pp. 783–784, Apr 1997.

[216] *SimWindows*. http://simwindows.wixsite.com/simwindows.

[217] E. Kleijn, M. K. Smit, and X. J. M. Leijtens, "Multimode interference reflectors: A new class of components for photonic integrated circuits," *Journal of Lightwave Technology*, vol. 31, no. 18, pp. 3055–3063, 2013.

[218] G. D. Valicourt, G. H. Duan, C. Ware, M. Lamponi, and R. Brenot, "Experimental and theoretical investigation of mode size effects on tilted facet reflectivity," *IET Optoelectronics*, vol. 5, pp. 175–180, August 2011.

[219] D. Hodgson, K. Noonan, B. Olsen, and T. Orosz, "Pulsing a laser diode," *ILX Lightwave, Newport Corporation*, vol. Rev01.122804, no. 11, 2011.

[220] P. Sajewicz, C. Kelleher, and B. Corbett, "Influence of structure on external efficiency of wide stripe semiconductor lasers based on the analysis of spontaneous emission," *IET Optoelectronics*, vol. 4, no. 4, pp. 149–158, 2010.

[221] M. J. Cristea, "Capacitance-voltage profiling techniques for characterization of semiconductor materials and devices," *Emerging Trends in Electrical, Electronics and Instrumentation Engineering: An international Journal (EEIEJ)*, vol. 3, pp. 29–38, 2014.

[222] Probion Analysis, "Electrochemical CV-Profiling." `https://www.probion.fr/en/tutorials/ecvp/ecvprofiling.html`, 2018. Accessed December-2018.

[223] EAG Laboratories, "SIMS Tutorial: Theory." `https://www.eag.com/resources/tutorials/sims-tutorial-theory/`, 2018. Accessed December-2018.

[224] CAMECA, "Introduction to SIMS." `https://www.cameca.com/products/sims/technique`, 2018. Accessed December-2018.

[225] M. Achtenhagen and A. Hardy, "Lateral current spreading in ridge waveguide laser diodes," *Applied Physics Letters*, vol. 74, no. 10, pp. 1364–1366, 1999.

[226] E. V. K. Rao, B. Theys, J. L. Benchimol, and J. Chevallier, "Photoluminescence of as-grown and hydrogenated carbon-doped indium phosphide," *Semiconductor Science and Technology*, vol. 13, no. 6, p. 641, 1998.

[227] Compugraphics, "Compugraphics Photomasks." `https://www.compugraphics-photomasks.com/`, 2018. Accessed December-2018.

[228] P. E. Morrissey, D. Goulding, R. Sheehan, B. Roycroft, and F. H. Peters, "Experimental technique for quick and efficient lensed fibre to ridge waveguide coupling," *IET Optoelectronics*, vol. 7, no. 2, pp. 57–61, 2013.